DESIGN, MODELING, AND TESTING OF A SOLAR THERMOCHEMICAL INCLINED GRANULAR FLOW REACTOR FOR CONCENTRATED SOLAR POWER

A Dissertation
Presented to
The Academic Faculty

by

Andrew J. Schrader

In Partial Fulfillment
of the Requirements for the Degree
Doctor of Philosophy in the
G. W. Woodruff School of Mechanical Engineering

Georgia Institute of Technology
December 2019

DESIGN, MODELING, AND TESTING OF A SOLAR THERMOCHEMICAL INCLINED GRANULAR FLOW REACTOR FOR CONCENTRATED SOLAR POWER

Approved by:

Dr. Peter G. Loutzenhiser, Advisor (ME)
G. W. Woodruff School of Mechanical Engineering
Georgia Institute of Technology

Dr. Timothy Lieuwen (AE)
Daniel Guggenheim School of Aerospace Engineering
Georgia Institute of Technology

Dr. Sheldon Jeter (ME)
G. W. Woodruff School of Mechanical Engineering
Georgia Institute of Technology

Dr. Christopher Jones (Ch. E)
School of Chemical and Biomolecular Engineering
Georgia Institute of Technology

Dr. Zhuomin Zhang (ME)
G. W. Woodruff School of Mechanical Engineering
Georgia Institute of Technology

Date Approved: August 16, 2019

ACKNOWLEDGEMENTS

I thank my advisor, Dr. Peter Loutzenhiser, for his support and guidance during my graduate research and teaching experiences. I also thank my committee members, Dr. Sheldon Jeter, Dr. Christopher Jones, Dr. Timothy Lieuwen, and Dr. Zhuomin Zhang for their evaluation and advice in performing this research. I thank past and present colleagues in the Solar Fuels and Techonologies Laboratory: Malavika Bagepalli, Evan Bush, Ashley Clendenen, Chuyang Chen, Gianmarco De Dominicis, Tyler Farr, Robert Gill, Iacopo Guscetti, Alex Muroyama, Karl-Philipp Schlichting, Saverio Sparacio, Garrett Schieber, Nhu "Ty" Nguyen, and Justin Yarrington. I thank Evan Bush for being an insightful friend and colleague since we started together in Summer 2014. I thank Robert Gill for his mentorship and teaching me to always find joy in my work. I also thank Garrett Schieber and Alex Limia for their friendship, support, and technical expertise. I want to thank Evan+Kara, Robby+Erin, Garrett+Kaelynn, and Alex+Valery for creating a strong community of friends and scholars outside of the laboratory. My fondest memories of my time at Georgia Tech are of us all together.

I thank my wife, Amanda Schrader, for supporting my dreams and making them come true. I wish to thank my parents, Jeffrey L. Schrader and Dr. Cheryl B. Schrader, and my sister, Ella Schrader, for their love and support.

This material is based upon work supported by the U.S. Department of Energy SunShot initiative under Award No. DE-FOA-0000805-1541.

TABLE OF CONTENTS

LIST OF TABLES

LIST OF FIGURES

LIST OF SYMBOLS AND ABBREVIATIONS

A	area
a	first barycentric location
A_r	Area ratio between cavity and quartz window
B	Bagnold coefficient
b	second barycentric coordinate location
C	solar concentration ratio
C_p	specific heat
D	stochastically determined distribution factor
d	diameter
D_m	mass transfer diffusion coefficient
E_a	apparent activation energy
E_b	fractional, hemispherical black body emissive power
F	geometric view factor
f	blackbody fraction
f_v	particle volume fraction
Fr	Froude number
G	Gibb's free energy function
g	gravitational acceleration
H	total enthalpy, irradiation, relative flow height to particle diameter
h	height, molar enthalpy, convection coefficient
I	direct-normal irradiance
k	rate constant, thermal conductivity
k_o	apparent pre-exponential factor
L	empirically determined relative roughness, dimensionless bed depth
M	molar mass
m	mass, Weibull shape parameter
n	Avrami constant, integer number, moles
p	pressure
Q	heat
Q_{ext}	media extinction efficiency
q	net heat flux, measurands, heat rate
R	universal gas constant, thermal resistance, storage density rate of granular flow
r	molar consumption rate, position vector
S	total entropy, tensile stress, set, source/sink
T	temperature
t	time, boundary thickness, barycentric coordinate direction
U	overall heat transfer coefficient
u	unidirectional flow velocity
V	velocity, volume
W	work
w	width

X	conversion extent
y	mole fraction
y_{RS}	fitted response surface

Greek Letters

α	absorptance, conversion
β	fitting parameter, fitted flow parameter
γ	reaction order, fitted flow parameter
ΔH	enthalpy change of reaction
δ	Kronecker delta function, deviation from stoichiometry
ε	emittance
η	efficiency
θ	diffraction angle, inclination angle
ω	fitting coefficients for response surface
κ	linear absorption coefficient, collision momentum transfer proportionality constant
λ	wavelength
ν	elastic momentum transfer proportionality constant
Ξ	exergy
ξ	correlation length between solid particle chains, independent scattering correction factor
ρ	reflectance, density
σ	Stefan-Boltzmann constant, experimental uncertainty
τ	transmittance
φ	angle of internal friction
χ^2	chi-squared estimation
ψ	independent and normally distributed fitting error for response surface

Subscripts

abs	absorptive
ave	average
bed	particle bed
bulk	bulk flow quantity
CoO	cobalt (II) oxide
Co_3O_4	cobalt (II,III) oxide
comp	compressor
conv	convection coefficient
cool	cooled O_2 stream
cycle	CSP facility
D	destruction
eff	effective property
exhaust	depleted-O_2 airflow from turbine outlet
f	flow
fs	free surface of dense, granular flow
i	index
k	ray index
loss	lost to environment

n	normal direction
N	nearest neighbor
nb	neighboring cell
o	ambient / environment
p	particle
plug	plug flow
R	radiation
rad	radiative
res	residence
rxn	reaction
s	surface
sf	steady-flow
stop	residual particle layer
∞	environment conditions

Superscripts

^	unit vector
°	degree
.	time rate of change
’	integration variable
’’	flux
’’’	volumetric term
$\bar{}$	mean value
$\vec{}$	vector
=	matrix
-1	inverse

Acronyms

SSE	summed square of errors
RMSE	root-mean summed square of errors
2D,3D	two, three dimensions
CFD	computational fluid dynamics
FV	finite volume discretization
HFSS	high-flux solar simulator
MCRT	Monte-Carlo ray tracing
RTE	Radiative transport/transfer equation
STInGR	Solar Thermochemical Inclined Granular-flow Reactor
CAM28	$CaAl_{0.2}Mn_{0.8}O_{3-\delta}$
CAM	spray-dried aluminum-doped calcium manganites
MS	mass spectrometer
GC	gas chromatograph
PT	pressure transducer
VM	vibratory motor
DAQ	data acquisition system
XRD	X-ray diffractometry

SUMMARY

Solar thermochemical energy storage is a promising pathway towards extending the utility of concentrated solar power technologies. With continued research and development, solar electricity production can be decoupled from intermittent solar conditions, leading to an economically competitive, on-demand energy resource.

In this work, a two-step solar thermochemical cycle is proposed for energy storage based on the reduction/oxidation of metal oxides for direct integration into an air-Brayton cycle. The two steps encompass 1) the sensible heating and thermal reduction of metal oxides using concentrated solar irradiation, and 2) the extraction of stored sensible and chemical energy during re-oxidation of metal oxides for an air-Brayton cycle. A thermodynamic analysis is performed on the proposed cycle using Co_3O_4/CoO to assess the cycle potential and identify thermodynamic constraints. Thermogravimetric analysis is performed to extract thermal reduction kinetics of Co_3O_4 to evaluate operation in similar conditions to the solar thermochemical reactor for the proposed cycle.

Next, to realize the proposed cycle a solar thermochemical reactor is optimized to achieve solar energy storage within directly irradiated dense, granular flows of reactive metal oxides. The reactor concept is first evaluated using a design-stage heat and mass transfer model of a 5 kW_{th} laboratory scale reactor for Co_3O_4/CoO media. From this modeling, a 5 kW_{th} reactor is designed and evaluated using detailed heat and mass transfer modeling for aluminum-doped calcium manganite media. Lastly, the reactor performance is evaluated during experimentation in a high-flux solar simulator with aluminum-doped calcium manganite media.

CHAPTER 1. INTRODUCTION

1.1 Motivation

Continued research and development of solar technologies will support the United States' national goals of energy security, low-cost electricity resources, and environmental stewardship [1]. The United States' solar resources (*i.e.*, the sunlight incident on the earth's surface) are vast, with significant resource potential stretching from California to Texas, as pictured in a solar resource map in Figure 1.1.

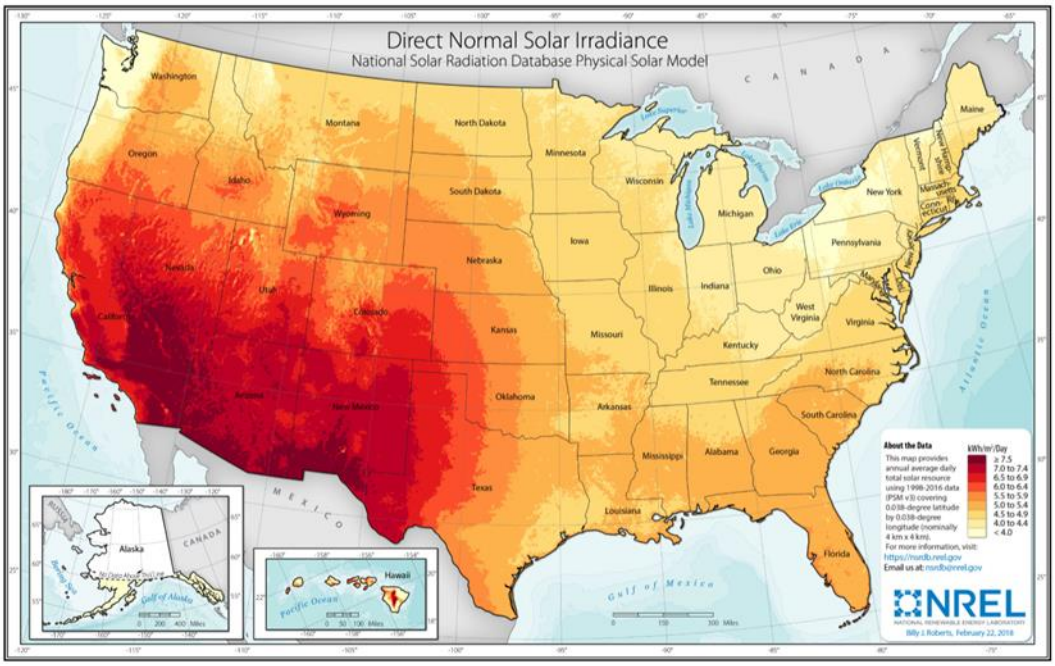

Figure 1.1. Contour map of solar resources in the United States

However, effectively harnessing the United States' solar resources is not without significant challenges as solar irradiation is dilute, unequally distributed, and intermittent.

In regions with increased solar irradiation (*e.g.* Southwest United States), the diluteness and unequal distribution of solar resources is addressed by concentrating solar irradiation

to generate high temperature process heat to produce electricity in a power cycle [*i.e.* concentrated solar power (CSP)]. With CSP technologies, dilute solar resources are converted into a deliverable, electrical resource. A process diagram of a CSP facility using a mirrored heliostat field for concentrating infrastructure is given in Figure 1.2.

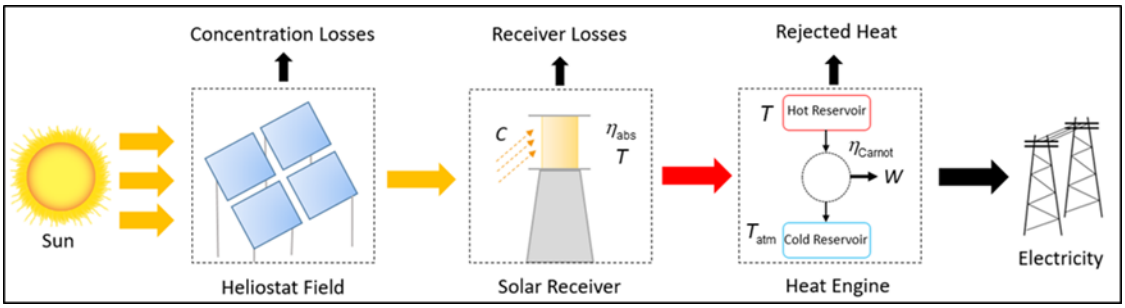

Figure 1.2. Process flow diagram of concentrated solar power facility with heliostat field solar concentrating infrastructure

In Figure 1.2, incident solar irradiation over a large area is reflected and concentrated to a focal point at a solar receiver using an array of reflective panels (*e.g.*, heliostats). Concentrated irradiation is absorbed by the solar receiver and is transferred as heat to a heat transfer fluid. Process heat is then delivered to a heat engine for electricity production. Solar concentrating facilities equipped with mirrored heliostat fields are capable of achieving focused solar concentrations approaching 1000 suns [2] (1 sun = 1 kW/m^2 [3]). Advancements in CSP technologies are being explored in the development of heat transfer materials and receiver designs operating in excess of 923 K for solar receivers [2] and developing dispatchable solar electricity using energy storage (*i.e.* decoupled from intermittent solar resources) [4]. CSP is predicted to approach cost competitiveness with fossil fuel power generation methods between 2020 and 2030 with approximately 50% of future cost reductions to be delivered by technological advancements including higher temperature operation and improved solar energy storage methods [5]. Increased operating

temperature is directly correlated to CSP operation efficiency as demonstrated by the ideal efficiency of a CSP facility. The ideal efficiency is modeled as the coupled absorption efficiency of a solar receiver η_{abs} and the Carnot cycle efficiency η_{Carnot}, given as:

$$\eta_{ideal} = \eta_{abs} \cdot \eta_{Carnot} = \left(1 - \frac{\sigma T^4}{IC}\right) \cdot \left(1 - \frac{T_{atm}}{T}\right) \tag{1.1}$$

where T is the operating temperature of the solar receiver and the high-temperature heat source for the Carnot cycle; σ is the Stefan-Boltzman constant; I is the incident solar resource (~1 sun); C is the concentration achieved via a concentrating infrastructure (100s – 1000s of suns); and T_{atm} is the low temperature reservoir for heat rejection in the Carnot cycle. The η_{ideal} is plotted in Figure 1.3 as a function of T for various C's and is compared to η_{abs} and η_{Carnot}. The η_{Carnot} captures the theoretical maximum work that can be extracted between two temperature reservoirs.

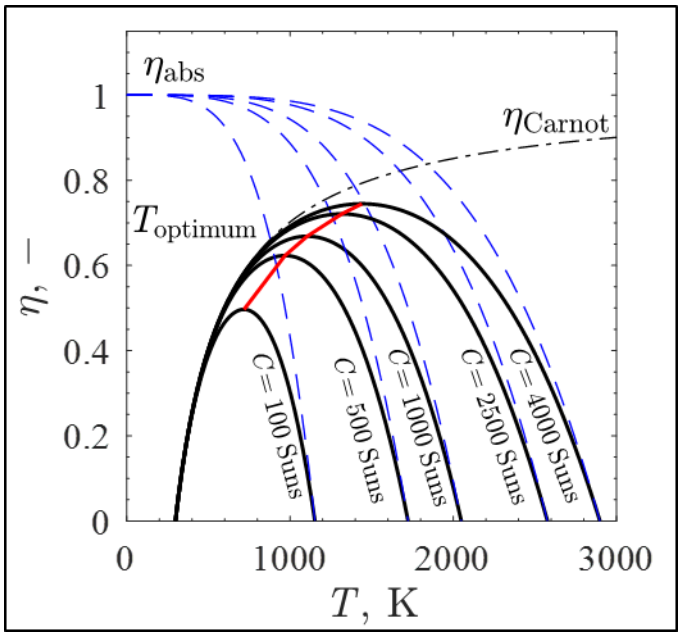

Figure 1.3. Ideal concentrated solar power facility efficiency as a function of solar receiver operating temperature and concentration ratio and compared to ideal absorption efficiencies of a black-body solar receiver and Carnot cycle

In Figure 1.3, η_{ideal} is maximized for heliostat field concentrating infrastructures with $C \rightarrow 1000$ suns with $1000 < T < 1300$ K.

Two-step solar thermochemical cycles for chemical and sensible heat storage integrated into an air-Brayton cycle were proposed for solar electricity production operating with $T > 923$ K and with energy storage [6-14]. Some proposed cycles use reduction / oxidation (redox) active metal oxide particles as both a heat transfer and thermochemical energy storage (TCES) material [8, 13]. In the first cycle step, the sensible heating and thermal reduction of particles is achieved using concentrated solar irradiation within a solar thermochemical reactor, represented as:

$$MO_{ox} + \Delta H_{red} \rightarrow MO_{red} + \nu O_2 \tag{1.2}$$

where ν is a stoichiometric coefficient; MO_{ox} is a metal oxide; MO_{red} is a metal oxide at a lower valance state; and ΔH_{red} is the endothermic reduction enthalpy. The high temperature reduced particles are stored in a thermally-insulated, chemically inert environment to achieve long-term sensible and chemical energy storage. In the second step of the cycle, the particles are re-oxidized using a compressed air-stream to deliver process heat to an air-Brayton cycle, represented as:

$$MO_{red} + \nu O_2 \rightarrow MO_{ox} + \Delta H_{ox} \tag{1.3}$$

The MO_{ox} is recycled back into the first step to complete the cycle. The cycle steps can be decoupled to promote on-demand electricity production during non-ideal solar conditions.

To promote the optimal performance of a two-step solar thermochemical cycle, a solar thermochemical reactor is designed to achieve effective and efficient solar energy storage within a given particulate media. A wide range of flow configurations are achieved for a given particulate media based on the relative magnitude of frictional and collisional particle interactions. Particular flow configurations support novel solar thermochemical reactors which promote direct irradiation, continuous operation, and match incident irradiation to the sensible heating and endothermicity of bulk, granular transport [15-17].

1.2 Objectives

The purpose of this study was to design, model, and test a laboratory-scale solar thermochemical inclined granular flow reactor to promote high temperature operation efficiency and chemical storage within a dense, granular flow of redox-active metal oxide particles. The reactor development was supported by investigations of the thermodynamic and kinetic potential of a newly proposed CSP technology: an air-Brayton cycle coupled to a two-step solar thermochemical cycle using redox-active metal oxides as a heat transfer and energy storage medium. The reactor was developed using thermodynamic and kinetics studies of viable metal oxides, extensive mass and heat transfer modeling of the solar thermochemical reactor, and the design, fabrication, and testing of the laboratory-scale reactor. A scalable solar thermochemical reactor was developed to be integrated with pre-existing concentrating solar and air-Brayton infrastructures to promote high temperature operation efficiencies and energy storage capability for CSP facilities.

The thesis objectives were as follows:

1. Detailed thermodynamic analysis of a metal oxide two-step solar thermochemical cycle to identify process limitations and to assess process impact
2. Evaluation of chemical reduction kinetics of a viable metal oxide particle, Co_3O_4
3. Development of a design stage heat and mass transfer model for initial investigation into laboratory scale solar thermochemical reactor to select an optimal design
4. Development of an extensive heat and mass transfer model of the complete laboratory scale solar thermochemical reactor design to provide further insight into experimental results and to assist in future reactor scale-up
5. Design, fabricate, and test a laboratory-scale solar thermochemical reactor

1.3 Thesis Overview

A combination of modeling and experimental work was performed to achieve the thesis objectives. Chapter 2 includes an extensive literature review: 1) state-of-the-art energy storage mechanisms for concentrated solar power, 2) extraction of reduction and oxidation kinetics for candidate metal oxide materials, 3) solar reactor / receiver designs; 4) mass and heat transfer methods for modeling solar reactor / receivers, and 5) characterization of dense, granular flows.

In Chapter 3, a thermodynamic analysis was performed on an air-Brayton cycle with an integrated two-step solar thermochemical cycle for heat storage based on particulate Co_3O_4/CoO redox reactions. A heat transfer model of an ideal, windowed, solar thermochemical reactor was developed to characterize the storage of incident irradiation in the cycle. The model was coupled to a thermodynamic analysis of the cycle to determine

ideal cycle efficiencies over a range of operating parameters and to identify major sources of irreversiblities.

In Chapter 4, a study using thermogravimetric analysis was performed to identify the rate limiting mechanisms and determine kinetic parameters for the reduction of Co_3O_4 for similar temperatures and environmental conditions in a solar thermochemical reactor for the two-step cycle. An Avrami-Erofeyev nucleation model with a power law partial pressure of O_2 dependency was proposed for reduction.

In Chapter 5, a solar thermochemical inclined granular-flow reactor concept was proposed. A $5kW_{th}$ reactor concept was evaluated using a design-stage heat and mass transfer model to identify optimal reactor design and operating conditions to promote thermal and chemical storage of incident irradiation within dense, granular flows of Co_3O_4 / CoO metal oxide particles. A parametric study was performed with varying cavity depth, particle inlet temperature, and solar concentration ratio to identify conditions which maximized conversion of Co_3O_4 to CoO and particle outlet temperature while preventing particle overheating.

In Chapter 6, a method was presented for mapping directional, irradiation modeled via a Monte Carlo ray-tracing model to commercial computational heat transfer and fluid dynamics models. The method was well-suited to models with highly directional and spatially varying radiative inputs as is common with solar receivers and reactors. Four case studies were performed on a 5 kW_{th} scale solar thermochemical inclined granular flow reactor to evaluate the method and further inform reactor design and operation.

In Chapter 7, a 5 kW_{th} laboratory-scale solar thermochemical inclined granular-flow reactor was designed. The reactor design was tuned to accommodate aluminum-doped calcium manganite granular powders as a thermochemical energy storage media within the reactor due to their promising advantages over Co_3O_4 in CSP applications. Bulk, granular flow characteristics of the granular powders were extracted using a custom tilt-flow rig and particle image velocimetry (PIV) analysis. Flow characteristics were applied to steady-flow mass transfer models of dense, granular flows and employed in a detailed heat and mass transfer model. Modeling was performed in ANSYS Fluent 17.1 to evaluate the performance of candidate granular flows, to capture the final geometry and materials of the laboratory scale reactor within the high-flux solar simulator, and to evaluate the influence of evolved O_2 transport within the reactor on the chemical reduction of the dense granular flow. Reactor performance was evaluated using aluminum-doped calcium manganite granular powders and compared to a state-of-the-art inert, sensible storage granular media Accucast ID50 for CSP applications. A new metric, the energy density storage rate, was used in evaluating granular flows in CSP applications and determining their applicability at various scales.

In Chapter 8, the experimental methodology and performance of the 5 kW_{th} STInGR was presented during high-temperature operation within the HFSS using spray-dried aluminum-doped calcium mangnanite granular powders as a TCES media. Steady-state system response was examined for reactor geometry and high-flux solar simulator operating conditions which avoided the formation of significant particle agglomerations, promoting continuous reactor operation.

In Chapter 9, the study conclusions and technical contributions to the field were reviewed. Recommendations for future work and research opportunities which have been produced from this work were presented.

CHAPTER 2. LITERATURE REVIEW

2.1 Methods / Materials for Energy Storage

Three methods were employed to store solar heat for use in CSP: sensible energy storage (SES), latent energy storage (LES), and thermochemical energy storage (TCES). SES systems store sensible energy using heat transfer fluids or inert granular materials (e.g., oil, synthetic oil, molten salts, sand, etc.). SES was commonly used for commercial CSP systems, but affords numerous challenges due to high pressure components, cost of various heat transfer media, and temperature limitations that impede facility operations [18]. This was especially prevalent with molten salts (e.g., $NaNO_3$ and KNO_3 mixtures) that solidify below 473 K and often degraded at temperatures greater than 873 K [19, 20]. Maintaining these temperatures was challenging, with the maximum temperature limiting the facility output work potential. An additional SES system was the falling particle receiver, which used a curtain of ceramic particles or proppants as a thermal storage medium. The particles were predicted to heat rapidly to temperatures greater than 873 K and are temporarily stored to retain sensible heat while remaining chemically stable. The high temperature particles were proposed as an on-demand process heat source to the working fluid of a power cycle [19, 21].

CSP facilities with LES capability store heat in a phase change material (PCM) with a high heat of fusion. Heat is stored when a thermal gradient exists between the heat transfer fluid (HTF) and the PCM. A heat exchanger transfers heat to the PCM, driving the PCM phase change. Heat extraction occurs when solar conditions fluctuate and the HTF becomes cooler than the PCM, removing stored heat from the material. Challenges to LES have

included the selection of a PCM and the large thermal resistance between the PCM and HTF. It was proposed that a favorable PCM should include high thermal conductivity and a constant charge/discharge temperature during phase change tailored to the working conditions of the CSP facility [22, 23]. The low thermal conductivities of most PCMs have required specialized storage / heat exchange units with a series of highly conductive fins to promote heat transfer [24]. One of the most extensively studied PCMs includes $NaNO_3$. Previous works have assessed the eutectic mixture of $NaNO_3$ / KNO_3 in a 100 kW_{th} latent heat storage system. The system successfully stored and extracted heat from the PCM, providing process heat to a Steam – Rankine cycle despite low HTF temperatures [25].

TCES systems use concentrated solar irradiation as process heat to drive reversible chemical reactions, enabling the sensible and chemical storage of sunlight in high temperature endothermic reduction reactions. Stored heat is extracted from the reverse, exothermic oxidation reaction, releasing heat to drive power cycles. Previous work resulted in an ammonia-based TCES delivering process heat at 475 °C to a power cycle [26]. Additional TCES studies included two-step solar thermochemical cycles based on stoichiometric metal oxide redox reactions [27-34], with numerous redox pairs evaluated for both energy storage and extraction potential [14, 35]. Evaluations encompassed both thermogravimetry and economic analyses of various metal oxides with the most promising redox pairs including BaO_2/BaO, Mn_2O_3/Mn_3O_4, and Co_3O_4/CoO [14]. Complete reduction and oxidation occurred between 1073-1273 K with the higher energy density of Co_3O_4/CoO making it a more attractive storage medium. Recent kinetics analyses have further demonstrated the promise of Co_3O_4/CoO as a solar thermochemical energy storage material [9, 36-38]. Additional metal oxides investigated for TCES include redox-active

mixed-ionic/electronic conducting (MIEC) materials with perovskite oxide structures in the generic form $ABO_{3-\delta}$. MIECs offer a distinct advantage over binary metal oxides as they maintain crystal structure across a wide range of oxygen non-stoichiometry and exhibit significantly high ionic and electronic conductivities, properties which facilitate increased energy storage density, increased reduction extent, and rapid kinetics. Additionally, MIEC thermodynamic properties were tuned during synthesis with the inclusion of various material combinations at the A and B sites. Custom MIECs were produced to promote thermal reduction at temperatures typical of CSP facilities, to include compositions of less expensive materials compared to binary metal oxides [39], and to increase the mass – specific reduction enthalpy leading to reduced material handling costs. Recent studies investigated the redox capability and stability of perovskite MIECs including $Sr_xLa_{1-x}Mn_yO_{3-\delta}$ [40] , $LaMn_{1-x}Co_xO_{3-\delta}$ [41], $La(B_{1-x}B'_x)\ O_{3-\delta}$ (where BB' is FeCO, MnCO, MnNi, or CoCu) [42], $La_{1-x}Sr_xMnO_{3-\delta}$ [43], $La_xSr_{1-x}Co_yMn_{1-y}O_{3-\delta}$, $La_xSr_{1-x}Co_yFe_{1-y}O_{3-\delta}$, $CaAl_{0.2}Ti_{0.8}O_{3-\delta}$, and $CaAl_{0.2}Mn_{0.8}O_{3-\delta}\ O_{3-\delta}$ (CAM28), with CAM28 exhibiting promising storage capacity per mass of material with reduced material cost [39, 44].

Calcium-based perovskite oxide particles were proposed as alternatives to binary metal oxide particles as heat transfer and thermochemical energy storage media [44-50]. Calcium-based perovskite oxides are more advantageous over binary metal oxides due to a continuum of redox states over a range of thermodynamic conditions, tunable thermodynamic properties when synthesized with various dopants, rapid kinetics, and synthesis from abundant, less massive constituent materials. Detailed thermodynamic characterization of various calcium-based perovskites [44] identified an aluminum-doped

calcium manganite ($CaAl_{0.2}Mn_{0.8}O_{3-\delta}$) as a promising candidate for solar thermochemical applications.

2.2 Reaction Kinetics of Metal Oxide TCES Media

Metal oxides generally follow the principles of solid-state kinetics, based on a variety of models and mechanisms that include nucleation and nuclei growth, geometrical contraction, diffusion, and simple reaction order [51]. A number of limiting mechanisms were proposed in previous works for Co_3O_4 thermal reduction, including nucleation and nuclei growth [52], heat transfer [52, 53], and oxygen diffusion [53].

Prior work using non-isothermal thermal reduction and isothermal re-oxidation in air with a thermogravimetric analyzer (TGA) determined an apparent activation energy of 960 $kJ \cdot mol^{-1}$ for Co_3O_4 thermolysis using a nucleation model [53]. Another study used a TGA to perform multi-cyclic temperature reduction and re-oxidation in air or O_2, finding apparent activation energies of 439 and 892 $kJ \cdot mol^{-1}$ for thermal reduction in air and O_2, respectively, using a model based on thermodynamic driving force [52]. A recent work used downstream O_2 measurements in an air-blown furnace system with a simplified kinetic model, resulting in apparent activation energy of 723 $kJ \cdot mol^{-1}$ for Co_3O_4 thermal reduction [54].

Other works have analyzed the kinetics of other metal oxide redox pairs for solar applications, including Zn/ZnO [55-63], SnO/SnO_2 [62-64], FeO/Fe_3O_4 [61, 65], Mg/MgO [66], MnO/Mn_2O_3 [67, 68], perovskites [69], and ferrites [65, 70-72]. These and other redox pairs have been examined predominantly for solar thermal syngas production and are detailed in an extensive review [73].

2.3 Solar Receiver / Reactor Designs

Previous works examining an array of solar receiver / reactor technologies for thermochemical energy storage have employed a range of different receiver / reactor configurations for different applications and materials, including rotary kilns [74-79], packed beds [17, 80, 81], fluidized beds [82-84], air receivers [85], and falling particle receivers [86, 87]. Direct irradiation of energy storage media was proposed to achieve high temperatures (> 1073 K) in solar thermochemical reactors, as the media act as a radiant absorber, reactor insulation, and chemical reactant [88]. This method is proposed to reduce inherent irreversibilities (i.e. exergy destruction) introduced by indirect irradiation, where the heat was conducted through reactor walls to the storage media [3]. Directly irradiated Co_3O_4 thermal reduction and subsequent CoO off-sun oxidation were successfully demonstrated in an atmospheric air environment using a batch process rotary kiln [32]. Rotary kilns and fluidized bed reactors introduced reactor specific engineering challenges including high-temperature moving components and controlled residence times for entrained particles. An advantage of packed bed reactors and falling particle receivers over other reactor styles was their relative mechanical simplicity, with such systems often having used gravity or simple lift mechanisms to transport storage media. A method promoting complete reduction of storage media was proposed using a quartz window to directly irradiate and rapidly heat the storage media while maintaining a reduced O_2 partial pressure via vacuum or an inert gas. A 10-20 kW_{th} gravity fed solar thermochemical receiver/reactor to thermally reduce ZnO combined the primary elements of both a falling particle receiver and a packed bed reactor with a quartz window [89]. The solar thermochemical reactor was mounted in the vertical position with concentrated irradiation

entering through a quartz window located at the reactor top. ZnO particles were directly irradiated and continuously distributed over 15 inclined Al_2O_3 tiles which formed an inverted cone around the window central axis. ZnO particles were introduced along the top of a tile, transported by gravity into a region of direct irradiation, and thermally reduced to produce Zn(g) and O_2. Gravity-driven particles along inclined slopes simplified mass transport and imparted some residence time control for a continuous, directly-irradiated reactor concept.

2.4 Heat and Mass Transfer Modeling of Solar Receivers / Reactors

Detailed computational modeling was used to evaluate and optimize the designs of solar receivers/reactors. Heat transfer, fluid dynamics, radiative exchange, and chemical reaction phenomena were captured via computational solutions of the corresponding transport equations. The coupling of these equations was well documented [90, 91] and supported by commercial computational fluid dynamics (CFD) software [92]. Accurate modeling of heat and mass transfer phenomena in solar receivers/reactors was a necessary endeavor to further understand the limitations associated with solar receiver/reactor concepts, to optimize geometries and operating conditions, and to predict performance from the laboratory-scale to pilot and commercial scales [93]. Solar thermochemical reactor modeling efforts combined Monte Carlo ray-tracing with radiative exchange to determine radiative distributions within a given reactor cavity for both diffuse and specular reflecting surfaces [94, 95]. Radiative distributions were coupled with energy conservation relationships within the reacting media and across cavity surfaces to assess reactor performance [93, 96-101].

Monte Carlo ray-tracing (MCRT) and finite volume approximations to the radiative transport equation (FV–RTE) are two methods for modeling solar inputs in receiver/reactor models. MCRT is a statistical method to predict radiative absorption by surfaces and participating media with specified radiative properties [102]. Challenges in implementing MCRT for solar receivers/reactors have occurred when modeling optically thick media, wavelength/temperature-dependent radiative properties, and complex geometries. FV-RTE methods such as the discrete ordinates (DO) method are more suited to these conditions and are supported in computational software [103]. FV-RTE methods were computationally expensive for domains requiring high mesh resolutions, like combined models of solar receivers/reactors and collecting/generating infrastructures [104, 105]. Fortunately, some studies have used MCRT to model the concentrated solar input to the receiver/reactor, and FV-RTE to capture internal radiative transport within the reactor [104]. If paired appropriately, the models are a powerful tool for modeling radiative heat transfer to and within solar receivers/reactors.

Prior methods for pairing MCRT and FV-RTE have been implemented by employing 1) non-overlapping or 2) overlapping domains. In non-overlapping schemes [104-107], models of the solar input are mapped to the CFD model at a common boundary through an intensive process of translating directional solar inputs to intensity boundary conditions. Non-overlapping schemes may be functionally energy-conservative. However, they require fine meshes that are directionally aligned with the solar input to mitigate discretization errors which extend computational time and inhibit CFD convergence [105]. Restricting non-overlapping schemes to two-dimensional domains has been recommended [105].

In overlapping schemes [108-112] some portions of the MCRT and CFD modeling domains were spatially coincident. In this scheme, the external radiative input was modeled from the collector/generator until it is 1) absorbed by internal receiver/reactor surfaces or media, modeled as boundary or volumetric sources, respectively; or 2) rejected from the receiver/reactor by reflection, transmission, or scattering. Re-emission within the receiver/reactor was captured separately in the CFD model. For diffuse surfaces, overlapping schemes permit coarser CFD meshes that are not necessarily directionally aligned with the solar input. Systematic errors have resulted from the representation of curved geometries in the MCRT domain as planar approximations in the CFD domain [112] but can be mitigated by careful meshing and mapping. Absorbed rays in overlapping schemes were implemented as surface [113] or sub-surface [114, 115] averaged fluxes. This approximation has maintained energy conservation but has not preserved spatial variation between the MCRT and CFD models. Alternatively, absorbed rays were binned into a grid within the MCRT modeling domain to produce a spatial irradiation profile, which may then be interpolated to the CFD mesh [108]. For sufficiently fine grids and meshes, this method preserved spatial variation but did not guarantee energy conservation.

2.5 Bulk Granular Transport in Solar Receivers / Reactors

Optimal storage of concentrated solar irradiation in particles has required solar receivers / reactors designed for the bulk transport behavior of granular media. Granular media was observed to exhibit traits of solids (*i.e.*, densely-packed particle structures), gases (*i.e.*, dilute particle collisions), or liquids (*i.e.*, dense particle flows) based on the relative impact of frictional and collisional effects [116-118]. Solid granular structures were achieved within solar thermochemical reactor designs using rotary kilns [32, 74, 75]

and packed beds [17, 81, 119, 120]. Dilute granular transport was achieved within solar receivers and solar thermochemical reactors using falling particle curtains [86, 121-124], fluidized beds [82-84] , and low-density flows along steep inclined planes [89, 125, 126]. Dense, granular flows were achieved within solar receivers / reactors using slip-stick planes [127] and along inclined surfaces [109, 128]. Steady, dense, granular flows are promising for thermochemical energy storage as they achieve continuous transport of granular media with controlled particle residence times. However, characterization of steady, dense, granular flows was challenging due to the complex frictional and collisional behavior of particle-particle and particle-surface interactions [116]. Dimensional scaling arguments were proposed to extract predictive, steady granular flow characteristics of various granular materials along roughened inclined planes [118, 129-132].

CHAPTER 3. THERMODYNAMIC ANALYSIS OF COBALT OXIDE CYCLE

3.1 Introduction

An Air Brayton cycle was thermodynamically examined with an integrated two-step solar thermochemical cycle for heat storage based on Co_3O_4/CoO redox reactions. The first step is the thermal reduction of Co_3O_4 using concentrated solar irradiation as process heat, represented as:

$$Co_3O_4 \rightarrow 3CoO + 1/2\,O_2 \quad \Delta H_{298.15\ K} = 196.2\ kJ \cdot mol^{-1} \tag{3.1}$$

The particles can then be stored in an inert environment and re-oxidized in the reversible second step that does not require solar energy and releases heat, represented as:

$$3CoO + 1/2\,O_2 \rightarrow Co_3O_4 \quad \Delta H_{298.15\ K} = -196.2\ kJ \cdot mol^{-1} \tag{3.2}$$

Co_3O_4 is then recycled to the first step, completing the cycle. The steps of the cycle may be decoupled, enabling the long-term chemical storage of sunlight to provide the necessary heat inputs to the power cycles to produce on-demand electricity. This work built on previous analyses that examined thermodynamic constraints for CSP facility operation and two-step solar thermochemical cycles based on metal oxide redox reactions for fuel production [133-137].

Ranges for reactor temperature and O_2 partial pressure were determined thermodynamically to identify temperatures above which the $Co_3O_4 \rightarrow 3CoO + ½O_2$ reaction is spontaneous (i.e., $\Delta G \leq 0$). ΔG is given as a function of temperature and O_2

partial pressure in Figure 3.1. Three different O_2 partial pressures were plotted to show the impact of O_2 on the reaction. ΔG is positive at 800 K for p_{O2} = 0.001 bar, indicative of a favorable back reaction, and decreases monotonically with increasing temperature until reaching T = 1093.0 K, where the reaction becomes spontaneous. The same trend for ΔG is shown for both p_{O2} = 1 bar and 6 bar where the reaction is shifted further to the right according to Le Chatalier's principle, resulting in equilibrium temperatures of 1252.8 K and 1351.8 K respectively, where the back reaction is favored.

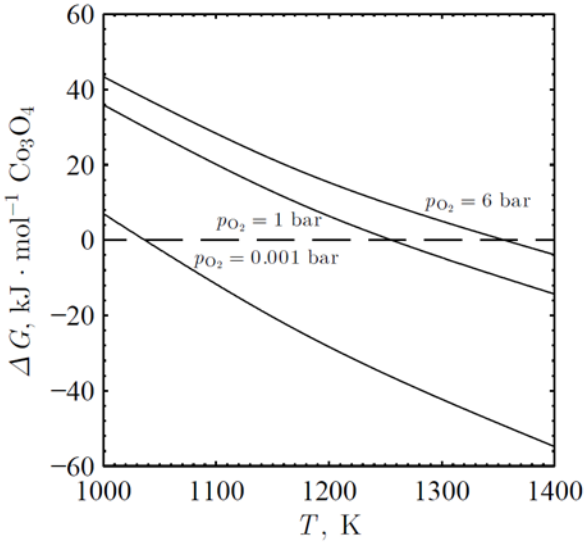

Figure 3.1. Gibb's free energy function difference for the Co3O4 → 3CoO + ½ O2 reaction as a function of temperature at partial O2 pressures of 0.001 bar, 1 bar, and 6 bar

3.2 Thermodynamic analysis

The Air Brayton cycle integrated with the two-step solar thermochemical heat storage cycle is schematically depicted in Figure 3.2 with relevant energy flows. Concentrated solar irradiation enters the solar thermochemical reactor through a quartz window and impinges directly upon Co_3O_4/CoO particles entering from a cold storage bin. Particles are heated rapidly to $T_{reactor}$ and undergo thermolyses to O_2 and CoO. The solar thermochemical reactor is maintained at a reduced pressure by a vacuum pump to ensure favorable

thermodynamics and complete conversion for the Co_3O_4 thermal reduction at lower temperatures. The O_2 evolves from the particles and is continuously extracted from the cavity, driving a non-equilibrium process, cooled to ambient temperature, and removed through the vacuum pump. CoO particles are fed into a hot storage bin and then introduced to a re-oxidizer. CoO particles flow in the opposite direction to a pressurized air flow, entering the re-oxidizer from an air compressor. The entering air comes into contact with particles that are cooled by the upstream flow and partially reacted. The lower temperatures further drive the re-oxidation of the CoO particles to Co_3O_4 due to a favorable $3CoO + ½O_2$ reaction at lower temperature as shown in Figure 3.1. This enables the air stream to extract both the sensible and reaction heat. An O_2-depleted, pressurized air flow exits the re-oxidizer at its maximum temperature and is expanded across a turbine to produce work. In actual practice, particle feeding to the re-oxidizer from the hot storage bin may be accomplished through a lock or screw-type feeder [17] while a filter or similar component would prevent entrained particles from exiting the re-oxidizer and entering the turbine. CoO and/or Co_3O_4 particles exit the re-oxidizer depending on conversion and are stored in a cold bin until being re-introduced into the solar thermochemical reactor.

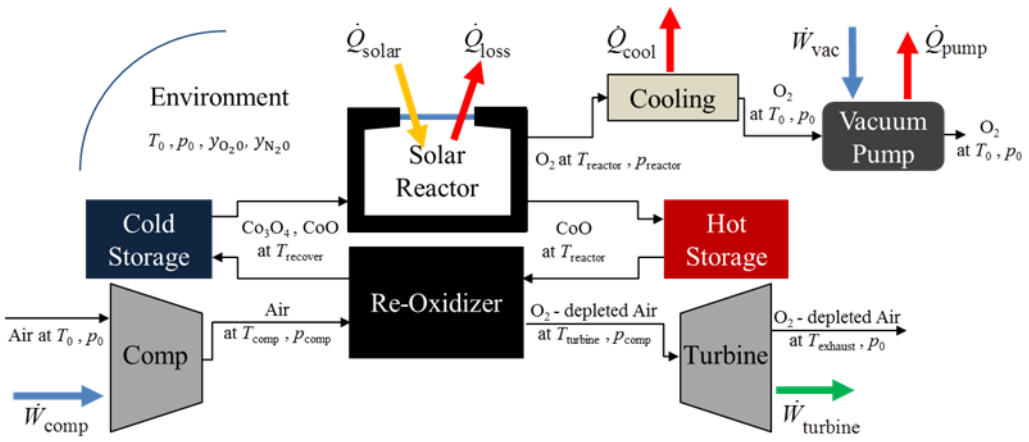

Figure 3.2. A flow diagram of the Air Brayton cycle with an integrated two-step solar thermochemical heat storage cycle based on Co3O4/CoO redox reactions is depicted with relevant heat and work flows into and out of the system

The thermodynamic analysis assumes a continuous, steady-state cycle to determine maximum theoretical efficiencies and identify major sources of irreversibility. In reality, the solar thermochemical reactor will be oversized compared to the re-oxidizer, enabling significant storage capacity of CoO during periods when sunlight is unavailable. The work required to transport the particles and overcome pressure losses throughout the system were neglected along with kinetic and potential energies. Thermophysical properties were extracted from HSC. The analysis was normalized to 3 mol/s of CoO exiting the solar thermochemical reactor. Steady flow rates of particles are assumed to pass between the solar thermochemical reactor and the re-oxidizer in the analysis. The environmental temperature and pressure (i.e., the dead state) were T_0 = 298.15 K and p_0 = 1 bar, respectively, and the molar fractions of N_2 and O_2 in air were assumed as $y_{N2,0}$ = 0.79 and $y_{O2,0}$ = 0.21, respectively [139]. Ideal gas and solution behaviors were assumed for gases and solids, respectively.

The CoO particles leaving the solar thermochemical reactor at T_{reactor} are deposited in a well-insulated and reversible hot storage bin. The particles enter the re-oxidizer and flow in the opposite direction of a stream of pressurized air introduced from an air compressor. Air from the environment composed of O_2 and N_2 is isentropically compressed to fixed pressure. The rate of work into the compressor is given as:

$$\dot{W}_{\text{comp}} = \dot{n}_{\text{air}} \Delta H \,|_{y_{O_2,0}O_2, y_{N_2,0}N_2 \text{ at } T_0 \rightarrow T_{\text{comp}}} \tag{3.3}$$

where ΔH is the total enthalpy change and $\dot{n}$ is the molar flow rates. Hot CoO particles are introduced at one end of the re-oxidizer at T_{reactor} and move in a counter flow to a pressurized air stream. Operation at increased O_2 partial pressures enables airflow temperatures greater than T_{reactor} to occur at the turbine due to favorable thermodynamics at higher temperatures according to Le Chatelier's principle as shown in Figure 3.1. The direct contact heat exchanger allows the O_2 to react with the CoO particles, recovering both sensible and reaction heat. The maximum turbine inlet temperature, $T_{\text{turbine,max}}$, was determined by calculating the temperature for $\Delta G = 0$ for $3CoO \rightarrow Co_3O_4 + \frac{1}{2}O_2$ using the partial pressure of O_2 of the air stream exiting the re-oxidizer. Air flow temperatures greater than $T_{\text{turbine,max}}$ are not thermodynamically favored as the reaction is no longer spontaneous. T_{turbine} is assumed equivalent to $T_{\text{turbine,max}}$ if supported by an energy balance across the re-oxidizer. The minimum temperature of the exiting particle stream, $T_{\text{recover,min}}$ was equal to T_{comp}. Chemical equilibrium between the incoming air stream and the exiting particle stream was employed in addition to an energy balance across the re-oxidizer to determine T_{recover} and the conversion extent of CoO to Co_3O_4 at the particle outlet. The re-oxidizer was assumed to be well-insulated and the particles and fluid were assumed to be in local thermal equilibrium at both the particle inlet and outlet. Air entering the re-oxidizer is assumed to heat rapidly to T_{recover}. T_{recover} and T_{turbine} were determined by applying the described thermodynamic constraints bounding the temperatures and applying an energy balance, given as:

$$\begin{aligned} 0 = {} & \dot{n}_{Co_3O_4,\text{recover}} \Delta H\big|_{3CoO \text{ at } T_{\text{reactor}} + \frac{1}{2}O_2 \text{at } T_{\text{comp}} \rightarrow Co_3O_4 \text{ at } T_{\text{recover}}} + \\ & \dot{n}_{CoO,\text{recover}} \Delta H\big|_{CoO \text{ at } T_{\text{reactor}} \rightarrow T_{\text{recover}}} + \\ & \left(\dot{n}_{\text{air}} - \frac{1}{2} \dot{n}_{Co_3O_4,\text{recover}} \right) \Delta H\big|_{y_{O_2,\text{turbine}} O_2, y_{N_2,\text{turbine}} N_2 \text{ at } T_{\text{comp}} \rightarrow T_{\text{turbine}}} \end{aligned} \tag{3.4}$$

T_{recover} and T_{turbine} were solved iteratively with convergence criteria of < 0.1 K for both temperatures and the CoO and Co_3O_4 fractions at the outlet with a convergence criterion of < 10^{-4}. T_{turbine} was verified within a turbine operation range with temperatures (1000 – 1600 K) and pressures (5-30 bars) as specified in [140]. The conversion extent of CoO to Co_3O_4 in the flow is given as:

$$X = \frac{3\dot{n}_{\text{Co}_3\text{O}_4,\text{recover}}}{\dot{n}_{\text{CoO,reactor}}} \tag{3.5}$$

The re-oxidizer was provided excess O_2 for all cases considered, thus X is dependent upon equilibrium conditions and the energy balance across the re-oxidizer. The rate of exergy destruction across the re-oxidizer was used to assess performance, given as:

$$\begin{aligned}\dot{\Xi}_{\text{D,re-oxidizer}} = {} & \dot{n}_{\text{Co}_3\text{O}_4,\text{recover}}\,\Delta\Xi_{\text{f}}\big|_{3\text{CoO at } T_{\text{reactor}} + \frac{1}{2}\text{O}_2 \text{at } T_{\text{comp}} \rightarrow \text{Co}_3\text{O}_4 \text{ at } T_{\text{recover}}} + \\ & \dot{n}_{\text{CoO,recover}}\,\Delta\Xi_{\text{f}}\big|_{\text{CoO at } T_{\text{reactor}} \rightarrow T_{\text{recover}}} + \\ & \left(\dot{n}_{\text{air}} - \frac{1}{2}\dot{n}_{\text{Co}_3\text{O}_4,\text{recover}}\right)\Delta\Xi_{\text{f}}\big|_{y_{\text{O}_2,\text{turbine}}\text{O}_2, y_{\text{N}_2,\text{turbine}}\text{N}_2 \text{ at } p_{\text{comp}}, T_{\text{comp}} \rightarrow p_{\text{comp}}, T_{\text{turbine}}}\end{aligned} \tag{3.6}$$

where $\Delta\Xi_{\text{f}}$ is the change in exergy flow (both mechanical and chemical). The particles exiting the re-oxidizer enter the well-insulated cold storage bin. The O_2 depleted air exiting the re-oxidizer is fed directly into the turbine. Expansion across the turbine to p_0 was assumed isentropic, and the rate of work across the turbine is given as:

$$\dot{W}_{\text{turbine}} = \left(\dot{n}_{\text{air}} - \frac{1}{2}\dot{n}_{\text{Co}_3\text{O}_4,\text{recover}}\right)\Delta H\,|_{y_{\text{O}_2,\text{turbine}}\text{O}_2, y_{\text{N}_2,\text{turbine}}\text{N}_2 \text{ at } T_{\text{turbine}} \rightarrow T_{\text{exhaust}}} \tag{3.7}$$

CoO/Co_3O_4 particles are taken from the cold storage bin and fed directly to the solar thermochemical reactor. The solar thermochemical reactor was modeled as directly

irradiated, requiring a quartz window that reflects a small portion of incoming solar irradiation to the environment, schematically shown in Figure 3.3.

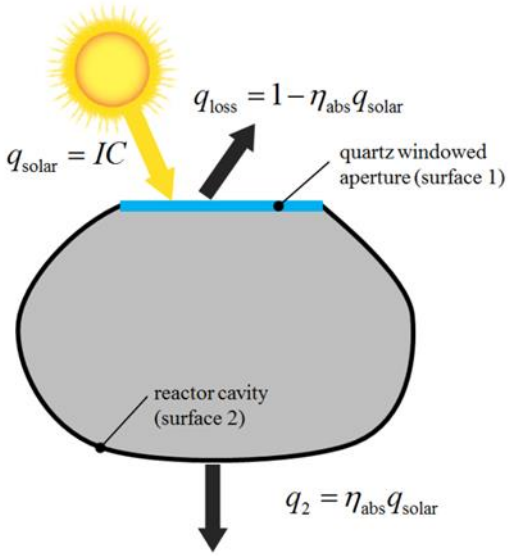

Figure 3.3. A schematic depiction of a simplified solar thermochemical reactor geometry for radiative exchange analysis between a quartz window (Surface 1) and reactor cavity (Surface 2) with incident concentrated solar irradiation passing through the window and directly impinging on the reactor cavity

However, the spectral characteristics of the quartz window help to mitigate re-radiative losses as the window temperature is lower than the cavity temperature. A radiative exchange model was employed to determine the absorption efficiency of a solar thermochemical reactor composed of two surfaces: a quartz window (Surface 1) and a reactor cavity (Surface 2). The reactor cavity temperature was fixed to a specified temperature corresponding to typical CSP operation with a concentration ratio of C=1000 suns and direct normal irradiance of I=1 kW/m^2. The relevant parameter is the area ratio between the two surfaces, therefore, a detailed cavity geometry is not specified. A semi-gray, two-band approximation was used to account for spectral dependency of the quartz glass: Semi-transparent and opaque wavelength intervals over the ranges of (1) 0- λ_c and

(2) λ_c-∞, respectively, where λ_c = 4 μm [141]. Both surfaces were considered as diffuse and isothermal. The radiative exchange equation over the semi-transparent band (i.e., radiative band 1) for n surfaces is given as [142]:

$$\frac{q_i^{(1)}}{1-\rho_i} - \sum_{j=1}^{N}\left(\frac{\rho_j}{1-\rho_j}\right)F_{i\text{-}j}q_j^{(1)} + H_{0,i}^{(1)} = \frac{\alpha_i}{1-\rho_i}\sigma T_i^4 f\left(T_i\lambda_c\right) - \sum_{j=1}^{N}\left(\frac{\alpha_j}{1-\rho_j}\right)F_{i\text{-}j}\sigma T_j^4 f\left(T_i\lambda_c\right) \tag{3.8}$$

where q is the net radiative heat flux, ρ is the slab reflectance, F is the view factor, α is the slab absorptance, H_0 is the external irradiation to a surface, σ is the Stefan-Boltzmann constant, T is the surface temperature, f is the radiative fractional function, and i and j are summing indices representing the emitting surface and incident surface(s) respectively. The incoming concentrated irradiation, assumed to be uniformly distributed and incident only on the cavity in the semi-transparent band, was represented as:

$$H_{0,2}^{(1)} = \frac{\tau_1 IC}{A_r} \tag{3.9}$$

where τ_1 is the slab transmittance for the quartz glass, I is the direct-normal solar irradiance, C is the solar concentration ratio, and A_r is the ratio of the areas of the cavity to the quartz window. The radiative exchange equation over the opaque bandwidth (i.e., radiative band 2) for n surfaces is given as:

$$\frac{q_i^{(2)}}{\varepsilon_i} - \sum_{j=1}^{N}\left(\frac{1}{\varepsilon_j} - 1\right)F_{i\text{-}j}q_j^{(2)} = \left(1 - f\left(T_i\lambda_c\right)\right)\sigma T_i^4 - \sum_{j=1}^{N}F_{i\text{-}j}\left(1 - f\left(T_j\lambda_c\right)\right)\sigma T_i^4 \tag{3.10}$$

where ε is the surface emittance. The net radiative flux between the reactor cavity and the quartz window in both radiative bands was solved using equations 8-10 along with

an energy balance considering external convection, transmitted radiative energy through the quartz window, and radiative exchange to and from the surroundings, given as:

$$q_1^{(1)} + q_1^{(2)} = \tau_1 \left(\frac{q_1^{(1)} - \alpha_1 f(T_1 \lambda_c) \sigma T_1^4}{1 - \rho_1} \right) - h_1 \left(T_1 - T_0 \right) - \alpha_1 f(T_1 \lambda_c) \sigma T_1^4 - \varepsilon_1 \left[1 - f(T_1 \lambda_c) \right] \sigma T_1^4 + \sigma T_0^4 \tag{3.11}$$

where h_1 is the external convective heat transfer coefficient determined from free convection of a vertical surface [143], α_1 is the absorptance, τ_1 is the transmittance, ρ_1 is the reflectiance, ε_1 is the emittance of the quartz window, and T_1 refers to the window temperature.. The system of non-linear equations was solved iteratively until the window temperature converged to < 0.1 K. The results were used to determine reactor absorption efficiencies for a range of reactor cavity temperatures and surface emittances, given as:

$$\eta_{abs} = \frac{\left[q_2^{(1)} + q_2^{(2)} \right] A_r}{IC} \tag{3.12}$$

$q_2^{(1)} + q_2^{(1)}$ was assumed solely to heat incoming particles and drive the chemical reaction. The reaction absorption efficiency was compared to the theoretical absorption efficiency assuming a perfectly insulated, blackbody, cavity-receiver with no convective/conductive heat losses to the environment, given as:

$$\eta_{abs,ideal} = 1 - \frac{\sigma T_{reactor}^4}{IC} \tag{3.13}$$

The incoming particles to the solar thermochemical reactor were assumed to enter the reactor without a carrier gas and completely reduce to CoO in a non-equilibrium reaction with O_2 being continually removed. Spontaneous reaction occurs at $T_{reactor} \geq$ 1036.6 K at p_{O2} = 0.001 bar where $\Delta G \leq 0$ for $Co_3O_4 \rightarrow 3CoO + ½O_2$. Therefore, $T_{reactor} >$

1036.6 K were considered to assess the impact of additional sensible heat storage coupled to higher re-radiative heat losses. T_{reactor} = 1050 K was chosen as it is just above the temperature where the Co_3O_4 thermal reduction is spontaneous at 0.001 bar, ensuring conversion from Co_3O_4 to CoO and O_2. The process heat required for complete reduction in the solar thermochemical reactor, the required concentrated solar irradiation (utilizing η_{abs} calculated from the radiation exchange model), and heat rejected to the surroundings are given, respectively, as:

$$\dot{Q}_{\text{reactor}} = \dot{n}_{\text{Co}_3\text{O}_4,\text{recovered}} \Delta H \big|_{\text{Co}_3\text{O}_4 \text{ at } T_{\text{recovered}} \rightarrow 3\text{CoO}+\frac{1}{2}\text{O}_2 \text{ at } T_{\text{reactor}}} + \dot{n}_{\text{CoO,recovered}} \Delta H \big|_{\text{CoO at } T_{\text{recovered}} \rightarrow T_{\text{reactor}}} \tag{3.14}$$

$$\dot{Q}_{\text{solar}} = \frac{\dot{Q}_{\text{reactor}}}{\eta_{\text{abs}}} \tag{3.15}$$

$$\dot{Q}_{\text{loss}} = (1-\eta_{\text{abs}})\dot{Q}_{\text{solar}} \tag{3.16}$$

The rate of exergy destruction in the solar thermochemical reactor to the surroundings is given as:

$$\dot{\Xi}_{\text{D,reactor}} = \left(1-\frac{T_0}{T_{\text{reactor}}}\right)\dot{Q}_{\text{solar}} - \left(1-\frac{T_0}{T_0}\right)\dot{Q}_{\text{loss}} + \dot{n}_{\text{Co}_3\text{O}_4,\text{recovered}} \Delta\Xi_{\text{f}} \big|_{\text{Co}_3\text{O}_4 \text{ at } T_{\text{recovered}} \rightarrow 3\text{CoO}+\frac{1}{2}\text{O}_2 \text{ at } T_{\text{reactor}}, p_{\text{reactor}}} + \dot{n}_{\text{CoO,recovered}} \Delta\Xi_{\text{f}} \big|_{\text{CoO at } T_{\text{recovered}} \rightarrow T_{\text{reactor}}} \tag{3.17}$$

Exergy destruction due to the solar input was calculated using T_{reactor} according to previous literature [144, 145]. An ideal cooling process to T_0 was assumed for the O_2 stream exiting the solar thermochemical reactor. The heat rejected to the surroundings during the cooling process and the associated exergy destruction rate are given, respectively, as:

$$\dot{Q}_{\text{cool}} = \dot{n}_{\text{O}_2,\text{vac}} \Delta H \,|_{\frac{1}{2}\text{O}_2 \text{ at } T_{\text{reactor}} \to T_0} \tag{3.18}$$

$$\dot{\Xi}_{\text{D,cool}} = \left(1 - \frac{T_0}{T_{\text{b,cool}}}\right) \dot{Q}_{\text{cool}} \tag{3.19}$$

where $T_{\text{b,cool}}$ is the effective temperature at the boundary of the cooling process, given as:

$$T_{\text{b,cool}} = \frac{\dot{Q}_{\text{cool}}}{\dot{n}_{\text{O}_2,\text{vac}} \Delta S\Big|_{\frac{1}{2}\text{O}_2 \text{ at } T_{\text{reactor}} \to T_0}} \tag{3.20}$$

A reversible vacuum pump was assumed to operate isothermally at T_0 to reduce the pressure in the solar thermochemical reactor. The rates of work and heat transfer to the environment are given, respectively, as:

$$\dot{W}_{\text{vac}} = -\dot{n}_{\text{O}_2,\text{vac}} T_0 \, \Delta S\big|_{\text{O}_2 \text{ at } T_0, p_{\text{reactor}} \to p_0} \tag{3.21}$$

$$\dot{Q}_{\text{vac}} = \dot{W}_{\text{vac}} \tag{3.22}$$

To assess the potential of the CSP facility, the overall cycle efficiency is given as:

$$\eta_{\text{cycle}} = \frac{\dot{W}_{\text{turbine}} - \dot{W}_{\text{comp}} - \dot{W}_{\text{vac}}}{\dot{Q}_{\text{solar}}} \tag{3.23}$$

3.3 Results and discussion

Parameters for the thermodynamic and exergy analyses are provided in Table 3.1.

Table 3.1. Properties and values for the thermodynamic analysis of the Air Brayton cycle integrated with thermochemical heat storage.

Property	Value(s)
I	1 kW·m^{-2}
C	1000 suns
T_{solar}	5780 K
T_0	298.15 K
p_0	1 bar
$T_{reactor}$	1050-1250 K
$p_{reactor}$	0.001bar
p_{comp}	5 – 30 bar
A_r	5
$\dot{n}_{CoO,reactor}$	3 mol/s
$\dot{n}_{air}$	8 – 16 mol/s
α_1	0 (0-4 μm) and 0.9 (4 μm-∞)
ρ_1	0.06 (0-4 μm) and 0.1(4 μm-∞)
τ_1	0.94 (0-4 μm) and (4 μm-∞)
ε_1	0.9
ε_2, α_2	0.8
ρ_2	0.2

$T_{recover}$ and $T_{turbine}$ as functions of $\dot{n}_{air}$ were determined using the energy balance across the re-oxidizer employing the thermodynamic constraints previously described and are given in 31 at $T_{reactor}$ = 1050 K and p_{comp} = 30 bar. At $\dot{n}_{air}$ < 13.7 mol/s, $T_{turbine} \sim T_{turbine,max}$ and is greater than $T_{reactor}$ as calculated from the thermodynamic limit where $\Delta G = 0$. $T_{turbine}$ increases slightly with $\dot{n}_{air}$ as O_2 concentration increases at the airflow exit, favoring higher equilibrium temperatures and reaches a maximum of 1344.7 K at $\dot{n}_{air}$ = 13.7 mol/s. $T_{recover}$ decreases rapidly with $\dot{n}_{air}$, as more heat exits at the turbine to maintain $T_{turbine} = T_{turbine,max}$. $T_{recover}$ achieves a minimum possible temperature at $\dot{n}_{air}$ = 13.7 mol/s where $T_{recover} = T_{comp}$, corresponding to rapid decreases in $T_{turbine}$ for increasing $\dot{n}_{air}$ > 13.7 mol/s as greater airflows absorb greater sensible heat.

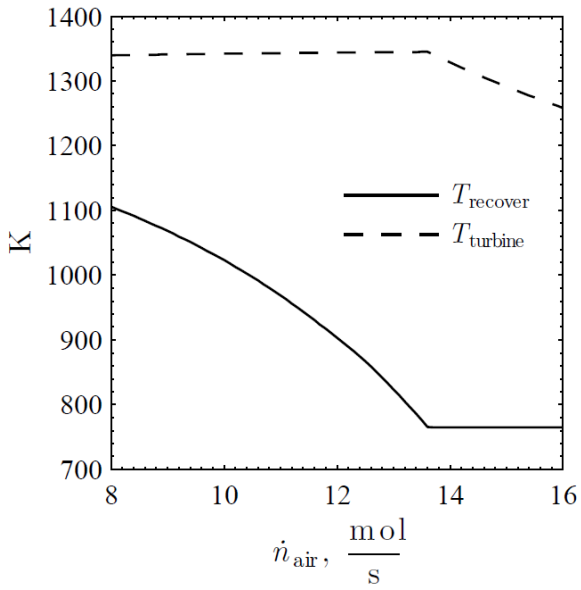

Figure 3.4. Particle temperature exiting re-oxidizer to the cold storage bin (solid) and air temperature entering turbine from the re-oxidizer (dashed) as functions of molar flow of air exiting the compressor at 30 bar for a solar thermochemical reactor temperature of 1050 K

$\dot{\Xi}_{\text{D,re-oxidizer}}$ and X are given as functions of $\dot{n}_{\text{air}}$ in Figure 3.5 at T_{reactor} = 1050 K and p_{comp} = 30 bar. The $\dot{\Xi}_{\text{D,re-oxidizer}}$ initially increases until it reaches a maximum of 11.8 kW at $\dot{n}_{\text{air}}$ = 9.8 mol/s, which corresponds the largest $\Delta\Xi_f$ between the particle and air streams. X increases as lower particle recovery temperatures favor complete conversion from CoO to Co_3O_4. Once T_{recover}=T_{comp}, $X \rightarrow 1$, which corresponds to a minimum $\dot{\Xi}_{\text{D,re-oxidizer}}$ at $\dot{n}_{\text{air}}$ = 13.7 mol/s and the smallest $\Delta\Xi_f$ between the particle and air streams. The $\dot{\Xi}_{\text{D,re-oxidizer}}$ then begins a monotonic increase with larger $\dot{n}_{\text{air}}$ due to the introduction of additional irreversibilities related to a decreasing T_{turbine}.

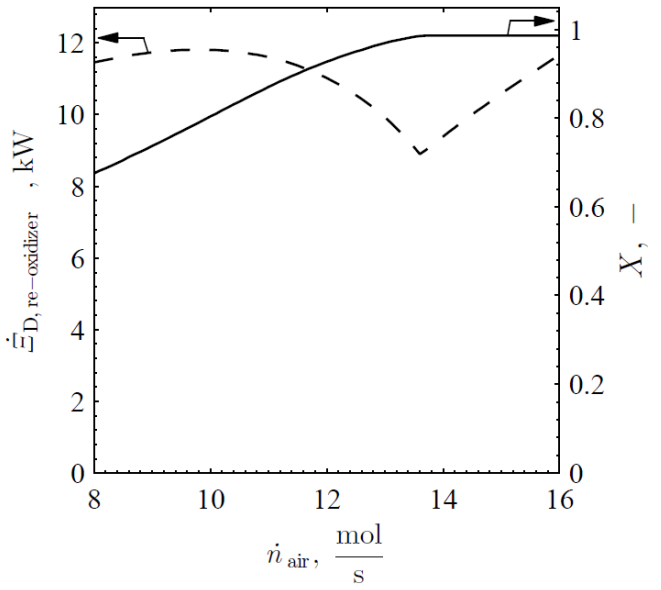

Figure 3.5. Exergy destruction rate (dashed) and conversion of CoO to Co3O4 (solid) across the re-oxidizer as functions of molar flow of air exiting the compressor at 30 bar and solar thermochemical reactor temperature of 1050 K

A comparison of η_{abs} as a function of A_r is given in Figure 3.6. The η_{abs} as a function of A_r is given in Figure 3.6a at $T_{reactor}$ = 1050 K for a range of ε_2. The η_{abs} rapidly increases with an increasing $A_r \leq 3$ for $\varepsilon_2 \leq 0.8$, after which the curves begin to asymptotically approach η_{abs} for $\varepsilon_2 = 1$ (i.e., a blackbody cavity). At higher A_r, a large portion of the incoming solar irradiation is absorbed due to an increase in internal reflections and subsequent absorptions, resulting in near blackbody behavior. Blackbody behavior is also more closely approximated as ε_2 approaches 1 for all A_r. The maximum η_{abs} never reaches the $\eta_{abs,ideal}$ as the quartz window reflects a portion of incoming solar radiation, subsequently reducing $H_{0,2}$ incident upon the cavity walls. The η_{abs} as a function of A_r for a range of $T_{reactor}$ at $\varepsilon_2 = 0.8$ is provided in Figure 3.6b. The η_{abs} at all $T_{reactor}$ increases initially and then begins to asymptotically approach the limit for a blackbody cavity. As $T_{reactor}$ increases, η_{abs} decreases as result of increased internal cavity re-radiation, increasing both emissions and convective losses due to a higher T_1 which increases from 820 K to

1010 K. Active cooling is often required for solar thermochemical reactors to ensure window durability [15, 76, 146], adding a small parasitic load not included in this analysis. A higher $T_{reactor}$ results in a more efficient power cycle by increasing the Carnot efficiency of the cycle, but the efficiency is offset by increased re-radiative losses to the environment. A $T_{reactor}$ =1106 K is the optimal operating temperature for C = 1000 suns and I = 1 kW/m^2 as calculated from the expression presented in [147] which depends upon the lower operating temperature of a Carnot heat engine equivalent to reactor operating conditions, effective cavity absorptance and emittance, and concentrated solar irradiation.

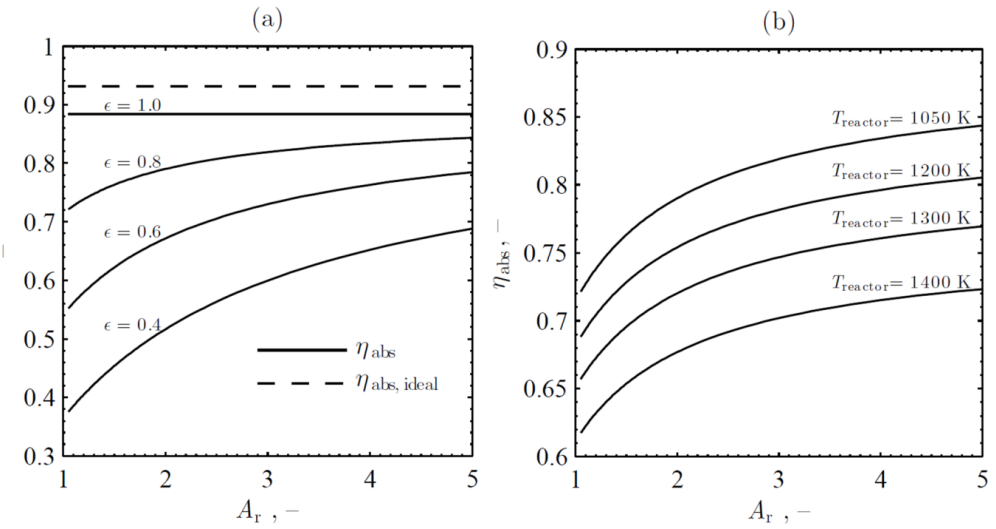

Figure 3.6. Absorption efficiency versus area ratio between the cavity and the quartz window for a solar thermochemical reactor for (a) a range of cavity emittances (solid) compared to a theoretical blackbody cavity (dashed) at a cavity temperature equal to 1050 K; and (b) a range of cavity temperatures for the cavity emittance equal to 0.8

$\dot{Q}_{solar}$, $\dot{Q}_{loss}$, and $\dot{Q}_{quench}$ as functions of $\dot{n}_{air}$ are given in Figure 3.7 at $T_{reactor}$ = 1050 K and p_{comp} = 30 bar. $\dot{Q}_{solar}$ rapidly increases with $\dot{n}_{air}$ as additional process heat is required to both sensibly heat and fully reduce incoming CoO/Co_3O_4 particles. The recovered particles decrease in temperature and increase in concentration of Co_3O_4 with increasing $\dot{n}_{air}$, as more heat is transferred to the air stream. When $\dot{n}_{air}$ <13.7 mol/s, $\dot{Q}_{solar}$ and $\dot{Q}_{loss}$

increase with $\dot{n}_{air}$ as $T_{recover}$ decreases and X increases, requiring more heat to drive the Co_3O_4 thermal reduction. $\dot{Q}_{quench}$ increases with $\dot{n}_{air}$ as higher X results in more O_2 evolution in the solar thermochemical reactor. Maximum values of $\dot{Q}_{solar}$ = 306 kW and $\dot{Q}_{loss}$ = 48 kW correspond to $\dot{n}_{air}$ =13.7 mol/s, after which $T_{recover}$ = T_{comp} and X remain constant, resulting in constant $\dot{Q}_{solar}$ and $\dot{Q}_{loss}$ (i.e., the solar thermochemical reactor requires no additional heat). At $\dot{n}_{air}$ > 13.7 mol/s, the equilibrium compositions of the incoming particles remain constant, resulting in a constant $\dot{Q}_{quench}$ as no additional O_2 is extracted by the vacuum pump from the solar thermochemical reactor.

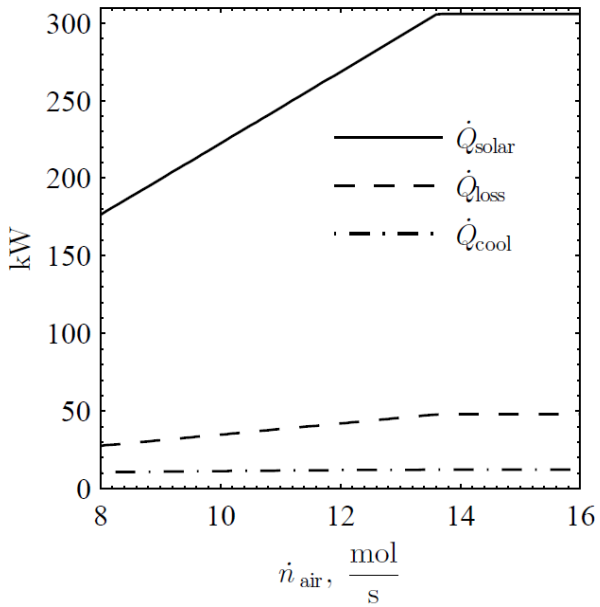

Figure 3.7. Concentrated solar power input (solid) and heat loss rate to the surrounding (dashed) for the solar thermochemical reactor and the rate of heat rejected to the surroundings from O_2 cooling (dash-dot) as functions of the molar flow of air exiting the compressor at 30 bar and a thermochemical reactor temperature of 1050 K

$\dot{W}_{turbine}$, $\dot{W}_{comp}$, and $\dot{W}_{vac}$ are given as functions of $\dot{n}_{air}$ in Figure 3.8 at $T_{reactor}$ = 1050 K and p_{comp} = 30 bar. $\dot{W}_{turbine}$ monotonically increases with $\dot{n}_{air}$ until reaching $\dot{n}_{air}$ = 13.7

mol/s. At $\dot{n}_{air}$ = 13.7 mol/s, increases in airflow entering the turbine are offset by lower $T_{turbine}$, resulting in a continued, shallower increase in $\dot{W}_{turbine}$. $\dot{W}_{comp}$ increases steadily as $\dot{n}_{air}$ increases constantly and the temperature difference across the turbine remains the same. $\dot{W}_{vac}$ increases as a result of greater O_2 production in the reactor until $\dot{n}_{air}$ = 13.7 mol/s and $\dot{W}_{vac}$ = 8.5 kW at which the composition of the entering particle stream and the O_2 produced are constant. The $\dot{W}_{vac}$ is a minor parasitic load compared to $\dot{W}_{comp}$ and $\dot{W}_{turbine}$.

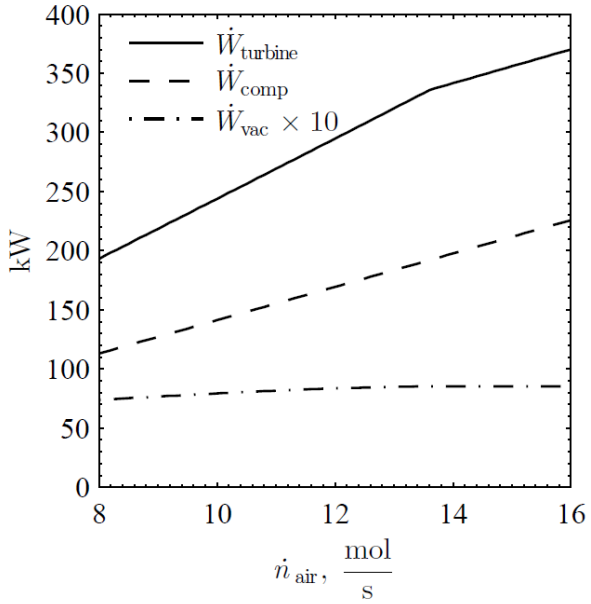

Figure 3.8. Rates of work for the turbine (solid), compressor (dashed), and vacuum pump (dash-dot) as functions of molar flow of air exiting the compressor at 30 bar and a thermochemical reactor temperature of 1050 K

$\dot{\Xi}_{D,reactor}$ and $\dot{\Xi}_{D,quench}$ are compared to X as functions of $\dot{n}_{air}$ and given in Figure 3.9 at $T_{reactor}$ = 1050 K and p_{comp} = 30 bar. The increase in X with $\dot{n}_{air}$ requires additional $\dot{Q}_{solar}$ to sensibly heat and fully-reduce the CoO/Co_3O_4 particle stream and overcome heat losses. Additional $\dot{Q}_{solar}$ greatly increases the incoming thermal exergy related to heat transfer across a boundary. However, once $\dot{Q}_{solar}$ and $T_{recover}$ are constant for $\dot{n}_{air} \geq 13.7$ mol/s, both

entering and exiting exergy flows become fixed and $\dot{\Xi}_{D,reactor}$ = 37.5 kW. Small $\dot{\Xi}_{D,quench}$ increases are correlated to increasing O_2 flowrates exiting the solar thermochemical reactor and the $\dot{\Xi}_{D,quench}$ plateaus at a maximum at 6.2 kW once *X* is constant.

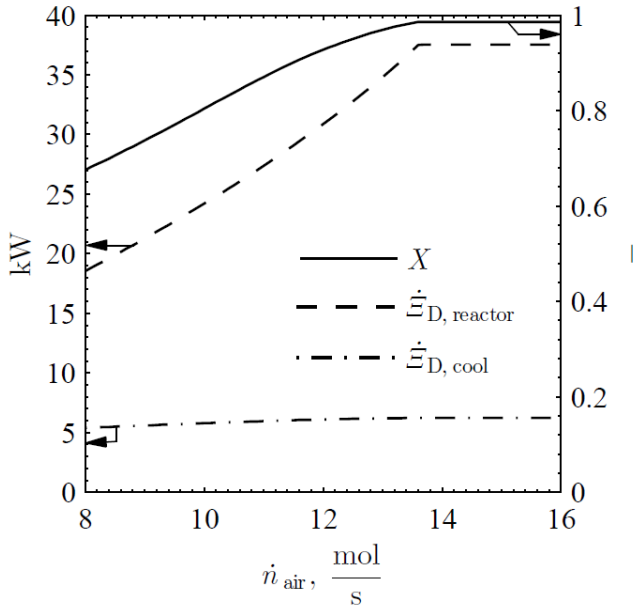

Figure 3.9. Exergy destruction rates in the solar thermochemical reactor (dashed) and from heat rejection during O_2 cooling (dash-dot) and conversion of CoO to Co3O4 in the re-oxidizer (solid) as functions of molar flow of air exiting the compressor at 30 bar and a thermochemical reactor temperature of 1050 K

Comparisons of η_{cycle} as a function of $\dot{n}_{air}$ are given in Figure 3.10 for a range of $T_{reactor}$ and p_{comp}. For all of the analyses, η_{cycle} increases with larger $\dot{n}_{air}$ for different $T_{reactor}$ and p_{comp}. η_{cycle} as a function of $\dot{n}_{air}$ is given in Figure 10a at $T_{reactor}$ = 1050 K for a range of p_{comp} between 5-30 bar, a pressure range suitable for gas turbines. Increasing to p_{comp} = 30 bar results in η_{cycle} nearing 44% compared with η_{cycle} of 26% for a p_{comp} = 5 bar. The increased η_{cycle} is a result of higher $T_{turbine}$ (Figure 1) and lower $T_{exhaust}$, directly translating to more $\dot{W}_{turbine}$. Increases in $\dot{W}_{turbine}$ more than offset the additional $\dot{W}_{comp}$ required. Operation at lower $\dot{n}_{air}$ resulted in some unreacted CoO, reducing $\dot{Q}_{solar}$ while decreasing

the energy density of the redox material. In addition, $T_{recover,min}$ increases at higher p_{comp}, decreasing the required amount of $\dot{Q}_{solar}$. Increasing $T_{reactor}$ results in decreases in η_{cycle} as $T_{turbine}$ is thermodynamically limited by 3CoO +½ O_2 reaction and remains relatively constant as shown in Figure 10b. Increases in $T_{reactor}$ at p_{comp} = 30 bar result in larger $\dot{Q}_{solar}$ due to larger $\dot{Q}_{loss}$ that do not correspond to increases in $\dot{W}_{turbine}$. An additional analysis was performed assuming no reactions (i.e., SES) with 1 mol/s of Co_3O_4 flowing through the system. η_{cycle} was 51% for operation at $T_{reactor}$ = 1050 K, p_{comp} = 30 bar, and $\dot{n}_{air}$ = 16 mol/s compared to η_{cycle} = 44% under the same conditions with reactions. However, the improved efficiency of SES comes at the expense of lower energy densities, requiring more materials handling and larger infrastructure (e.g., storage bins) throughout the system to achieve the same amount of $\dot{W}_{turbine}$.

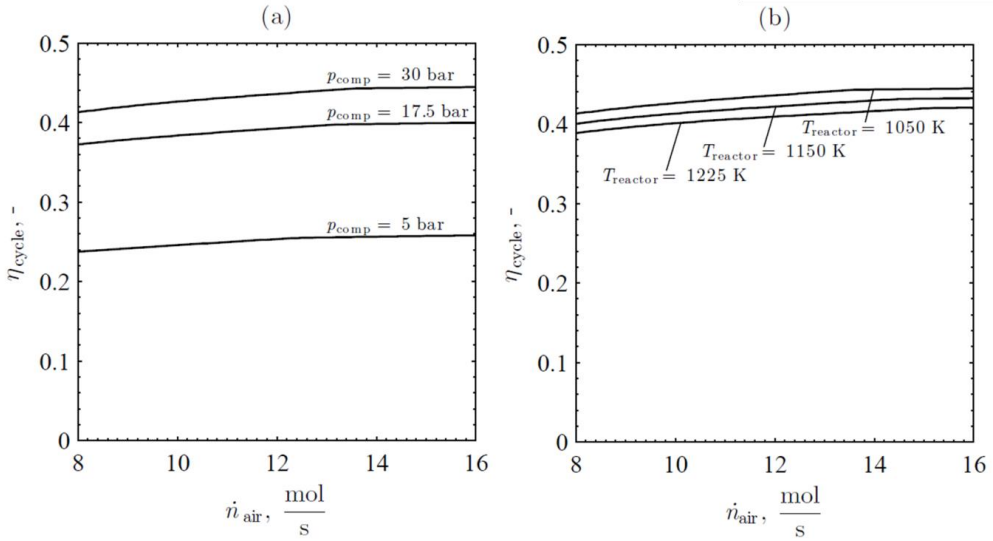

Figure 3.10. Overall cycle efficiency as a function of molar flow of air exiting the compressor for (a) a range of pressures exiting the compressor between 5-30 bar for solar thermochemical reactor temperature of 1050 K; and (b) a range of solar thermochemical reactor temperatures between 1050-1225 K for a pressure exiting the compressor of 30 bar

3.4 Verification

Thermodynamic analysis can be verified by performing an energy balance with a defined control volume that encompasses all components. This was done to compute the incoming concentrated solar irradiation, given as:

$$\begin{aligned}\dot{Q}_{\text{solar,ver}} &= \dot{Q}_{\text{loss}} + \dot{Q}_{\text{quench}} + \dot{Q}_{\text{pump}} + \dot{W}_{\text{turbine}} - \dot{W}_{\text{vac}} - \dot{W}_{\text{comp}} + \\ &\dot{n}_{\text{O}_2,\text{vac}} H\,|_{\text{O}_2 \text{ at } \text{T}_\text{o}} + \left(\dot{n}_{\text{air}} - \frac{1}{2}\dot{n}_{\text{Co}_3\text{O}_4,\text{recover}} \right) H\big|_{y_{\text{O}_2,\text{turbine}}\text{O}_2, y_{\text{N}_2,\text{turbine}}\text{N}_2 \text{ at } T_{\text{exhaust}}} - \\ &\dot{n}_{\text{air}} H\,|_{y_{\text{O}_2,0}\text{O}_2, y_{\text{N}_2,0}\text{N}_2 \text{ at } T_0}\end{aligned} \tag{3.24}$$

For operation at T_{reactor} = 1050 K, p_{comp} = 30 bar, and $\dot{n}_{\text{air}}$ = 16 mol/s both $\dot{Q}_{\text{solar}}$ and $\dot{Q}_{\text{solar,ver}}$ are equal to 306kW.

The available work, the sum of all of the work flows, exergy destructions, and the exergy flow at the exit of the turbine, can be used to determine the maximum cycle efficiency. This efficiency is comparable to a Carnot cycle operating between hot and cold temperature reservoirs of $T_{\text{H}} = T_{\text{reactor}}$ and $T_{\text{C}} = T_0$, respectively. The maximum efficiency is given as:

$$\begin{aligned}\eta_{\max} &= \frac{\dot{W}_{\text{turbine}} - \dot{W}_{\text{comp}} - \dot{W}_{\text{vac}}}{\dot{Q}_{\text{solar}}} + \\ &\frac{\dot{\Xi}_{\text{d,reoxidizer}} + \dot{\Xi}_{\text{d,reactor}} + \left(\dot{n}_{\text{air}} - \frac{1}{2}\dot{n}_{\text{Co}_3\text{O}_4,\text{recover}} \right) \Xi_{\text{f}}\,|_{y_{\text{O}_2,\text{turbine}}\text{O}_2, y_{\text{N}_2,\text{turbine}}\text{N}_2 \text{ at } p_0, T_{\text{exhaust}}}}{\dot{Q}_{\text{solar}}} \\ &= 1 - \frac{T_0}{T_{\text{reactor}}} = \eta_{\text{Carnot}}\end{aligned} \tag{3.25}$$

For operation at T_{reactor} = 1050 K, p_{comp} = 30 bar, and $\dot{n}_{\text{air}}$ = 16 mol/s both $\eta_{\max}$ and η_{Carnot} are equal to 0.716.

A control volume excluding the solar thermochemical reactor, storage bins, and vacuum pump was used to compute the Air Brayton cycle efficiency, represented as:

$$\eta_{\text{Brayton}} = \frac{\dot{W}_{\text{turbine}} - \dot{W}_{\text{comp}}}{\dot{n}_{\text{air}} \Delta H\big|_{y_{O_2} O_2, y_{N_2} N_2 \text{ at } T_{\text{comp}} \rightarrow T_{\text{turbine}}}} \tag{3.26}$$

Some O_2 was consumed during re-oxidation between the compressor and turbine. This was compared to the cycle efficiency of an ideal Air-Standard Brayton cycle, represented as:

$$\eta_{\text{Brayton,ideal}} = 1 - \frac{1}{r_p^{(k-1)/k}} \tag{3.27}$$

where k is the specific heat ratio for air. For operation at T_{reactor} = 1050 K, p_{comp} = 30 bar, $\dot{n}_{\text{air}}$ = 16 mol/s, η_{Brayton} is 55 % while $\eta_{\text{Brayton,ideal}}$ is 62 %. Exergy destruction within the re-oxidizer due to the chemical reaction impacts the performance of the Air Brayton cycle.

3.5 Summary and conclusions

A thermodynamic analysis was performed for an Air- Brayton cycle coupled to a two-step thermochemical cycle for heat storage based on CoO/Co_3O_4 redox reactions through direct integration of direct counter-flow heat exchange between the high-temperature particles and the working fluid. Cycle performance was quantified and major sources of irreversibilities (i.e., exergy destruction) were identified using exergy destruction results. The analysis used a windowed cavity receiver for a solar thermochemical reactor to directly heat CoO/Co_3O_4 particles with concentrated solar irradiation. For a solar thermochemical reactor temperature of 1050 K and an outlet compressor pressure of 30 bar, the maximum cycle efficiency approached 44%. The cycle

efficiency decreased to 26% for outlet compressor pressures of 5 bar. Operation at higher solar thermochemical reactor temperatures resulted in decreased cycle efficiencies, while increased airflow rates across the compressor increased cycle efficiencies for the range of solar thermochemical reactor temperature and outlet compressor pressures considered. The dominant source of exergy destruction was in the solar thermochemical reactor, due to the incoming concentrated solar irradiation used to heat entering particles and chemically reduce Co_3O_4 to CoO and O_2. Smaller exergy destruction rates were determined for the re-oxidizer and the cooling process. The analysis shows the potential of directly integrating a two-step solar thermochemical cycle into an Air Brayton cycle as the cycle is capable of effectively utilizing the available exergy while incorporating heat storage, culminating in high operating efficiencies. Additionally, the analysis has demonstrated the importance of designing a solar thermochemical reactor for the effective and efficient storage of solar energy within metal oxide particles.

CHAPTER 4. COBALT OXIDE REDUCTION KINETICS[1]

4.1 Introduction

Accurate determination of the chemical reduction kinetics is of key importance for developing solar thermochemical reactor technologies to realize effective and efficient storage of concentrated solar power. In the present work, apparent chemical kinetic parameters for Co_3O_4 thermal reduction are determined with thermogravimetry at 1 bar over a range of temperatures and O_2 concentrations. The novelty of this work is aimed towards developing applicable kinetics for Co_3O_4 thermal reduction that capture the effects of both temperature and O_2 partial pressure over appropriate ranges for concentrated solar power applications.

4.2 Experimental Section

Experimentation was carried out using a TGA (Netzsch STA449 F3 Jupiter, ± 1 μg). Powder samples of ~100 mg of Co_3O_4 (Sigma-Aldrich, particle size <10 μm) and CoO (Sigma-Aldrich, ~325 mesh) were placed on a 17-mm-diameter Al_2O_3 crucible. The crucible was in contact with an S-type thermocouple and was covered with a platinum foil to prevent unwanted reactions. The initial mass of each sample was determined using an analytical balance (Mettler-Toledo ML54, ± 0.1 mg), and product gases were temporally monitored with mass spectrometry (MS, OmniStar ThermoStar GSD320 Gas Analysis

[1] TGA experimental procedures, data-processing techniques, and additional oxidation kinetics and reduction / oxidation cyclability evaluations were developed by Dr. Alexander Muroyama, with whom kinetic evaluation was performed in collaboration in: Muroyama, A.P., A.J. Schrader, and P.G. Loutzenhiser, *Solar electricity via an Air Brayton cycle with an integrated two-step thermochemical cycle for heat storage based on Co3O4/CoO redox reactions II: Kinetic analyses.* Sol. Energy, 2015. 122: p. 409-418

System) and gas chromatography (GC, Agilent 490 Micro GC equipped with Molsieve and PoraPLOT Q columns). Different initial powder samples for CoO and Co_3O_4 were used due to uncertainty concerning full conversion. Using different samples ensured sample purity and uniformity between experiments.

Isothermal experiments were performed to examine the Co_3O_4 thermal reduction in the high temperature graphite furnace (T_{max} = 2273K) of the TGA at different temperatures and O_2 concentrations. The samples were heated at 20 K/min in the graphite furnace with 100 mL_N/min (L_N denotes liters at normal conditions at 273 K and 1 bar) of 80% O_2-Ar entering from the bottom of the graphite furnace to impede the onset of Co_3O_4 thermal reduction. Upon reaching the isotherm, the samples were held in 80% O_2-Ar for ~15 min to allow for thermal stabilization, and the atmosphere was then switched to a reducing atmosphere of O_2-Ar to allow the thermal reduction to proceed until conversion from Co_3O_4 to CoO was complete. MS and GC measurements showed that ~1.5 min was required to purge to O_2 below 1% from the graphite furnace. Three runs were performed for each condition, and blanks were run at each condition and subtracted from sample runs to mitigate the effects of buoyancy and momentum due to changing temperatures. The $\%\Delta m_{loss}(t)/m_{initial}$ for isothermal experiments between 1113 – 1213 K in 0% O_2-Ar are shown in Figure 4.1a. Mass loss curves have deceleratory rate that is highly temperature-dependent. All samples reached complete conversion with a $\%\Delta m_{loss}(t)/m_{initial}$ equal to 6.6%. There was almost an order of magnitude difference between time to complete conversion at the minimum and maximum temperatures tested, and increasing the temperature above 1193 K led to only marginal increases in reaction rate. The rate slowed as the samples reached full conversion. Figure 4.1b shows the $\%\Delta m_{loss}(t)/m_{initial}$ for

isothermal experiments at 1213 K in 0-20% O_2-Ar. Mass loss was slightly less consistent as sample conditions approached the thermodynamic limit, but a clear trend of higher O_2 concentrations inhibiting the rate of thermal reduction was seen. Approximately twice the time was required to reduce the Co_3O_4 particles under a 20% O_2-Ar atmosphere versus a 0% O_2-Ar atmosphere. Samples at 1213 K did not completely reduce above 20% O_2-Ar, so temperature changes had a demonstrably greater effect on rate than O_2 concentration changes.

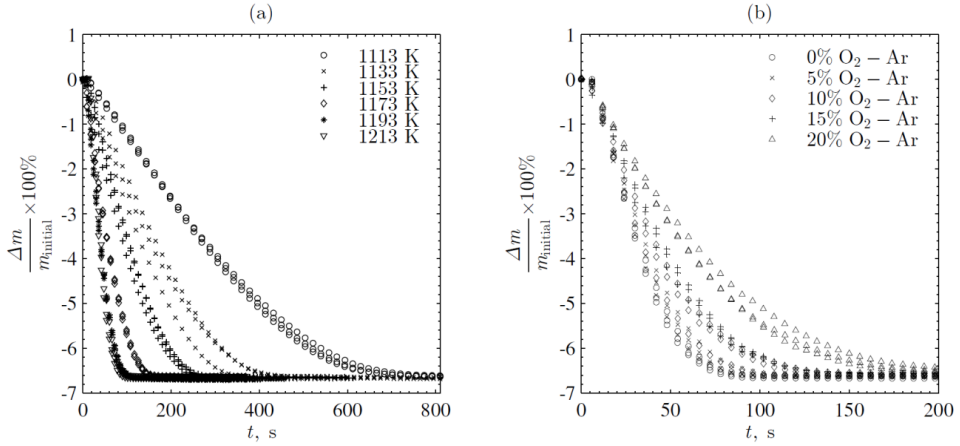

Figure 4.1. Measured temporal mass losses normalized with the initial mass from isothermal thermogravimetry for the Co_3O_4 thermal reduction for (a) temperatures between 1113 – 1213 K at 0% O_2-Ar and (b) O_2 concentrations between 0-20% O_2-Ar at 1213 K

Non-isothermal thermal reduction experiments were performed by heating Co_3O_4 samples at a rate of 20 K/min in a reducing atmosphere flowing at 100 mL_N/min until complete conversion was achieved. Three runs were performed at each O_2-Ar condition and blank runs were subtracted from sample runs. Figure 4.2 shows the $\%\Delta m_{loss}(t)/m_{initial}$ for experiments in 0-15% O_2-Ar. Higher O_2 concentrations prevented the onset of the thermal reduction as the reaction was thermodynamically limited. While higher O_2 concentrations would inhibit rate of thermal reduction due to the back reaction, this was

offset by higher corresponding thermal reduction temperatures in non-isothermal experiments, leading to minimal changes in rate between 5-15% O_2-Ar.

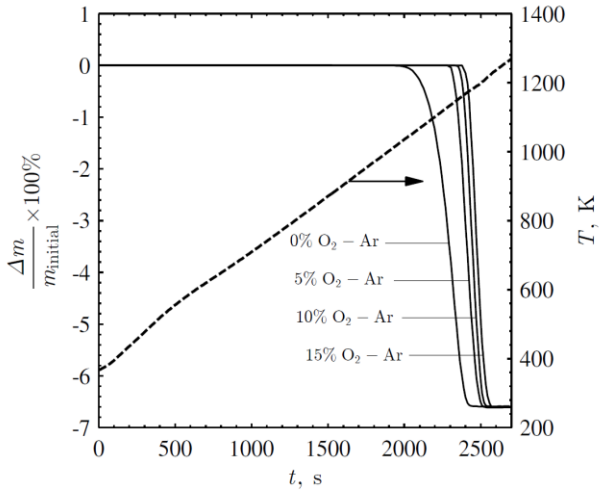

Figure 4.2. Measured temporal mass losses normalized with the initial mass for non-isothermal thermogravimetry for O_2 concentrations between 0-15% O_2-Ar with the temporal temperature (dashed) increasing at a rate of 20 K/min

4.3 Kinetic Analysis

The temporal conversion of Co_3O_4 to CoO was determined using TGA measurements as:

$$\alpha(t) = \frac{m(t) - m_{\text{initial}}}{m_{\infty} - m_{\text{initial}}} \tag{4.1}$$

where t is time; $m(t)$ is temporal sample mass measured by TGA; m_{initial} is the initial sample mass; and m_{∞} is the mass calculated for full conversion. Weighted non-linear regression [148] was used to fit data to the appropriate rate laws using the least squares criterion for best fit by minimizing chi-squared using a multidimensional unconstrained non-linear minimization algorithm (Nelder-Mead), represented generically as:

$$\chi^2_{\min} = \sum_{\mathrm{j}} \left(\frac{F_{\mathrm{j}}}{\sigma_{\mathrm{j}}} \right)^2 \tag{4.2}$$

where F is a function of measured properties and values that are initially unknown, represented as:

$$F_{\mathrm{j}} = f\left(q_{1\mathrm{j}}, ..., q_{\mathrm{nj}}; \beta_1, ..., \beta_r\right) = 0 \tag{4.3}$$

where q denotes n measurands assumed as known, and β represents r fitting parameters assumed initially as unknown. The standard error was estimated as:

$$\sigma_{\mathrm{j}}^2 = \sum_{\mathrm{i=1}}^{\mathrm{n}} \left(\frac{\partial F_{\mathrm{j}}}{\partial q_{\mathrm{ij}}} \right)^2 \sigma_{\mathrm{ij}}^2 \tag{4.4}$$

where σ_{ij} represents the experimental uncertainty of the parameter. Ninety-five percent confidence limits for the β's were estimated using Monte Carlo analyses [148] with greater than 200 iterations by stochastically varying σ_{ij}'s according to a Gaussian probability distribution function (pdf) and a uniform pdf for frequentist and Bayesian errors, respectively [150].

The rate limiting mechanism for Co_3O_4 thermal reduction was related to random nucleation where imperfections in surface of the solid reactant material minimize the activation energy [151]. Nucleation has been proposed as the mechanism for several decomposition reactions [151]. A pressure dependence power rate law was included to account for the $3CoO + ½O_2 \rightarrow Co_3O_4$ back reaction (2), which impedes the forward reaction (1). The Avrami-Erofeyev model with a power rate term to resolve O_2 partial pressure functionality from literature [54, 152] for solid-gas reactions captured the reaction mechanism, given as:

$$k\left(1-\frac{p_{O_2}}{p_{O_2,eq}(T)}\right)^{\gamma}(t-t_0)=[-\ln(1-\alpha)]^{1/n} \quad (4.5)$$

where n is the Avrami constant; p_{O_2} is the O_2 partial pressure, $p_{O_2,eq}$ is the O_2 partial pressure at equilibrium determined using thermophysical property data [153]; γ is the reaction order; t_0 is the offset time required to resolve the latency from switching from 80% O_2-Ar to 0-20% O_2-Ar and small grain growth during the onset of nucleation. For isothermal experiments performed with 0% O_2-Ar, the back reaction is small (i.e., p_{O_2} =0) as the O_2 evolving during the reaction is continuously removed. The reaction mechanism is represented as:

$$k(t-t_0)=[-\ln(1-\alpha)]^{1/n} \quad (4.6)$$

The rate constants were assumed to follow an Arrhenius-type temperature dependency, represented as:

$$k=k_0\exp\left(-\frac{E_a}{RT}\right) \quad (4.7)$$

where k_0 is the pre-exponential factor; E_a is the apparent activation energy; R is the universal gas constant; and T is the temperature.

4.4 Results and Discussion

Kinetic analyses were performed for Co_3O_4 thermal reduction and the results are described in this section. Figure 4.3a shows a comparison of the modeled and experimental conversion for Co_3O_4 thermal reduction between 1113-1213 K at 0% O_2-Ar. n = 1.968 ± 0.058 was determined for Co_3O_4 thermal reduction with good agreement between the model and experiment as t_0 was used to account for the switching from 80% O_2-Ar to 0%

O_2-Ar. This deviation was less pronounced at higher temperatures due to favorable thermodynamics at higher O_2 concentrations. Figure 4.3b shows the modeled and experimental conversion for Co_3O_4 thermal reduction at 1213 K between 0-20% O_2-Ar. γ = 1.506 ± 0.022 was determined by fitting all data simultaneously and using k's and n's determined at 0% O_2-Ar between 1113-1213 K. The γ term captures the complex dependence of reaction rate on p_{O_2}. Agreement between the modeled and experimental conversions is particularly strong at lower O_2 concentrations where thermal reduction takes place relatively quickly, but deviates more as O_2 concentrations approach the thermodynamic limit of thermal reduction.

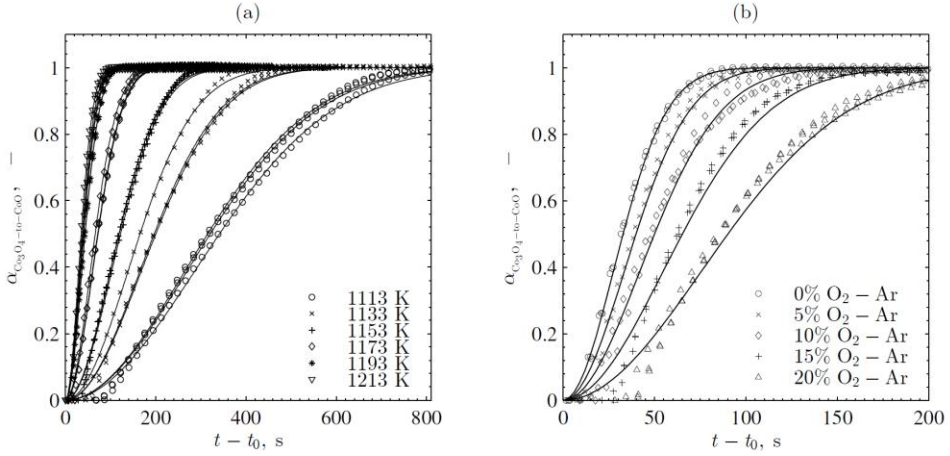

Figure 4.3. Experimental (markers) and fitted (solid) conversion for Co_3O_4 thermal reduction (a) for temperatures between 1113 – 1213 K at 0% O_2-Ar and (b) O_2 concentrations between 0-20% O_2-Ar at 1213 K

The rate constants were determined from isothermal experiments at 0% O_2-Ar and fitted to an Arrhenius-type temperature dependency, with k_0 and E_a, given with 95% confidence limits as:

$$k = 1.104 \pm 0.043 \times 10^{9}\,\mathrm{s}^{-1} \exp\left(-\frac{247.21 \pm 0.38\ \mathrm{kJ/mol}}{RT}\right) \tag{4.8}$$

The Arrhenius-type temperature dependency is shown in Figure 4.4 for Co_3O_4. The *k*'s are strongly dependent on temperature and exponentially increase with increasing temperature. The apparent activation energy is similar in magnitude to the enthalpy change of reaction, consistent with observations about metal oxide thermal reduction [154]. The value was lower than previously reported values [52-54]; however, the apparent activation energy can be highly dependent on experimental conditions, sample preparation, and chosen reaction mechanism.

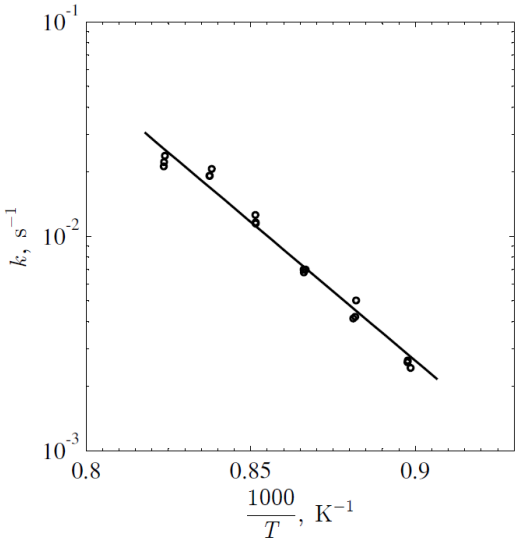

Figure 4.4. Arrhenius plot for isothermal Co_3O_4 thermal reduction showing experimental (markers) and fitted (solid) kinetic parameters

4.5 Conclusions

Co_3O_4 reduction reactions were analyzed using thermogravimetry for application in two-step solar thermochemical cycle integrated into an Air Brayton cycle to store heat. Apparent kinetic parameters were determined for Co_3O_4 thermal reduction with Arrhenius-type temperature dependencies. The thermal reduction followed a nucleation model with an Avrami constant equal to 1.968. O_2 partial pressure dependence of thermal reduction

was given by a reaction order of 1.506. The apparent activation energy for thermal reduction was 247.21 $kJ \cdot mol^{-1}$. Non-isothermal thermal reduction demonstrated the thermodynamic limit of spontaneous reaction due to the presence of O_2.

The reduction kinetics developed in this work serve to guide solar thermochemical reactor designs to efficiently realize Co_3O_4 thermal reduction operating within the temperatures ranges and O_2 partial pressures of the proposed two-step cycle.

CHAPTER 5. EVALUATION OF INCLINED REACTOR CONCEPT[2]

5.1 Introduction

The previous thermodynamic and kinetics analyses have demonstrated the promise of Co_3O_4/CoO as a solar thermochemical energy storage material [9, 36-38] and are used to inform a solar thermochemical reactor concept. Efficient thermal reduction of Co_3O_4 is an integral step in realizing high cycle efficiencies for the integrated system, necessitating solar thermochemical reactor technologies that effectively capture incoming concentrated irradiation while mitigating heat losses to the environment. Detailed modeling is presented in this work to evaluate a horizontally oriented inclined slope reactor concept for thermally reducing Co_3O_4 to CoO and O_2. Heat and mass transfer mechanisms were coupled to chemical kinetics, optics, and particle flow correlations along an inclined plane [129, 155]. A parametric study was performed with a response surface for design optimization [156] to evaluate reactor performance as characterized by outlet conversion from Co_3O_4 to CoO, particle outlet temperature, and maximum flow temperature, and for a range of model inputs, including cavity depth, particle inlet temperature, and solar concentration ratio at the aperture.

5.2 Solar thermochemical reactor design concept

Efficient thermal reduction of Co_3O_4 is integral in realizing high cycle efficiencies, which requires a solar thermochemical reactor designed for direct solar irradiation of the

[2] MCRT of the high-flux solar simulator was performed by Robert Gill.

reacting material, continuous on-sun operation, and matched incident concentrated solar power to the rate of sensible and chemical energy storage of the reacting material [16, 17, 74]. A 5 KW_{th} laboratory-scale thermochemical solar reactor, the Solar Thermochemical INclined Granular-flow Reactor (STInGR), was designed to fulfill these criteria. The STInGR is schematically depicted in Figure 5.1, mounted in the horizontal position. Concentrated irradiation is introduced through a quartz window into a cavity designed to mitigate radiative losses, and the concentrated irradiation impinges directly on an incline plane and the reactor walls. Concentrated irradiation is efficiently captured using a large area ratio between the cavity walls and aperture to promote blackbody behavior [8]. The cavity walls were simulated using optical and thermophysical properties of alumina. Co_3O_4 particles enter at the top of the inclined plane and move along the slope in a gravity-driven flow of reacting particles, exiting the bottom of the STInGR. The Co_3O_4 particles are rapidly heated and thermally reduced to produce CoO and O_2. The cavity is sealed with a quartz window and evacuated to maintain a low O_2 partial pressure. A velocity profile for granular flow along inclined slopes was developed using a combination of frictional and collisional effects between particle layers, resulting in increased residence times for particles nearest the inclined slope compared to particles nearest the free surface. The inclined slope was tuned to achieve sufficient mass transport to match sensible and chemical energy storage to incoming concentrated irradiation. Resultant particle residence times promoted complete conversion of Co_3O_4 to CoO.

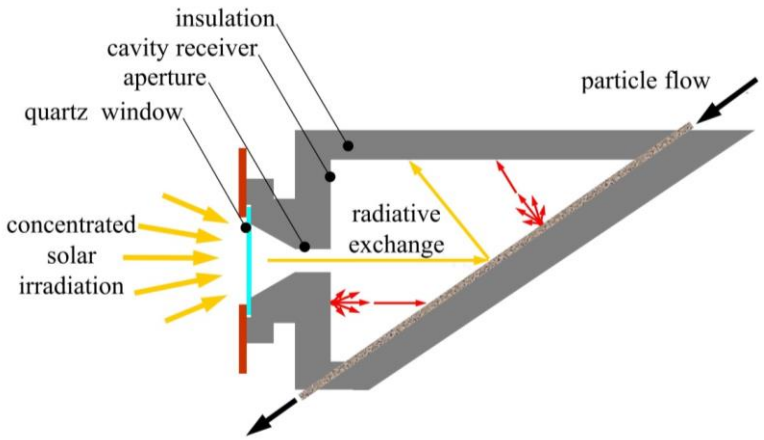

Figure 5.1 Proposed solar thermochemical inclined granular-flow reactor design for thermally reducing Co_3O_4 to CoO and O_2 by directly exposing the particles to concentrated irradiation

5.3 Modeling

Modeling efforts for the STInGR considered 1) the quartz window, 2) the surface-to-surface radiative heat exchange, 3) the particle bed flow, and 4) a coupled energy balance.

5.3.1 Quartz window

A window for the STInGR was designed with quartz glass due to its high optical transmittance, high thermal shock resistance, and high strength. The window was designed to operate under vacuum, capable of withstanding an external atmospheric pressure of up to approximately 100 kPa. Because quartz can withstand significantly greater compressive stresses than tensile stresses, the maximum tolerated tensile stress in the quartz window was estimated with the empirically determined probability of fused quartz test specimen failure [157], given as:

$$P_f = 1 - \exp\left[-(S / S_n)^m\right] \tag{5.1}$$

where m is the Weibull shape parameter; S is the maximum tolerated tensile stress for a particular P_f; and S_n is the characteristic tensile stress at which 63.2% of tested fused quartz specimens failed, estimated as:

$$S_n = \frac{S_{reference}}{\left(A_{reference} / A_{window} \right)^{\frac{1}{m}}} \tag{5.2}$$

where A_{window} is the projected stressed window area; $A_{reference}$ is a tabulated stressed area from previously tested fused quartz specimens; and $S_{reference}$ is the tabulated characteristic stress associated with $A_{reference}$ [158-160]. A Weibull shape parameter of $m \approx 10$ was used for stressed regions between 25.4 - 228.6 mm in diameter. A stress analysis on a window design subject to a distributed external 100 kPa pressure was performed with S representing a maximum tolerable tensile stress condition. Solidworks finite element analysis [161] was used to iteratively determine the required window thickness where tensile stress does not exceed S.

5.3.2 Surface-to-surface radiative exchange

Radiative heat transmitted through the window and radiative heat exchange between cavity surfaces was determined using a Monte Carlo ray tracing model. The modeled radiative input was supplied from a high flux solar simulator (HFSS) consisting of seven xenon arc lamps capable of delivering greater than 5 kW_{th} of concentrated irradiation to a 40 mm diameter area in the focal plane [162]. The quartz window was assumed isothermal and modeled at the reactor aperture to examine a stressed window heating scenario. A semi-gray, two-band approximation was used to account for spectral dependency of the quartz glass while a semi-gray three-band approximation was used to

account for spectral dependency of the alumina cavity surfaces. The total, hemispherical emissivity of the flow free surface included increased absorptive effects due to surface roughness [163]. Alumina cavity surfaces and the granular flow free surface were assumed as diffuse surfaces while the window was assumed as a specularly reflective surface. The Monte Carlo ray tracing method within the reactor cavity is illustrated in Figure 5.2.

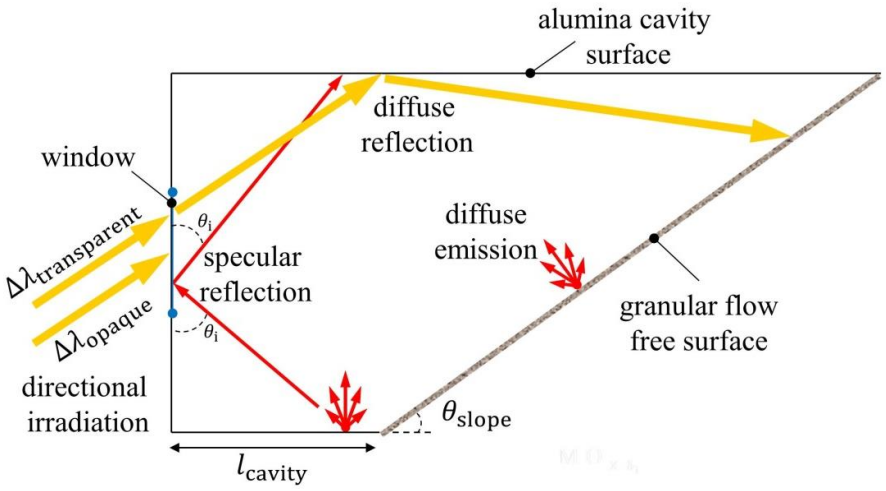

Figure 5.2. Monte Carlo ray trace analysis between diffusely reflective alumina cavity surfaces / granular flow free surface and specularly reflective, spectrally selective window for a directional radiative input supplied from a high flux solar simulator

Surface-to-surface exchange due to emissions and reflections within a k^{th} spectral band between surface *i* and surface *j* was represented using stochastically-determined band-averaged spectral radiation distribution factors [164]. Distribution factors were produced for each discretized reactor geometry with five million rays emitted per discretized surface and 70 million rays emitted from the HFSS. The net radiative heat flux for a single surface element is given as:

$$q_{i,\text{net}} = q_{i,\text{a}} - q_{i,\text{e}} + H_{ik,\text{a}} = \sum_{k=1}^{K}\sum_{j=1}^{N} \varepsilon_{ik} E_{\text{b}}\left(\Delta\lambda, T\right)\left(D_{ijk} - \delta_{ijk}\right) + H_{ik,\text{a}} \tag{5.3}$$

where $q_{i,a}$ is the absorbed surface exchange radiative heat flux on the surface; $H_{ik,a}$ is the absorbed radiative heat flux supplied by the high flux solar simulator on the surface; $q_{i,e}$ is the emitted heat flux from the surface; ε_{ik} is the spectral, hemispherical emissivity; $E_b(\Delta\lambda, T)$ is the spectral, hemispherical, fractional black body emissive power for a given wavelength band and surface temperature; D_{ijk} is the stochastically determined distribution factor; and δ_{ijk} is the Kronecker delta function.

5.3.3 Particle bed flow

The particle flow along inclined slopes was modeled as a uniform, gravity-driven, dense granular flow where the interstitial fluid has negligible effect on the flow behavior [118, 130, 165]. The average velocity for a dense granular flow along the inclined slope was determined empirically and was highly dependent upon the relative roughness between the granular material and the slope [129, 132], given as:

$$\bar{u} = \sqrt{gh}\left(\beta\frac{h}{h_{stop}} - \gamma\right) \tag{5.4}$$

where g is local acceleration due to gravity; h is the steady state granular flow depth; β and γ are empirically determined fitting parameters unique to the granular material; and h_{stop} is the maximum bed depth for a stationary, inclined bed. Co_3O_4/CoO particles and slope pairings were assumed to produce similar flow behavior. The h_{stop} was determined as:

$$\tan\theta_{slope} = \tan\theta_{min} + \left(\tan\theta_{max} - \tan\theta_{min}\right)\exp\left(-\frac{h_{stop}}{Ld_p}\right) \tag{5.5}$$

where L is an empirically determined fitted parameter describing the dimensionless flow depth; θ_{min} is an empirically determined inclination angle for which $h \rightarrow h_{stop}$; and θ_{max} is an empirically determined inclination angle for which $h_{stop} \rightarrow 0$. From this, the average residence time for the steady granular flow was estimated as:

$$\bar{t}_{res} = \frac{h_{cavity}}{\sin\left(\theta_{slope}\right)\bar{u}} \tag{5.6}$$

where h_{cavity} is the cavity height.

Thin, dense granular flows between 5-15 particle diameters thick resulted in nearly linear velocity profiles [166] with numerous models having been proposed [167, 168]. The dense, granular flow velocity profile captured frictional and collisional effects of the granular material within a stress tensor that included the sum of the Bagnold collisional stress, coulombic friction, and an additional stress term related to the observed formation and dissolution of tightly-packed particle chains within the flowing material [155]. The model was developed assuming negligible sidewall effects and steady, unidirectional, fully-developed flow, given as:

$$u = \left(\xi_x{}^3 \frac{f_v \rho_{ave} g}{B} \cos\theta_{slope} \left(\tan\theta_{slope} - \tan\varphi \right) \right)^{\frac{1}{2}} \int_{\left(H_{sf} d_p - z\right)/\xi_x}^{H_{sf} d_p/\xi_x} \left(1 - \exp(-z)\right)^{\frac{1}{2}} dz \tag{5.7}$$

where f_v is the particle volume fraction and has been observed as 0.6 for dense granular flows; ρ_{ave} is the average density for Co_3O_4/CoO particles; φ is the angle of internal friction, assumed as θ_{min}; H_{sf} is the ratio of h to d_p; ξ_x is the correlation length describing spacing between solid particle chains; and B is the Bagnold coefficient. B is approximated [168] using the mass flow rate of the steady granular flow assuming $\bar{u} \approx u_{z=H_{sf} d_p}/2$.

5.3.4 Coupling to the Energy Equation

` Radiative exchange and particle flow models were coupled to the energy equation for a directly-irradiated dense granular flow of Co_3O_4/CoO particles. The energy equation was developed assuming Co_3O_4/CoO particles and interstitial O_2 were transported as a single macroscopic continuum, a valid approximation when the dynamics of individual species are closely coupled [169] and local thermal equilibrium between fluid and solid phases can be assumed [170]. The O_2 evolved during the thermal reduction of Co_3O_4 was assumed to be instantaneously removed from the thin bed, thus maintaining a constant O_2 partial pressure. The steady-state energy equation for the reacting granular flow with negligible kinetic and potential energies was developed and captured the energy flow of the particles along the inclined slope and 3D conduction throughout the bed, given as:

$$u\frac{\partial\left(\sum n_i h_i\right)}{\partial x} = \left(k_{eff}\nabla T\right)\cdot\vec{A} \tag{5.8}$$

where n_i is moles of a given species determined as a function of spatial molar solid composition [171]; h_i is the molar enthalpy of a given species; $\vec{A}$ is the cross-sectional area normal to bed conduction; i is a species indice = CoO, Co_3O_4, and O_2; and k_{eff} is the effective thermal conductivity that accounts for thermal conductivity in the bed and radiative exchange between particles via the Rosseland diffusion approximation, given as:

$$k_{eff} = k_{bed} + k_{rad} = k_{bed} + \frac{32}{3\xi f_v Q_{ext}}\sigma d_p T^3 \tag{5.9}$$

where k_{bed} is the effective packed bed thermal conductivity from the Zehner and Bauer unit cell model [172, 173]; k_{rad} is the packed bed radiative conductivity as determined from the Rosseland diffusion approximation [174, 175]; ξ is an independent scattering

correction factor; σ is the Stefan-Boltzman constant; and Q_{ext}=2 is the medium extinction efficiency for particles exhibiting geometric optics characteristics [176]. The enthalpy flow term is represented as:

$$u\frac{\partial\left(\sum n_i h_i\right)}{\partial x} = u\sum n_i \frac{\partial h_i}{\partial x} + u\sum h_i \frac{\partial n_i}{\partial x} = u\sum n_i C_i \frac{\partial T}{\partial x} + u\sum h_i \frac{\partial n_i}{\partial x} \tag{5.10}$$

where C_i is the temperature-dependent, molar specific heat of a given species. The thermophysical properties were extracted from NIST Chemistry WebBook [177]. A species balance was used to resolve the change in molar density due to the chemical reaction, given as:

$$r_{Co_3O_4} = \frac{\partial n_{Co_3O_4}}{\partial t} = -u\frac{\partial n_{Co_3O_4}}{\partial x} = 3u\frac{\partial n_{CoO}}{\partial x} = \frac{1}{2}u\frac{\partial n_{O_2}}{\partial x} \tag{5.11}$$

where $r_{Co_3O_4}$ is the Co_3O_4 molar consumption rate as a function of pressure, temperature, and conversion determined from [178]. The energy equation was discretized normal to the flow, which resulted in an enthalpy change given as:

$$u\sum h_i \frac{\partial n_i}{\partial x} = r_{Co_3O_4}\left[h_{Co_3O_4\,\text{at}\,T_{x-dx/2}} - 3h_{CoO\,\text{at}\,T_{x+dx/2}} - \frac{1}{2}h_{O_2\,\text{at}\,T_{x+dx/2}}\right] \tag{5.12}$$

At the particle inlet to the cavity, a uniform temperature and flow composition, and unidirectional velocity profile were assumed. A directly irradiated flow top surface and one-dimensional, steady heat transfer through the bed sidewall and bottom surfaces were assumed, given, respectively, as:

$$q_{net,i} = -k_{eff}\left.\frac{\partial T}{\partial n}\right|_{top} \tag{5.13}$$

$$U\left[T_{\mathrm{f},i}-T_{\infty}\right]=-k_{\mathrm{eff}}\left.\frac{\partial T}{\partial n}\right|_{\text{sidewalls, bottom}} \tag{5.14}$$

where n is the direction normal to the bed; $T_{\mathrm{f,i}}$ is the boundary bed temperature; and U is the overall heat transfer coefficient determined for wall conduction, and environmental convection and radiation, given as:

$$U^{-1}=\frac{l_{\mathrm{wall}}}{k_{\mathrm{wall}}}+\left[h_{\mathrm{conv}}+h_{\mathrm{rad}}\right]^{-1} \tag{5.15}$$

where l_{wall} is the wall thickness; k_{wall} is the wall thermal conductivity; h_{conv} is the environmental convective heat transfer coefficient; and h_{rad} is the linearized radiative heat transfer coefficient between external cavity surfaces with an assumed constant total, hemispherical surface emissivity [179]. Temperature jumps (i.e., Deissler's jump boundary condition) between the flow and wall interfaces were neglected due to a large conduction-radiation parameter for the particles [180]. One-dimensional, steady heat transfer was assumed through the cavity walls to the environment, given as:

$$q_{\mathrm{net,i}}=U\left[T_{s,i}-T_{\infty}\right] \tag{5.16}$$

where $T_{\mathrm{s},i}$ is the cavity surface temperature. Convective losses on the external window surface were assumed, given as:

$$q_{\mathrm{net,int}}+q_{\mathrm{net,ext}}=h_{\mathrm{conv}}\left(T_{\mathrm{window}}-T_{\infty}\right) \tag{5.17}$$

The coupled energy transport, species transport, and radiative exchange equations were solved iteratively until absolute convergences of bed temperature, conversion, and cavity wall temperatures were less than $1\text{x}10^{-3}$ K, $1\text{x}10^{-6}$, and $1\text{x}10^{-3}$ K respectively.

The overall performance for a range of operating conditions was evaluated by determining the mass weighted average outlet α and heat flow, given, respectively, as:

$$\bar{\alpha} = \frac{\int \alpha u \sum \left[\left(n_{\mathrm{i}} \cdot M_{\mathrm{i}} \right) / \left(\delta x \cdot \delta y \cdot \delta z \right) \right] dA|_{\mathrm{outlet}}}{\dot{m}_{\mathrm{outlet}}} \tag{5.18}$$

$$\dot{m}_{\mathrm{outlet}} h_{\mathrm{outlet}} = \int u \sum \left[\left(n_{\mathrm{i}} \cdot h_{\mathrm{i}} \right) / \left(\delta x \cdot \delta y \cdot \delta z \right) \right] dA|_{\mathrm{outlet}} \tag{5.19}$$

where $\dot{\mathrm{m}}_{outlet}$ is the outlet mass flow rate; M_{i} is the molar mass of a given species; $\left(\delta \mathrm{x} \cdot \delta \mathrm{y} \cdot \delta \mathrm{z} \right)$ is the discretized element volume; and h_{outlet} is the specific enthalpy on a mass basis at the outlet. The average outlet flow temperature, $\bar{\mathrm{T}}$, was determined iteratively using $\bar{\alpha}$ and $\dot{m}_{\mathrm{outlet}} h_{\mathrm{outlet}}$. The reactor absorption efficiency was determined as:

$$\eta_{\mathrm{abs}} = \frac{\int u \left[\left(\sum_{\mathrm{outlet}} n_{\mathrm{i}} h_{\mathrm{i}} - \sum_{\mathrm{inlet}} n_{\mathrm{i}} h_{\mathrm{i}} \right) \Big/ \left(\delta x \cdot \delta y \cdot \delta z \right) \right] dA}{\dot{Q}_{\mathrm{HFSS}}} + \frac{\int \left[\left(\frac{1}{2} r_{\mathrm{Co_3O_4}} \right) \Big/ \left(\delta x \cdot \delta y \cdot \delta z \right) \right] h_{\mathrm{O_2\,at}\,T} dV}{\dot{Q}_{\mathrm{HFSS}}} \tag{5.20}$$

where $\dot{Q}_{\mathrm{HFSS}}$ is the radiative input supplied by the HFSS.

A parametric study was performed using a face-centered central composite design (CCD) response surface to assess optimal performance. Second order response surfaces were used to evaluate average outlet conversion extent, average outlet flow temperature; and maximum bed temperature, given as:

$$y_{\mathrm{RS}} = \sum_{i}^{N} \omega_{ii} x_i^2 + \sum_{i}^{N} \sum_{j}^{N} \omega_{ij} x_i x_j + \sum_{i}^{N} \omega_i x_i + \omega_{\mathrm{o}} + \psi \tag{5.21}$$

where N is the number of simulations tested; ω are fitting coefficients; ψ is the independent and normally distributed fitting error; and x is the model parameter of interest. The response surfaces were evaluated and simplified using stepwise regression and analysis of variance to identify statistically significant parameters and parameter interactions. The root mean error sum of squares (RMSE) and the adjusted R^2 value were used to evaluate the quality of the fitted response surfaces.

5.4 Results and Discussion

The heat and mass transfer model coupled to chemical kinetics was evaluated over a range of conditions to determine the sensitivity of response variables to changes in model inputs, shown in Table 5.1.

Table 5.1. Model input parameters for the heat and mass transfer model coupled to chemical kinetics for a solar thermochemical inclined granular-flow reactor

Parameters	Values
C	3250-3979 suns (1 sun = 1000 W/m^2)
I	1000 W/m^2
d_{aperture}	40 mm
$\dot{Q}_{\text{HFSS}}$	4.1 – 5.0 kW$_{\text{th}}$
cavity material	diffuse, Zircar Zirconia M-35 buster type alumina
w_{cavity}, h_{cavity}	150 mm
l_{walls}	100 mm
k_{wall}, $k_{Co_3O_4/CoO}$	0.27, 10· W/mK
h_{conv}	20 W/m^{2}K
T_∞	300 K
d_{p}	100 µm
H_{sf}	5
$\rho_{Co_3O_4,CoO}$	6110, 6440 kg/m^3
p_{O_2}	3 mbar
l_{cavity}	0 - 125 mm
T_{inlet}	400 - 700 K
θ_{slope}	28.7 – 37.8°
$\varepsilon_{\text{cavity walls}}$	0.5 (0-4 µm), 0.95 (4-12 µm), and 0.8 (12µm-∞)
α_{window}	0 (0-4 µm) and 0.9 (4 µm-∞)
ρ_{window}	0.06 (0-4 µm) and 0.1 (4 µm-∞)
τ_{window}	0.94 (0-4 µm) and 0 (4 µm-∞)
$\varepsilon_{\text{flow}}$	0.85
$\varepsilon_{\text{outer}}$	0.8

·Assumed value, similar order of magnitude to other metal oxides at T > 500 K[181]

To ensure mechanical stability of the window, a P_f = 0.1% was used to determine maximum allowable tensile stresses for spherical and flat windows of 34.6 MPa and 34.0 MPa, respectively. Window thicknesses were tested iteratively in a Solidworks finite element model until the maximum window stress was less than the maximum allowable stress for a given window type. The stressed area of the window was determined assuming a 100 mm deep conical section between the window and the 40 mm diameter reactor aperture. Both flat and domed windows covered a 170 mm diameter region with the spherical window radius of curvature centered at the aperture. The minimum thicknesses

for a flat and domed window were 4.7 mm and 0.95 mm, respectively. The thinner, spherical window was a result of the window being subjected primarily to compressive stresses. Von Mises stress contours from the finite element analysis for the spherical window design are shown in Figure 5.3. This analysis demonstrated that quartz window mechanical stability for both the flat and spherical geometries was not a limiting factor in the design of STInGR.

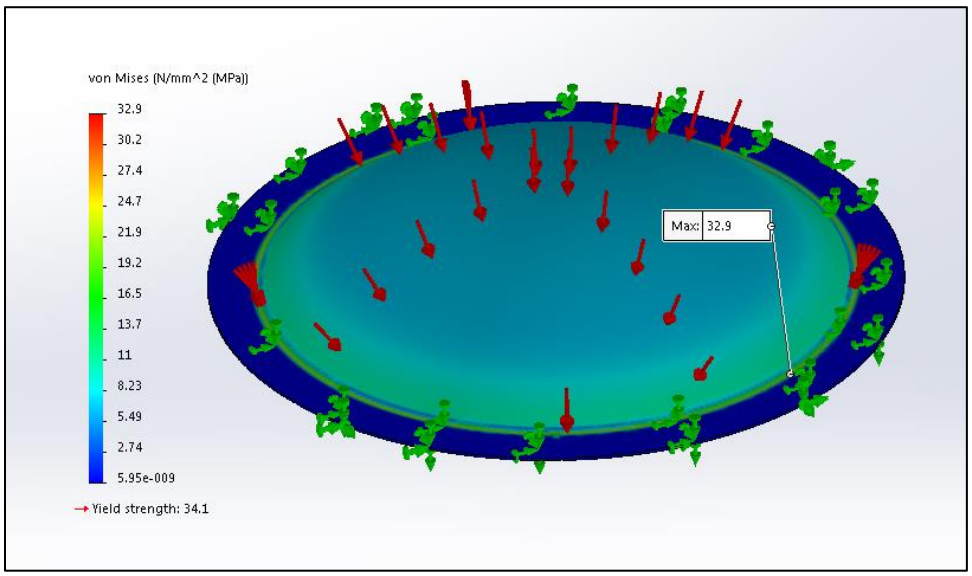

Figure 5.3. Results of finite element analysis for the 0.95 mm thick spherical window covering a 170 mm diameter region with radius of curvature centered at the reactor aperture for a 100 MPa distributed load across the window exterior

The granular flow was modeled based on empirical data for non-spherical sand particles with a d_p = 800 μm and negligible inter-particle cohesion where β = 0.65, γ = 0.77, θ_1 = 27°, θ_2 = 43.4°, and L = 2.03 [132]. The resulting granular flow is shown in Figure 5.4 for (a) $\bar{t}_{res}$ as a function of θ_{slope} and (b) u as a function of bed depth over a range of θ_{slope}'s for H_{sf} = 5 and d_p = 100 μm. The d_p and H_{sf} were selected to maximize $\bar{t}_{res}$ for a given θ_{slope}, neglecting the influence of inter-particle cohesion upon the flow behavior. For granular solids with $d_p \geq 100$ μm, the cohesive effects did not influence the flow, as was the case

for granular powders with 100 μm > $d_p \geq 10$ μm, and superfine powders with $d_p < 10$ μm that are highly cohesive [182]. $\bar{t}_{res}$ increased monotonically with decreasing θ_{slope} due to the reduced shear stress on the bed as shown in Figure 5.4a. u exhibited a nearly-linear increase with distance from the inclined surface for all θ_{slope}'s as shown in Figure 5.4b. The $\partial u/\partial z$ increased as greater shear stresses acted upon the bed for larger θ_{slope}. This velocity profile was used as a predictor of spatial particle residence times within the bed. Particles with the shortest residence times were located at the free surface and directly exposed to concentrated irradiation, which facilitated rapid heating rates compared to the bottom of the bed.

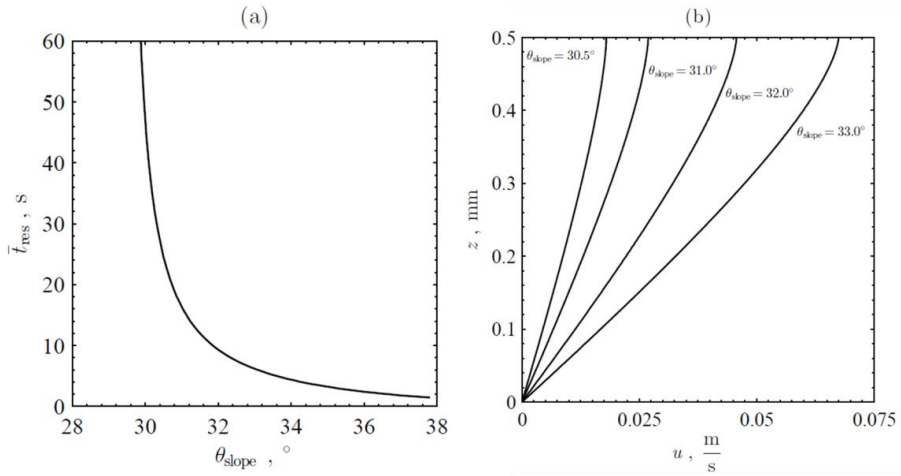

Figure 5.4. Granular flow model results for (a) estimated average particle residence time as a function of inclination angle and (b) flow velocity profiles as a function of bed depth for a thin bed containing uniform particles with a diameter of 100 μm with a flow depth to particle diameter ratio of five flowing along a 30.5° inclined slope with a cavity height of 150 mm

A complete reactor model was analyzed using a face-centered CCD parametric study with parameters: 1) l_{cavity} (0 - 125 mm), 2) T_{inlet} (400 - 700 K), and 3) C (3250-3979 suns). Response surfaces were developed for predicting $\bar{T}$, $\bar{\alpha}$, and T_{max} and were used to identify optimal STInGR performance: defined as largest $\bar{T}$ and $\bar{\alpha}$ where T_{max} was below

1573 K to avoid particle sintering [37] and associated disruptions of the flow. Individual response surface effects and parameter interactions were evaluated using analysis of variance, with overall results included in Table 5.2.

Table 5.2. Analysis of variance table comparing the effects and interactions of user-defined parameters for producing response surfaces of average outlet conversion, average outlet flow temperature, and maximum bed temperature

$\bar{\alpha}_{RS}$					
Source of Variance	SS	df	MS	F	p-value
$l_{\text{cavtiy}} \cdot l_{\text{cavtiy}}$	8.8901e-05	1	8.8901e-05	1.2814	0.2649
$T_{\text{inlet}} \cdot T_{\text{inlet}}$	0.0002	1	0.0002	2.4172	0.1285
$C \cdot C$	0.0007	1	0.0007	10.466	0.0026
l_{cavtiy}	0.0978	1	0.0978	1410.2	4.5963e-31
T_{inlet}	0.1550	1	0.1550	2233.6	1.0999e-34
C	0.4075	1	0.4075	5874.3	2.2477e-42
$l_{\text{cavtiy}} \cdot T_{\text{inlet}}$	0.0024	1	0.0024	35.025	8.1023e-07
$l_{\text{cavity}} \cdot C$	0.0021	1	0.0021	30.735	2.6038e-06
$T_{\text{inlet}} \cdot C$	0.0034	1	0.0034	48.968	2.8546e-08
Error	0.0026	37	6.9376e-05	1	0.5
$\bar{T}_{RS}$					
Source of Variance	SS	df	MS	F	p-value
$l_{\text{cavtiy}} \cdot l_{\text{cavtiy}}$	1254.3	1	1254.3	18.073	0.00014
$T_{\text{inlet}} \cdot T_{\text{inlet}}$	802.94	1	802.949	11.569	0.0016
$C \cdot C$	889.97	1	889.97	12.823	0.0010
l_{cavtiy}	3099.3	1	3099.3	44.656	7.5356e-08
T_{inlet}	16363	1	16363	235.77	1.2423e-17
C	54209	1	54209	781.08	1.7761e-26
$l_{\text{cavtiy}} \cdot T_{\text{inlet}}$	1852.4	1	1852.4	26.691	8.4287e-06
$l_{\text{cavity}} \cdot C$	1765.4	1	1765.4	25.437	1.2332e-05
$T_{\text{inlet}} \cdot C$	3585.5	1	3585.5	51.662	1.5962e-08
Error	2567.9	37	69.403	1	0.5
$T_{\text{max,RS}}$					
Source of Variance	SS	df	MS	F	p-value
$l_{\text{cavtiy}} \cdot l_{\text{cavtiy}}$	9809.4	1	9809.4	14.554	0.0005
$T_{\text{inlet}} \cdot T_{\text{inlet}}$	2346.1	1	2346.1	3.4809	0.0700
$C \cdot C$	2671.3	1	2671.3	3.9633	0.0539
l_{cavtiy}	266080	1	266080	394.77	2.4707e-21
T_{inlet}	52979	1	52979	78.602	1.0976e-10
C	312191	1	312191	463.18	1.6165e-22
$l_{\text{cavtiy}} \cdot T_{\text{inlet}}$	1038.15	1	1038.15	1.5402	0.2224
$l_{\text{cavity}} \cdot C$	2444.9	1	2444.9	3.6273	0.0646
$T_{\text{inlet}} \cdot C$	629.79	1	629.79	0.9344	0.3400
Error	24939	37	674.01	1	0.5

Response surfaces for $\bar{\alpha}_{RS}$, $\bar{T}_{RS}$ and $T_{max,RS}$ were produced from statistically significant parameters and interactions selected using stepwise regression [183] with predictor variables added if p-value < 0.05 or with predictor variables removed if p-value > 0.1 for the partial F-test of the change in the sum of squares error [184]. Resulting fits were evaluated with the goodness of fit statistics included in Table 5.3.

Table 5.3. Goodness of fit statistics for fitted response surfaces of average particle outlet conversion, average particle outlet temperature , and maximum flow temperature

Response Surface	RMSE	Adjusted R^2
$\bar{\alpha}_{RS}$	0.0084	0.996
$\bar{T}_{RS}$	8.33 K	0.964
$T_{max,RS}$	27.6 K	0.959

Contours of $\bar{\alpha}_{RS}$ are shown in Figure 5.5 for a range of l_{cavity}, C, and T_{inlet} with the shaded areas denoting regions where $T_{max,RS}$ >1573 K. $\bar{\alpha}_{RS}$ increased monotonically with decreasing l_{cavity}, increasing T_{inlet}, and increasing C as shown in Fig. 5 (a-i). An increase in T_{inlet} with constant C and l_{cavity} decreased the concentrated irradiation needed to achieve the temperatures required to thermally reduce Co_3O_4. An increase in C with constant T_{inlet} and l_{cavity} resulted in additional incident radiation which increased the flow temperature and $r_{Co_3O_4}$, which drove an increased reduction extent. An increase in l_{cavity} with constant T_{inlet} and C resulted in a greater fraction of $\dot{Q}_{HFSS}$ directly absorbed by the bed due to the directional nature of the input radiation which increased the flow temperature and $r_{Co_3O_4}$ and resulted in an increased extent of reduction. $\bar{\alpha}_{RS}$ was almost equally influenced by T_{inlet} and l_{cavity} for constant C as shown in Figure 5.5 (a-c) while $\bar{\alpha}_{RS}$ was more strongly influenced by C than l_{cavity} or T_{inlet} as shown in Figure 5.5 (d-i). Significant parameter combinations lie within shaded regions where $T_{max,RS}$ > 1573 K and were associated with

high T_{inlet}, small l_{cavity}, large C, and $\bar{\alpha}_{RS} > 0.7$ as shown in Figure 5.5 (c), (d), and (i). This behavior resulted from the directional nature of incident radiation which produced localized spikes in flow temperature and conversion where additional incident radiation was stored sensibly and further increased the flow temperature. This behavior was further evidenced by the delayed onset of shaded regions to $\bar{\alpha}_{RS} > 0.85$ in Figure 5.5 (f) as incident radiation was more uniformly distributed across the flow for l_{cavity} = 125 mm and resulted in lower magnitude localized spikes in temperature and conversion.

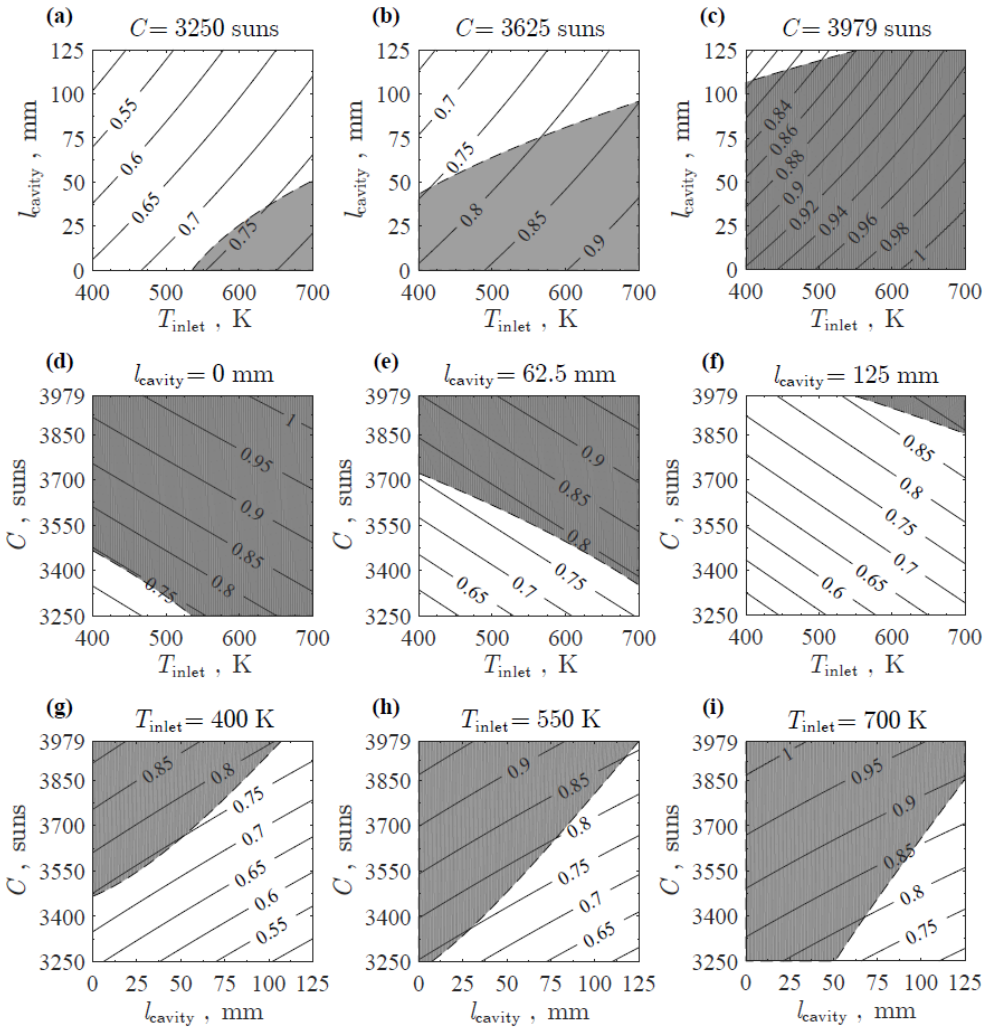

Figure 5.5. Response surfaces for granular flow average outlet conversion from Co3O4 to CoO for (a-c) varying slope distance from the aperture and flow inlet temperature and a fixed solar concentration ratio, (d-e) varying solar concentration ratio and flow inlet temperature and a fixed slope distance from the aperture, and (g-i) varying solar concentration ratio and slope distance from the aperture and a fixed flow inlet temperature. The shaded areas denote regions where the maximum temperature exceeded the sintering temperature of 1573 K.

Contours of $\overline{T}_{RS}$ are shown in Figure. 5.6 for a range of l_{cavity}, T_{inlet}, and C with the shaded areas denoting regions where $T_{max,RS} > 1573$ K. $\overline{T}_{RS}$ increased with increasing C and increasing T_{inlet} as shown in Figure. 5.6 (a-i). An increase in C for constant T_{inlet} and l_{cavity} resulted in additional incident radiation which increased the flow temperature. An increase in T_{inlet} for constant l_{cavity} and C resulted in more sensible energy imparted to the

incoming flow which required less solar irradiation to heat the flow to a similar outlet temperature. $\overline{T}_{RS}$ increased with increasing l_{cavity} for constant T_{inlet} < 550 K and constant C < 3550 suns as shown in Figure. 5.6 (a) and (g). However, $\overline{T}_{RS}$ increased with increasing l_{cavity} < 50 mm and decreased with increasing l_{cavity} > 50 mm for constant T_{inlet} > 550 K and constant C > 3550 suns as shown in Fig. 6 (b-f) and (h-i). An increase in l_{cavity} for constant T_{inlet} < 550 K and C < 3550 suns resulted in a more uniform distribution of incident radiation across the flow and a decrease in conversion which , respectively, decreased re-emission from the flow and increased sensible energy storage. This same behavior occurred with increasing l_{cavity} < 50 mm for constant T_{inlet} > 550 K and constant C > 3550 suns, however with increasing l_{cavity} > 50 mm for constant T_{inlet} > 550 K and constant C > 3550 suns increased upstream flow temperatures and re-emission from the flow resulted in significantly increased heat losses through the cavity walls which decreased the average outlet flow temperature. The same behavior for shaded regions where $T_{max,RS}$ > 1573 K shown in Figure 5.5 is also shown in Figure. 5.6.

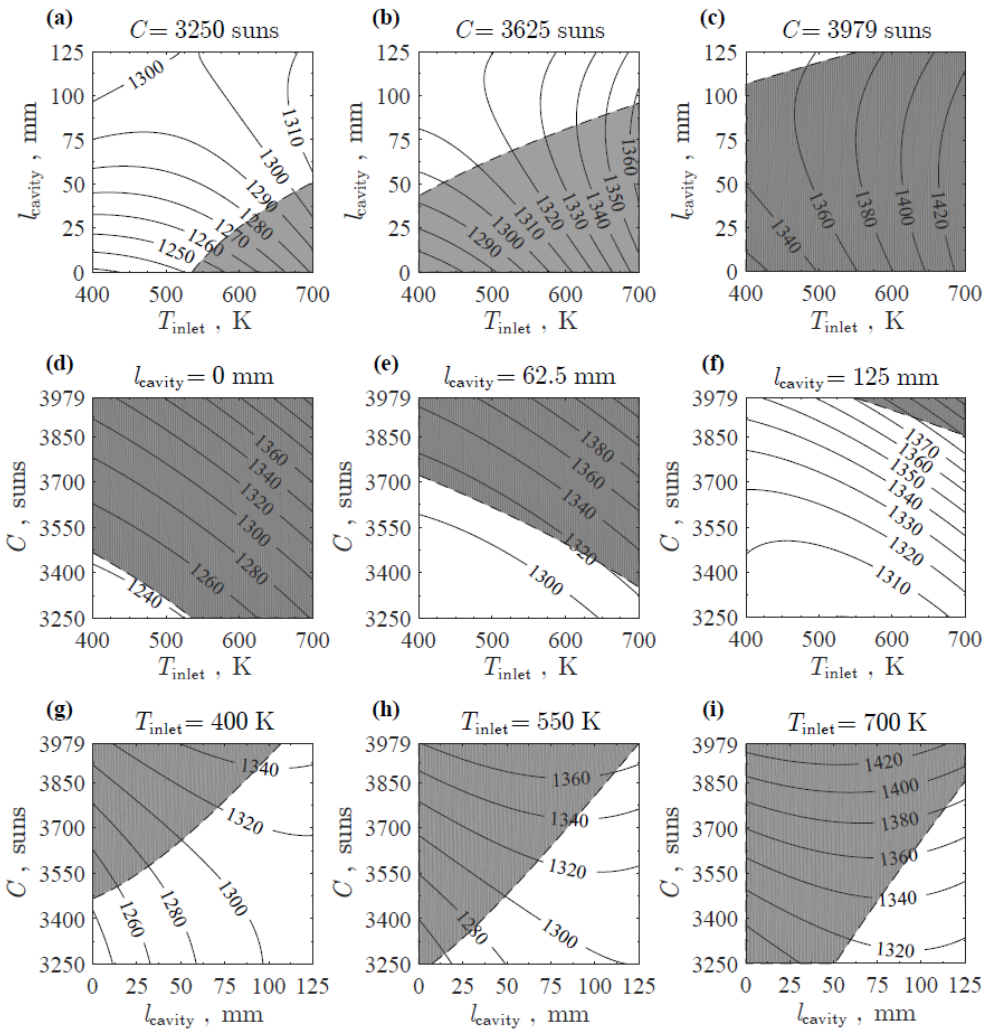

Figure. 5.6. Response surfaces for granular flow average outlet temperature from Co_3O_4 to CoO for (a-c) varying slope distance from the aperture and flow inlet temperature and a fixed solar concentration ratio, (d-e) varying solar concentration ratio and flow inlet temperature and a fixed slope distance from the aperture, and (g-i) varying solar concentration ratio and slope distance from the aperture and a fixed flow inlet temperature. The shaded areas denote regions where the maximum temperature exceeded the sintering temperature of 1573 K.

From the parametric study results, a reactor design for maximum conversion occurred when C = 3979 suns, l_{cavity} = 0 mm, and T_{inlet} = 700 K, resulting in a $\bar{\alpha}$ = 1.0, $\bar{T}$ = 1448 K, T_{max} = 1870 K, and η_{abs} = 0.83. Optimal performance in the absence of particle sintering corresponded to C = 3825 suns, l_{cavity} = 125 mm, and T_{inlet} = 700 K, resulting in $\bar{\alpha}$ = 0.89, $\bar{T}$ = 1377 K, T_{max} = 1559 K, and η_{abs} = 0.76. Isometric views of granular flow

temperature contours and conversion contours for the optimum reactor design are given in Figure 5.7(a) and (b), respectively. In Figure 5.7 flow was introduced along the top of the slope at x = 0 mm and was removed from the reactor at the base of the slope where x = 295.5 mm. The granular flow was directly irradiated along the free surface at z = 0.5 mm and granular flow nearest the alumina slope was located at z = 0 mm. The flow traveled along the slope in the x direction and heated gradually and uniformly until flow at the free surface became directly irradiated by individual lamps, which produced local temperature spikes as shown in Figure 5.7 (a). The locations of four local temperature spikes along the free surface are given in Table 5.4.

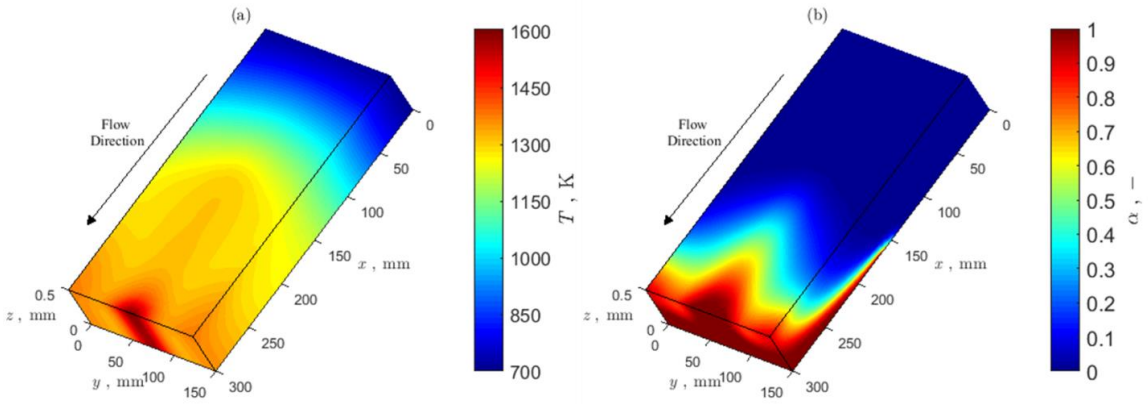

Figure 5.7. Contours of granular flow (a) temperature and (b) Co_3O_4-to-CoO conversion for 5 particle diameter thick steady flow along the reactor inclined slope within a diffuse, alumina cavity of 150 mm height and width and 30.5˚ angle of inclination, 700 K particle inlet temperature, solar concentration ration of 3825 suns, and 125 mm slope displacement from aperture

Table 5.4. Local temperature spikes along flow free surface produced from individual high flux solar simulator lamps

Temperature Spike	*x* location [mm]	*y* location [mm]	HFSS Lamp
1	180	75	7
2	295.5	0	6
3	295.5	150	2
4	295.5	75	1

The highest flow temperatures occurred at the flow outlet because of near normal irradiation from lamp 1. More temperature spikes resulted from irradiation from Lamps 7, 6, and 2. Direct irradiation supplied by lamps 1, 6, and 2 primarily impinged upon the alumina cavity surfaces with some spillage and re-emissions incident on the flow. Irradiation from lamps 3-5 directly impinged on the top of the bare alumina cavity without local temperature spikes in the particle flow. Despite low k_{eff}, the temperature difference between the free surface and inclined slope reached a maximum of 30.5 K as absorbed heat was used to drive thermal reduction of the material and longer residence times of lower layer particles resulted in particles with similar temperatures to layers above. As particles traveled along the slope $T \geq T_{\text{eq}}$ of 1061 K for p_{O_2} = 3 mbar (i.e. $\Delta G = 0$) occurred along the free surface and alumina incline at x = 81 mm and x = 86 mm, respectively, as particles along the free surface heated more rapidly due to direct irradiation.

Free surface flow never achieved an average of $\alpha \geq 0.95$ across w_{cavity} while flow along the inclined surface achieved an average $\alpha = 0.95$ across w_{cavity} at x = 172.8 mm as shown in Figure 5.7 (b). Particles attained larger α as $z \rightarrow 0$ mm due to increased particle residence times. On the free surface, local spikes in α occurred as the flow passed through local spikes in temperature, compensating for shorter residence times. In Figure 5.7 b along the x-z plane for y =150 mm and $x \geq 270$ mm, as $z \rightarrow 0.5$ mm α decreased due to decreasing particle residence times until near the free surface where α suddenly increased due to direct irradiation absorbed at the surface. The lowest values of α at the particle outlet occurred just below the free surface between high temperature regions 2 and 4 and between high temperature regions 3 and 4 as these particles experienced short residence times and did not pass directly through a local temperature spike. For this optimal reactor operation

T_{window} = 1175 K, where the maximum suggested operating temperature of electrically fused quartz from Heraeus Quarzglas is 1433 K [185].

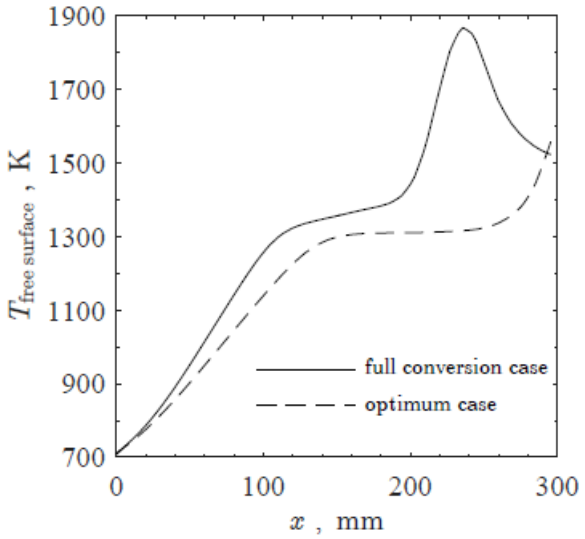

Figure 5.8. Granular flow free surface temperatures along flow center (y = 75 mm) for parametric study cases where (solid) full conversion of Co_3O_4 to CoO is achieved with 0 mm slope displacement from aperture, 700 K flow inlet temperature, and solar concentration ratio of 3979 suns and where (dashed) optimum reactor performance is achieved with 125 mm slope displacement from the aperture, 700 K flow inlet temperature, and solar concentration ratio of 3825 suns for 5 particle diameter thick steady flow along the reactor inclined slope within a diffuse, alumina cavity of 150 mm height and width, and 30.5˚ angle of inclination.

The flow free surface temperature along y = 75 mm and z = 0.5 mm for the parametric study cases which achieve maximum conversion and optimal reactor performance are compared in Figure 5.8. The flow free surface entered the reactor cavity at x = 0 mm and traveled along x where both cases were rapidly heated until 100 mm ≤ x ≤ 130 mm where $\partial T/\partial x$ decreased which was associated with significant Co_3O_4 reduction. $\partial T/\partial$x ~ 0 for the optimum case for 130 mm ≤ x ≤ 230 mm as incident radiation was more uniformly distributed across the flow and was primarily stored during Co_3O_4 reduction. For the full conversion case, temperature suddenly increased at x = 190 mm and was associated with

local heating due to near-normal incident radiation supplied by lamp 1 and subsequently decreased at x = 250 mm a result of re-emission from the flow surface. The optimum reactor case exhibited a similar surface temperature increase at x = 275 mm but was less pronounced and was shifted further downstream as incident radiation from lamp 1 primarily impinged upon bare cavity surfaces. The combination of lower T_{max} and the improved pairing of incident radiation and Co_3O_4/CoO reaction kinetics reinforced the selection of the optimum reactor design.

5.5 Model Verification

Grid independence studies were conducted on STInGR designs with parameters h_{cavity} = 150 mm, w_{cavity} = 150 mm, l_{cavity} = 0, 125 mm, θ_{slope}= 30.5°, d_p = 100 µm, $t_{insulation}$ = 100 mm, and C = 3979 suns where response variables η_{abs}, $\bar{\alpha}$, $\bar{T}$, changed less than 0.05%. Additionally, the ratios between the flow/cavity surface temperature root mean square difference and the flow/cavity surface temperature range were less than 1.5 % between examined grids.

Results of energy modeling were verified by performing energy and mass balances with a defined control volume which encompassed the entire reactor and assumed all O_2 produced during reduction was removed from the reactor, given as:

$$\dot{Q}_{HFSS} = \int u\left[\left(\sum_{outlet} n_i h_i - \sum_{inlet} n_i h_i\right)\Big/\left(\delta x \cdot \delta y \cdot \delta z\right)\right] dA + \int\left[\left(\frac{1}{2} r_{Co_3O_4}\right)\Big/\left(\delta x \cdot \delta y \cdot \delta z\right)\right] h_{O_2 \text{ at } T}\, dV + \dot{Q}_{loss} \tag{5.22}$$

$$\dot{m}_{\text{inlet}} = \int \alpha u \sum \left[\left(n_{\text{i}} M_{\text{i}} \right) / \left(\delta x \cdot \delta y \cdot \delta z \right) \right] dA|_{\text{outlet}} + \int \left[\left(\frac{1}{2} r_{\text{Co}_3\text{O}_4} M_{\text{O}_2} \right) \Big/ \left(\delta x \cdot \delta y \cdot \delta z \right) \right] dV \quad (5.23)$$

where $\dot{Q}_{\text{loss}}$ refers to the net total radiative, conductive, and convective heat loss from the reactor. The energy balance for all cases examined closed to within 0.3 % of $\dot{Q}_{\text{HFSS}}$ while the mass balance for all cases examined closed to within 0.002% of $\dot{m}_{\text{inlet}}$.

5.6 Conclusions

A 5 kW_{th} solar thermochemical reactor concept for thermally reducing a Co_3O_4 was modeled by coupling heat transfer mechanisms to chemical kinetics and granular particle flow correlations at steady state. Flowing Co_3O_4 particles were directly exposed to concentrated irradiation entering through a quartz window that also enabled operation at vacuum conditions. Mechanical failure analysis was performed on flat and spherical window designs, resulting in 4.7 mm flat quartz window and 0.95 spherical quartz window. A face-centered central composite design parametric study was performed that varied the distance between the inclined slope base and aperture (0–125 mm), flow inlet temperature (400 K–700 K), and solar concentration ratio (3250–3979 suns). From the parametric study and subsequent statistical analyses, inferences were made to assess the input responses on the average outlet flow conversion, average outlet flow temperature, and maximum bed free surface temperature. Optimal performance corresponded to when the bottom of the slope was 125 mm from the aperture, the particle inlet temperature was 700 K, and solar concentration ratio equaled 3825 suns, resulting in an average outlet conversion of 0.89, average outlet temperature of 1397 K, maximum flow temperature of 1559 K, and absorption efficiency of 0.76. These results provide engineering guidance for fabrication

and experimental study of an optimized solar thermochemical reactor to thermally reduce Co_3O_4 at laboratory-scale and provide additional guidance for reactor scale up.

CHAPTER 6. MONTE CARLO-CFD MAPPING[3]

6.1 Introduction

Monte Carlo ray tracing (MCRT) and finite volume approximations to the radiative transport equation (FV–RTE) are two methods for modeling solar inputs in receiver/reactor models. An algorithmically simple method of MCRT–CFD mapping was developed that introduced no spatial or energy conservation errors beyond the MCRT precision and CFD mesh resolution. The method was applicable for both 2D or 3D, for structured or unstructured meshes, for commercial or in-house CFD models, and for surfaces of any shape and orientation.

6.2 Methodology

Monte Carlo ray tracing (MCRT) allows for the directional modeling of radiative heat transfer by partitioning reflections or emissions from a radiation source, in this case concentrating solar collectors (*e.g.* heliostats, parabolic troughs/dishes) or generating devices (*e.g.* high flux solar simulators; HFSS), into rays or individual packets of energy, represented as:

$$\dot{E}_{\mathrm{k}} = \frac{\dot{Q}_{\mathrm{sun}}}{N_{\mathrm{rays}}} \tag{6.1}$$

[3] Mapping and validation performed in collaboration with Dr. H. Evan Bush. MCRT of the high-flux solar simulator was performed by Robert Gill.

where $\dot{Q}_{sun}$ is the total radiative power, here assumed to be evenly partitioned among N rays. N_{rays} is typically between 10^5 and 10^7, and MCRT convergence is expected for . The path of a given ray $k = 1, 2, \ldots, N_{rays}$ is defined via [102]:

$$\vec{r}_k = \vec{r}_{0,k} + D\hat{s}_k \tag{6.2}$$

where $\vec{r}_k$ is the ray intersection located a distance D and direction from the ray origin . The origin may be the point of ray generation (*i.e.* introduction to the model) or the point of the previous ray interaction (*e.g.* reflection, scattering) in the system.

6.2.1 Irradiated Surface Mapping

A point mapping algorithm is applied to ray intersections to translate absorbed irradiation from a MCRT model to boundary sources in a computational fluid dynamics (CFD) model. The mapping for a group of $\vec{r}_k$ depicted as red points is given in Figure 6.1 for a solar reactor aperture and cavity. A detail view shows the mapping for two $\vec{r}_k$ on a single mesh face F_i of the CFD model. The $\vec{r}_k$ are transformed to a local, barycentric coordinate system $(\hat{t}_1, \hat{t}_2)$ on F_i to determine whether they fall within the boundaries of, and should be mapped to, F_i. The process is repeated until all $\vec{r}_k$ are sorted into a given F_i.

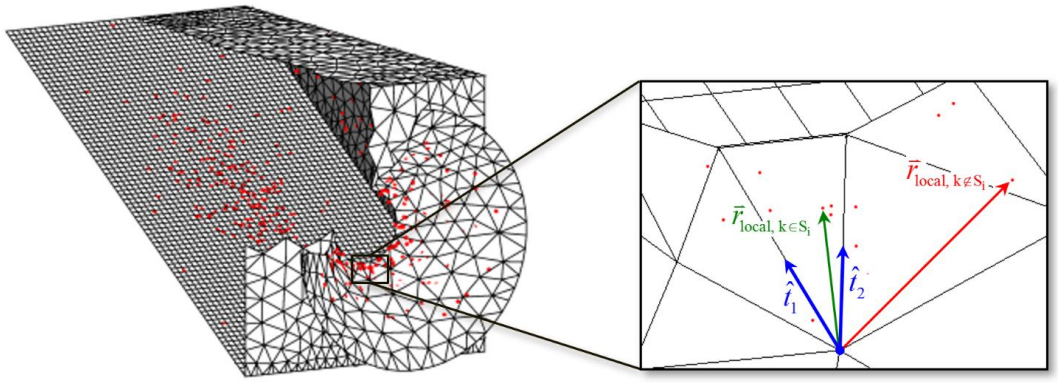

Figure 6.1. Monte Carlo ray tracing intersections (red points) on the surfaces of a solar reactor (left) overlaid on the computational mesh (black lines) to which the rays are coupled; and (right) a detail view of a mesh face on the reactor aperture with basis vectors of the local coordinate system (blue, not to scale) for ray mapping, as well as the position vectors of two ray intersections: one within the mesh face (green) and one not (red)

For triangular F_i, the local coordinate system origin is defined at any of the three F_i vertices, where the basis vectors $\hat{t}_1$ and $\hat{t}_2$ are unit vectors in the directions from the origin to each of the two remaining F_i vertices, respectively. For quadrilateral or greater F_i, the face is first subdivided into multiple triangular subcomponents which are each tested. The two-dimensional, local intersection position vectors are defined as:

$$\vec{r}_{\text{local}} = a\hat{t}_1 + b\hat{t}_2 \tag{6.3}$$

where (a,b) are the local coordinate dimensions. The subset of rays falling within F_i is defined by:

$$S_i = \left\{ k = 1, 2, \ldots, N_{\text{rays}} : a_{i,k},\ b_{i,k} > 0,\ a_{i,k} + b_{i,k} \le 1 \right\} \tag{6.4}$$

The direct mapping method is depicted in Figure 6.1 for two example intersections at the given F_i, where one intersection (green vector) falls within F_i and one (red vector) falls outside F_i.

CFD model boundary sources for each F_i are computed from mapped, summed ray energies as:

$$q''_{\text{sun,i}} = \left(\alpha H_0\right)_{\text{sun,i}} = \frac{1}{A_{\text{s,i}}} \sum_{k \in S_i} \dot{E}_k \tag{6.5}$$

where $(\alpha H_0)_{\text{sun}}$ is the absorbed component of the surface irradiation profile $H_{0,\text{sun}}$; and A_s is the face surface area. The summation is limited only to the rays within the subset *S*. The boundary sources are incorporated into a general surface-fluid mixed boundary condition to the heat diffusion equation as:

$$-k_{\text{n,i}} \left.\frac{\partial T}{\partial n}\right|_{\text{s,i}} + q''_{\text{sun,i}} = U_i \left(T_{\text{s,i}} - T_{\infty,\text{i}}\right) + q''_{\text{R,i}} \tag{6.6}$$

where the first term on the left-hand side is the conductive heat flux in the direction normal to the surface *n* and the first and second terms on the right-hand side are the convective and radiative heat fluxes, respectively. The convective heat flux uses an overall heat transfer coefficient *U* to account for contact resistance and/or thin-wall conduction. The net radiative heat flux q''_R resulting from internal reemission and reflection is computed via the FV-RTE.

6.2.2 Participating Volumetric Cell Mapping

MCRT has been employed to model heat transfer within radiatively participating media in solar receivers/reactors with quartz windows [107, 186-188], reticulated porous ceramics/metal foams [189-192], and particulate media [193-196]. Participating media attenuates directional input radiation by absorption and scattering within the modeled

medium, augmenting the resultant surface heat fluxes. The D and $\hat{s}_k$ defining a given $\vec{r}_k$ are additionally dependent upon absorption, scattering, and interface refraction.

Volumetrically absorbed rays may be mapped into the discretized volumetric domain by a similar algorithm to surface mapping: globally-defined points of absorption $\vec{r}_k$ are transformed into a local, barycentric coordinate system $(\hat{t}_1, \hat{t}_2, \hat{t}_3)$ based on the tetrahedral element C_i. For more complex element shapes, the C_i is first subdivided into M tetrahedral sub-elements which are each tested. Subdivision of a given element C_i and volumetric mapping of two $\vec{r}_k$, depicted as red points, are depicted in Figure 6.2, where the transparent surface bounds a sub-element.

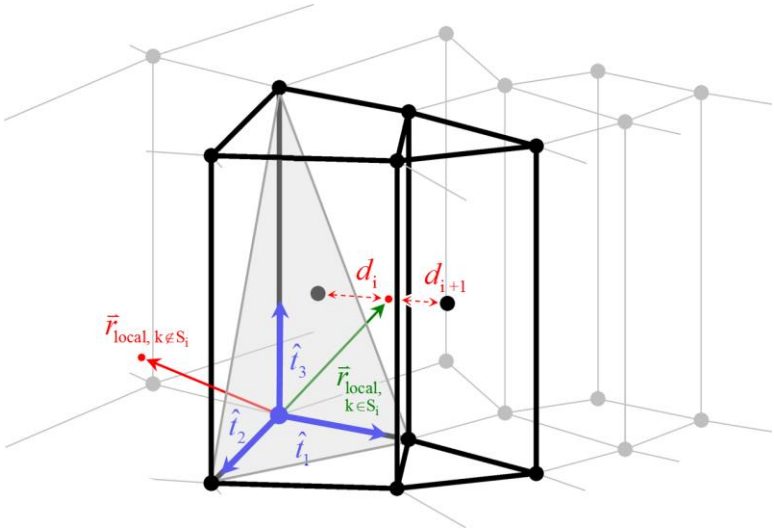

Figure 6.2. Monte Carlo ray tracing intersections (red points) within a discretized computational mesh (gray wireframe) to which the rays are coupled, with: 1) bases vectors of the local coordinate system (blue, not to scale) for a tetrahedral region (transparent gray surface) of a given cell (black lines);2) position vectors of two ray intersections within the cell (green) and outside the cell (red); and 3) straight-line distances (red dashed) from one absorbed ray to the centroids of the cell and a neighbor (black wireframe)

The three-dimensional, local absorption point position vectors are defined as:

$$\vec{r}_{local} = a\hat{t}_1 + b\hat{t}_2 + c\hat{t}_3 \tag{6.7}$$

where (*a*,*b*,*c*) are the local coordinates. The subset of rays that fall within C_i is defined by:

$$S_i = \left\{ k = 1, 2, \ldots, N : a_{i,k},\ b_{i,k}, c_{i,k} > 0,\ a_{i,k} + b_{i,k} + c_{i,k} \le 1 \right\} \tag{6.8}$$

The direct mapping method is depicted in Figure 6.2 for two example intersections at the given C_i, where one intersection (green vector) falls within C_i and one (red vector) falls outside C_i.

Volumetric sources for each C_i are computed from mapped, summed ray energies as:

$$\dot{q}'''_{sun,i} = \left(\kappa \int_{4\pi} I(s')\, d\Omega' \right)_{sun,i} = \frac{1}{V_i} \sum_{k \in S_i} \dot{E}_k \tag{6.9}$$

where $\left(\kappa \int_{4\pi} I(\vec{s}')\, d\Omega' \right)$ is the absorbed component of the entering radiation from all directions $\vec{s}'$ and over all solid angles Ω' for a linear absorption coefficient κ; and V is the cell volume. The summation is limited only to the rays within the subset *S*. The volumetric heat sources are applied at each C_i as a term in the thermal energy transport equation, a common form of which is represented as:

$$\frac{\partial E_i}{\partial t} + \nabla \cdot \left(\rho \vec{V} h \right)_{nb,i} = \nabla \cdot \left(k \nabla T_i \right) + q'''_{sun,i} + q'''_{R,i} \tag{6.10}$$

where the left hand side includes the transient and convected energy from neighboring fluid cells *nb*, and the right hand side captures heat diffusion and the two energy source terms: 1) q'''_{sun}, and 2) the internal radiative balance computed via the FV-RTE q'''_R.

6.2.3 Hybrid Nearest Neighbor/Barycentric mapping

In a hybrid nearest-neighbor/barycentric direct mapping method, a neighborhood of the n nearest surface/volumetric elements to each $\vec{r}_{\mathrm{k}}$ is identified. The barycentric mapping is applied exclusively to this neighborhood, significantly reducing computational cost. The nearest-neighbor algorithm used to identify the neighborhood, or subset of elements eligible for mapping, is defined as:

$$S_{\mathrm{n,i}} = \left\{ k = 1, 2, \ldots, N_{\mathrm{rays}} \,\middle|\, d_{\mathrm{i,k}} \leq P_{d_{\mathrm{i}},\,\mathrm{n/N_{elements}}\cdot 100\%} \right\} \tag{6.11}$$

where $P_{d_{\mathrm{i}},\,\mathrm{n/N_{elements}}\cdot 100\%}$ is the percentile of the n nearest elements; and $d_{\mathrm{i,k}} = \sqrt{\left\| \vec{r}_{\mathrm{k}} - \vec{r}_{\mathrm{C_i}} \right\|_2}$ is the straight-line distance between $\vec{r}_{\mathrm{k}}$ and the cell centroid $\vec{r}_{C_i}$. For a sufficiently large neighborhood, the barycentric and hybrid methods produce identical mapping results.

It should be noted that, while an exclusively nearest-neighbor direct mapping would be computationally simpler than a barycentric or hybrid method, it could amplify discretization error and instability by erroneously mapping some rays to neighboring cells. This scenario is demonstrated in Figure 6.2 for the within C_{i}: since $d_{\mathrm{i+1}} < d_{\mathrm{i}}$, nearest-neighbor direct mapping would map the $\vec{r}_{\mathrm{k}}$ to the prism-shaped cell despite the $\vec{r}_{\mathrm{k}}$ falling within C_{i}. Such errors are more likely to occur for meshes with high skew and large, abrupt element size changes, biasing $\vec{r}_{\mathrm{k}}$ toward nearby small cells. Therefore, the nearest neighbor/barycentric mapping hybrid method is suggested.

A flow chart detailing the algorithms for direct surface and volumetric mapping from the MCRT to CFD modeling domains is depicted in Figure 6.3a and b, respectively. Directions and for implementing the algorithm in ANSYS Fluent v19.0 are included in Appendix A.

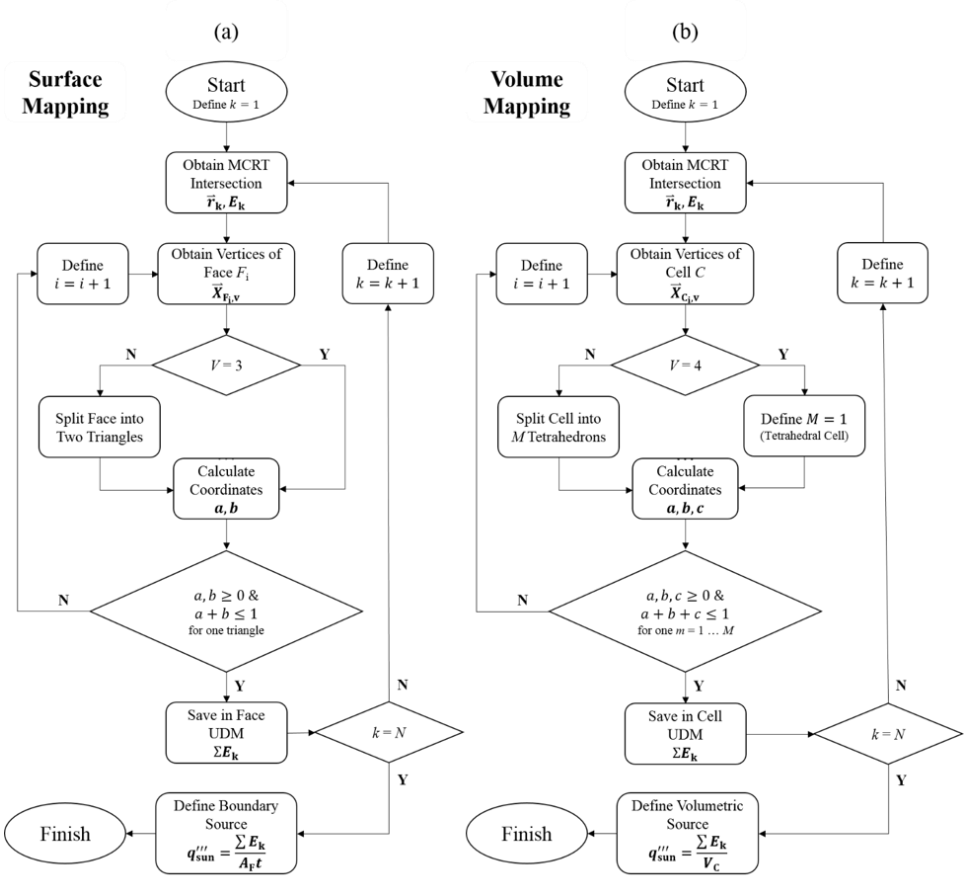

Figure 6.3. Flow charts for mapping of spatially-absorbed, incident irradiation for (a) surface and (b) volume geometries between Monte Carlo ray tracing and computational fluid dynamics modeling domains.

6.3 Modeling

Validation of energy conservation and preservation of spatial variation for the method was performed using the Solar Thermal Inclined Granular-Flow Reactor (STInGR), a 5 kW_{th} windowed solar thermochemical reactor. STInGR was designed for the reduction of redox-active metal oxides heated by input radiation from a HFSS [109],

and the combined HFSS-STInGR system, pictured in Figure 6.4, was modeled using an overlapping scheme. The 142 mm diameter, 5 mm thick quartz window was modeled as a specularly reflecting, non-scattering, participating medium [188]. The empty cavity and conical frustum were modeled as diffusely reflecting alumina surfaces.

The radiative input was modeled using a MCRT of a 6 kW_{th} HFSS comprised of seven Xe arc lamps [197] with the aperture of STInGR aligned to the HFSS focal point and all emitted rays assumed to be within the visible spectrum. The MCRT predicted that 8.77 kW_{th} of radiation was absorbed by STINGR surfaces or within the quartz window. The ray intersections from the MCRT were mapped to a CFD mesh produced in ANSYS Mesh for CFD models in ANSYS Fluent. The mesh consisted of 59209 unstructured triangular and quadrilateral face elements and 617 unstructured tetrahedral, hexahedral, and prismatic volumetric elements.

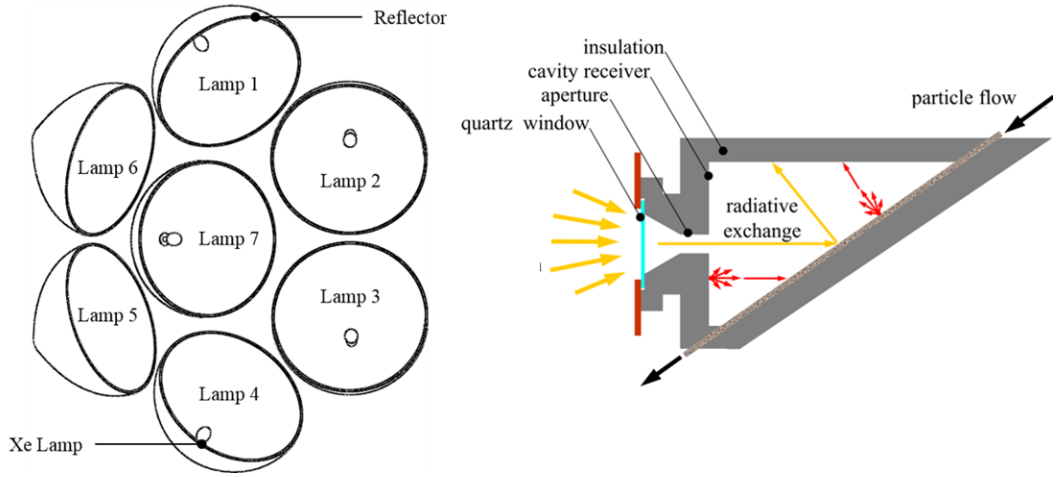

Figure 6.4. Schematic of the 6kW_t high-flux solar simulator with seven Xe arc lamps mounted in truncated ellipsoidal reflectors, with the solar thermochemical inclined granular-flow reactor positioned at the reflector focal point

Three case studies were performed to investigate preservation of spatial variation and energy conservation for direct mapping for three STInGR surfaces: the inclined slope,

ceiling, and conical frustum, labeled as surfaces 1, 2, and 3, respectively. The direct mapping method was compared to the profile interpolation process in ANSYS Fluent. The $\vec{r}_k$ were binned to a structured grid to produce an irradiation flux profile which was interpolated to the CFD mesh [198]. For surface 1, the CFD mesh was structured, so direct mapping would produce identical results to interpolation from an equally-fine MCRT grid. For surface 2, the CFD mesh was unstructured, so direct mapping would provide equal or better preservation of spatial variation and energy conservation. For surface 3, the CFD mesh was unstructured, the surface geometry was complex (conical), and the irradiation gradients were high due to proximity to the HFSS focal point. For this case, deficiencies in the binning, interpolation, and/or mesh resolution could produce significant energy losses.

To quantify spatial accuracy, MCRT surfaces were discretized as uniform, structured grids with approximately the same number of elements as the corresponding meshed CFD surfaces. For each case study, the $\vec{r}_k$ were binned into the corresponding MCRT grid using MATLAB to establish a common standard for comparing preservation of spatial variation. For the profile interpolation method, these gridded data were input to ANSYS Fluent as a profile which was internally interpolated to the CFD mesh. Separately, $\vec{r}_k$ were input to the CFD mesh using the direct mapping method.

To quantitatively compare the energy conservation of both methods, the total energy loss from the MCRT grid to the CFD mesh sources was calculated as:

$$P = \left| \left(\sum_i A_i q''_{sun,i} \right)_{CFD} - \left(\sum_j A_j q''_{sun,j} \right)_{MCRT} \right| \tag{6.12}$$

where *i* and *j* are the indices of CFD mesh and MCRT grid elements, respectively. To quantitatively compare the spatial accuracy of both methods, the resulting CFD mesh sources were linearly interpolated to the MCRT grid and the sum of square errors was calculated as:

$$SSE = \sum_{j} \left(q''_{sun,j}\Big|_{CFD} - q''_{sun,j}\Big|_{MCRT} \right)^2 \tag{6.13}$$

For complete energy conservation and preservation of spatial variation, $P \rightarrow 0$ and $SSE \rightarrow 0$, respectively.

A final case study was performed on the solar thermochemical reactor quartz window to demonstrate the application of the direct volumetric mapping algorithm to participating media. As profile interpolation for volumetric sources was not supported in ANSYS Fluent v17.1, the case study was instead compared to a simple, independent nearest-neighbor sorting algorithm.

6.4 Results and Discussion

Side, isometric, and normal views to the solar reactor inclined slope are given in XXa, b, and c, respectively. Each CFD mesh element is colored according to the absorbed irradiation, which was applied in ANSYS Fluent as a boundary source via the direct mapping method.

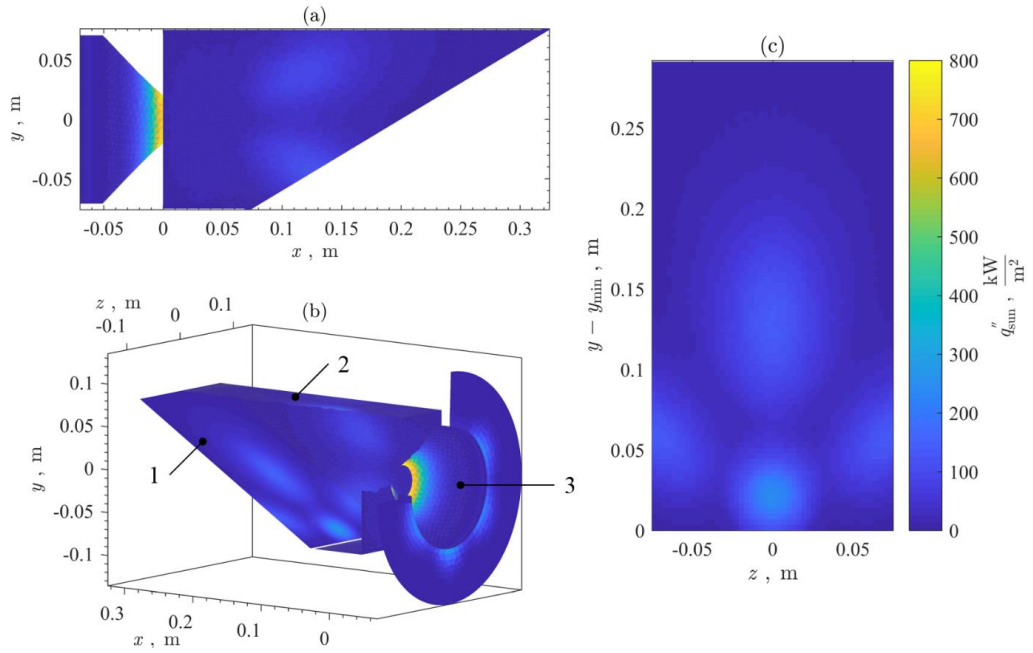

Figure 6.5. Side-view (a), isometric view (b), and normal view to inclined slope (c) of the unstructured computational fluid dynamics mesh for the solar thermochemical inclined granular-flow reactor, with each mesh face colored by the magnitude of mapped absorbed irradiation delivered by a seven-lamp high flux solar simulator using the direct mapping method.

In Figure 6.5a-c, localized regions of highly concentrated absorbed irradiation from individual lamps are evident along the internal cavity and external front face surfaces. Localized regions of high absorbed irradiation were particularly evident along the inclined slope (1), as shown in Figure 6.5c, and would not have been captured by a uniform or spatially-averaged heat flux profile. The total energy mapped to the reactor surfaces was $\sum_i \left(q''_{\text{sun,i}} A_i \right)$ = 8.29 kW_{th}. The total energy mapped to the quartz window was $\sum_i \left(q'''_{\text{sun,i}} V_i \right)$ = 0.48 kW_{th}. A total of 8.77 kW_{th} was mapped to the CFD mesh in ANSYS Fluent, meaning energy was conserved between the MCRT and CFD.

6.4.1 Surface Case Study I: Inclined Slope

The first case study demonstrates a scenario in which the direct mapping method performs identically to previous methods. A normal view of the STInGR cavity inclined slope is given in Figure 6.6, where (a) shows the binned MCRT grid and (b-c) show the mesh elements colored by the magnitude of absorbed irradiation. The slope was discretized as a structured, uniform mesh in the CFD modeling domain with 4250 quadrilateral elements aligned with the MCRT grid. Four local regions of absorbed irradiation were captured in Figure 6.6a-c associated with individual HFSS lamps. Peak fluxes up to 300 $kW_{th} \cdot m^{-2}$ and a total absorbed power of 1.91 kW_{th} were predicted.

In Figure 6.6b and c, nearly identical distributions of absorbed irradiation for the two methods were observed due to effectively exact alignment between MCRT grid and CFD mesh. Both methods achieved complete energy conservation (P = 0 kW_{th}) and high spatial preservation, with SSE_{interp} = 0.003 and SSE_{map} = 0.711, respectively. The spatial errors resulted solely due to differences in numerical precision between C and MATLAB, as no interpolation between modeling domains was required. Therefore, for structured meshes that align exactly to the binned MCRT grid, the direct mapping method is identical to the interpolated profile method.

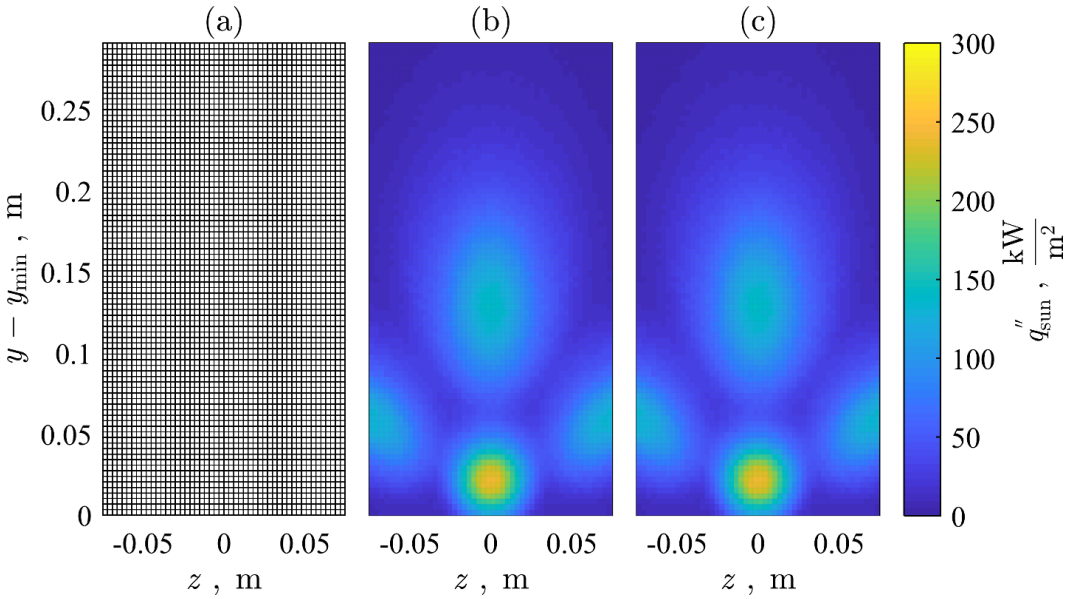

Figure 6.6. Normal view of reactor cavity inclined slope, with (a) the grid used to bin results from a Monte Carlo ray tracing of a seven-lamp high flux solar simulator to an absorbed irradiation profile applied as a boundary source in ANSYS Fluent using (b) the interpolated profile method, compared to (c) the direct mapping method; where each grid/mesh element is colored by the magnitude of absorbed irradiation.

6.4.2 Surface Case Study II: Reactor Ceiling

The second case study demonstrates a scenario in which the direct mapping method is equal to or better than previous methods. A normal view of the meshed STInGR ceiling is given in Figure 6.7, where (a) shows the binned MCRT grid and (b-c) show the mesh elements colored by the magnitude of absorbed irradiation. The ceiling was discretized as an unstructured, non-uniform mesh in the CFD modeling domain with 2864 elements. Three local regions of absorbed irradiation were captured in Figure 6.7a-c, each associated with individual HFSS lamps. Peak fluxes up to 150 $kW_{th} \cdot m^{-2}$ and a total absorbed power of 0.97 kW_{th} were predicted.

In Figure 6.7b, some degradation in spatial accuracy using the profile interpolation method is evident, particularly for F_i with absorbed irradiation of 50–100 $kW_{th} \cdot m^{-2}$. The

elliptical profile was slightly better preserved by direct mapping, as observed in Figure 6.7c. Spatial accuracy and energy conservation were achieved, respectively, to SSE_{map} = 5.8 x10^3 < SSE_{interp} = 7.5x10^3 and P_{map} = 0 < P_{interp} = 0.004 kW_{th}. While both methods approximately preserved the spatial profile shape without significant energy losses, the new method achieved improved spatial accuracy and complete energy conservation.

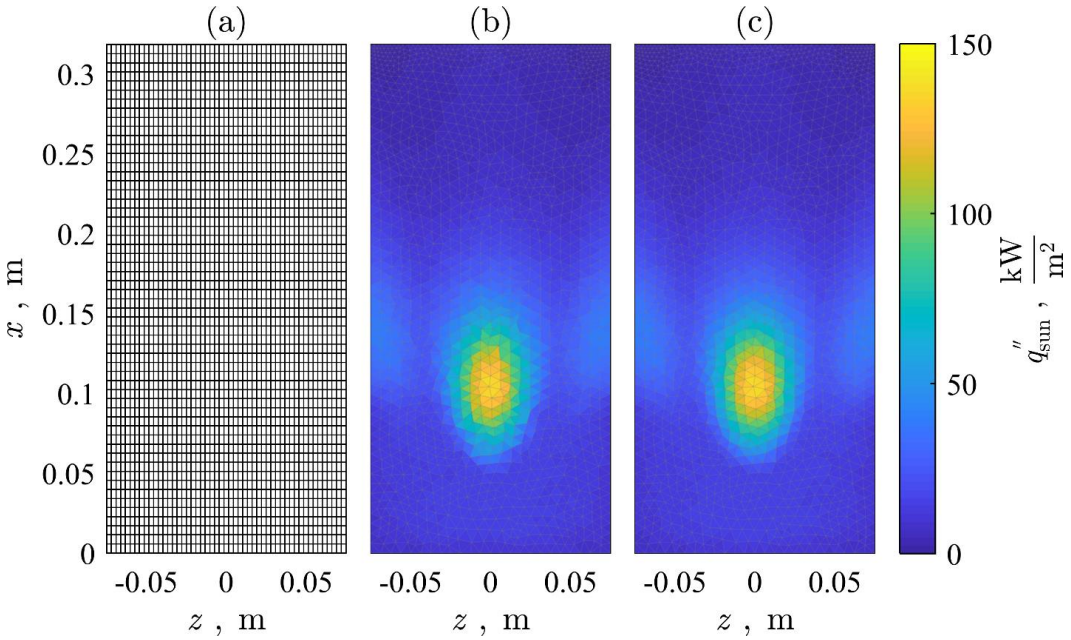

Figure 6.7. Normal view of reactor cavity ceiling, with (a) the grid used to bin results from a Monte Carlo ray tracing of a seven-lamp high flux solar simulator to an absorbed irradiation profile applied as a boundary source in ANSYS Fluent using (b) the interpolated profile method, compared to (c) the direct mapping method; where each grid/mesh element is colored by the magnitude of absorbed irradiation.

6.4.3 Surface Case Study III: Reactor Aperture

The third case study demonstrates a scenario in which the direct mapping method not only preserves spatial accuracy better than previous methods but is critical to prevent significant energy losses. A normal view of the STInGR aperture, a conical frustum shape, is given in Figure 6.8, where (a) shows the binned MCRT grid and (b-c) show the mesh elements colored by the magnitude of absorbed irradiation, with an inset in the bottom right

of (b) presented to show the spatial variation. The frustum was discretized as an unstructured, non-uniform mesh in the CFD modeling domain with 1182 elements. An approximately radially-uniform absorbed irradiation profile is shown in Figure 6.8a-c due a 2.3 kW_{th} spillage of concentrated radiation from the HFSS around the aperture.

While the direct mapping method qualitatively preserved the spatial profile shape slightly better than profile interpolation, there was a mismatch between the locations of the MCRT grid and CFD mesh elements, and between the total surface areas in the MCRT grid (0.022 m^2) and CFD mesh (0.020 m^2), due to approximation of conical surface as planar faces in the mesh. This mismatch prevented a meaningful quantitative *SSE* comparison before and after coupling.

A significantly smaller magnitude of absorbed irradiation was observed in Figure 6.8b compared to Figure 6.8c due to the highly concentrated irradiation in the focal plane. High flux gradients near the aperture led to underestimation during interpolation, which produced a maximum $q''_{sun} = 15 \ll 800$ $kW \cdot m^{-2}$, as shown in the inset. Energy conservation analysis resulted in $P_{map} = 0 < P_{interp} = 2.25$ kW_{th}. This result demonstrated that methods such as profile interpolation may introduce large errors in energy conservation depending on: 1) the irradiation gradient and 2) MCRT grid/CFD mesh resolutions. Direct mapping, however, is robust even for sharp irradiation profiles and/or coarse meshes.

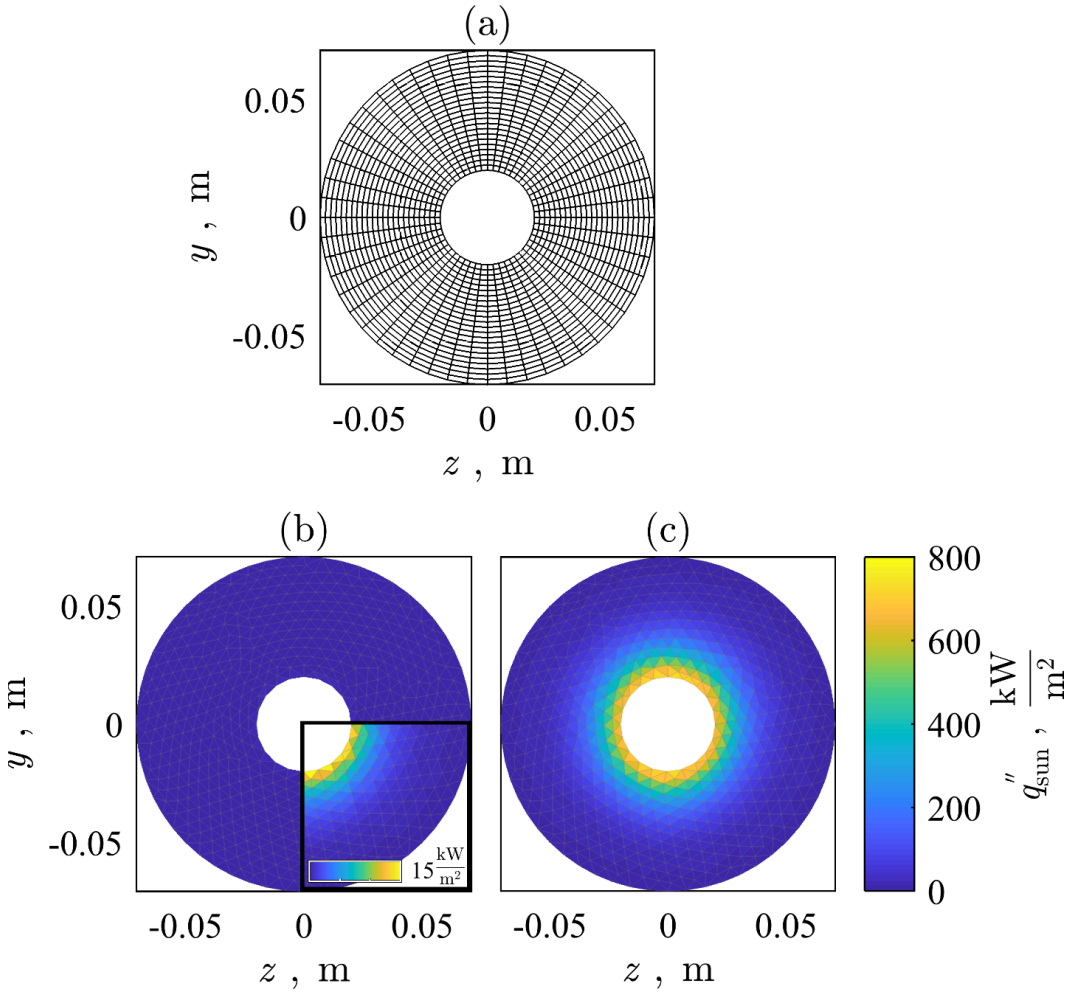

Figure 6.8. Normal view of reactor conical frustum, with (a) the grid used to bin results from a Monte Carlo ray tracing of a seven-lamp high flux solar simulator to an absorbed irradiation profile applied as a boundary source in ANSYS Fluent using (b) the interpolated profile method, compared to (c) the direct mapping method; where each grid/mesh element is colored by the magnitude of absorbed irradiation, and a quarter inset on (b) shows the maximum flux of 15 kW·m^{-2} from the interpolated profile method.

Comparison of mapping methods for the three studies pictured in Figure 6.6-8 demonstrated the inherent energy conservative nature of the direct mapping method, with spatial accuracy dependent upon discretization accuracy of the modeled geometry. The method was also demonstrated to be independent of the non-trivial process of matching gridded MCRT and meshed CFD modeling domains. Direct mapping achieved equivalent

accuracy to the interpolated profile method for aligned MCRT grids/CFD meshes and improved accuracy for misaligned MCRT grids/CFD meshes.

6.4.4 Volumetric Case Study: Quartz Window

An additional case study was performed to demonstrate the direct mapping method for participating media and to show the method's improved performance over the independent nearest-neighbor algorithm. A view of the STInGR window depicting the unstructured CFD mesh cell centroids is given in Figure 6.9a and b. Each cell is colored according to the volumetrically absorbed radiation, which was applied in as a volumetric heat source in ANSYS Fluent using the (a) nearest neighbor and (b) barycentric direct mapping algorithms, respectively.

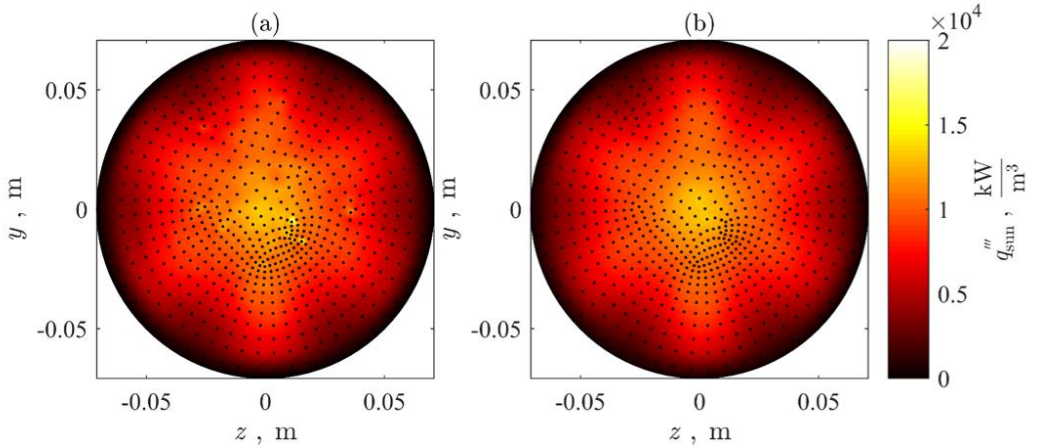

Figure 6.9. Normal view to 5 mm thick quartz window of computational fluid dynamics volumetric cell centroids, with each cell centroid colored by magnitude of mapped volumetric, absorbed irradiation delivered by a seven-lamp high flux solar simulator using (a) nearest-neighbor and (b) barycentric direct mapping methods.

Using both algorithms, the profile of the seven-lamp HFSS, roughly symmetric about (0,0), was visible. In Figure 6.9a, however, localized C_i of high or low q'''_{sun} not present in (b) are evident. The differences were the result of ray misappropriation by the nearest

neighbor algorithm for neighboring cells with significant volume differences. The most prominent example of ray misappropriation in Figure 6.9a occurred at the cell centroid near (0.01,0), producing to a localized hotspot q'''_{sun} of ≈ 1.9 x 10^4 kW/m^3. The centroid and corresponding meshed element is pictured in greater detail in Figure 6.2 as element C_{i+1}. In Figure 6.9b, the profile was smoother as a result of the barycentric mapping algorithm, indicating improved mapping between the MCRT and CFD modeling domains.

Based upon the methodology and various case study observations, the advantages and disadvantages of the method are summarized in the following subsections. Note that all disadvantages are also true for other overlapping modeling domain schemes.

6.4.5 Advantages

1) The method is energy conservative between the MCRT and CFD modeling domains.
2) The method is spatially accurate to within the MCRT and CFD discretization accuracies.
3) The method is compatible with structured and unstructured meshes of arbitrary polygonal or polyhedral construction, for two and three dimensions.
4) The method uses an algorithm that is programmatically simple and may be applied using an external code or directly within ANSYS Fluent via UDFs (see Appendix A).
5) The method requires that the MCRT run only once for a given geometry and radiative conditions, even when performing CFD mesh refinement.

6.4.6 Disadvantages

1) Transient mapping is cumbersome using the method. Such cases occur for overlapping schemes with participating media in the band(s) of the radiative solar input. Non-overlapping domains or MCRT/FV-RTE models with a single computational domain may therefore be more appropriate for media with highly temperature-dependent absorption, transmission, reflection, or scattering.
2) Systematic errors in the absorbed heat flux distribution are introduced by approximating curved geometries from the MCRT model with polygonal elements in the CFD model.

6.5 Conclusions

A method for mapping the results from radiative transport models using Monte Carlo ray-tracing to computational heat transfer models was presented. The direct mapping method allows for the input of two- and three-dimensional radiative absorption on structured or unstructured meshes. The method differs from previous documented attempts in that it may be rapidly implemented and not only maintains energy conservation between the two modeling domains, but also preserves spatial irradiation profiles to within mesh precision.

Energy conservation and preservation of spatial variation by the direct mapping method was demonstrated for a windowed solar thermochemical reactor with input radiation from a high flux solar simulator. The method captured local hotspots from individual lamps and demonstrated that the net energy absorption was equal before and after direct mapping from the Monte Carlo to the CFD mesh. The method was demonstrated to preserve spatial variation and maintain energy conservation as well or

better than previous methods for various complex geometries and mesh types. Most important, the method successfully mapped absorbed irradiation around the reactor aperture while a previous method resulted in energy losses of multiple kW_{th}. Therefore, the direct mapping method is a valuable and, in some scenarios, critical tool for accurately capturing the highly directional and spatial nature of concentrating solar inputs.

CHAPTER 7. 5 KW_{TH} REACTOR DESIGN AND MODELING

7.1 Introduction

A 5 kW_{th} STInGR [109] was designed for operation within a seven-lamp high flux solar simulator. Reactor performance was evaluated using dense, granular flows of aluminum-doped calcium manganite particles. Room-temperature granular flow characteristics of granular media were extracted to investigate mass transfer within STInGR applications. Detailed mass and heat transfer modeling was performed using experimentally determined granular flow characteristics for a range of reactor operating parameters. Modeling was performed in ANSYS Fluent 17.1 to evaluate the performance of candidate granular flows, to capture the final geometry and materials of the laboratory scale reactor within the high-flux solar simulator, and to evaluate the influence of evolved O_2 transport within the reactor on the chemical reduction of the dense granular flow.

7.2 Solar Thermochemical Reactor Design

A 5 kW_{th} scale Solar Thermochemical Inclined Granular-flow Reactor (STInGR) was designed using prior modeling results [109] to achieve thermochemical storage of concentrated irradiation within dense, granular flows. The reactor was designed for evaluating various thermochemical granular media using interchangeable reactor geometries and materials. A Solidworks rendering of the final 5 kW_{th} STInGR design is pictured in Figure 7.1.

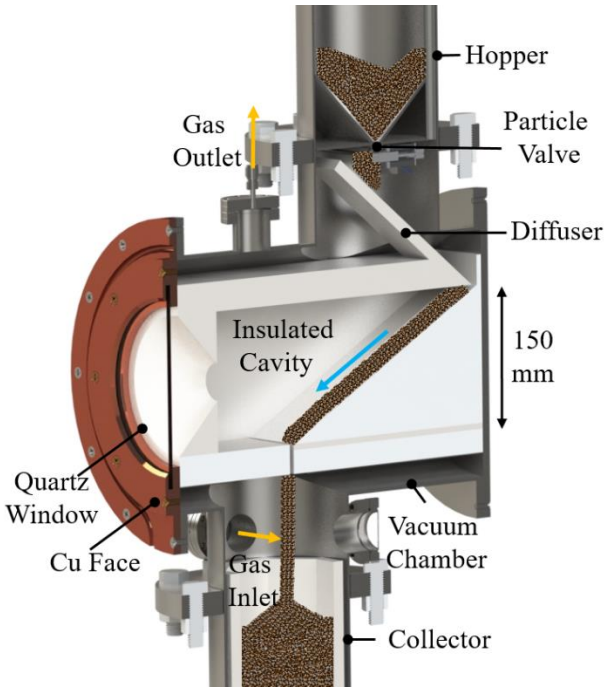

Figure 7.1. Design of the 5 kWth solar thermochemical inclined granular-flow reactor with (a) a Solidworks rendering of the final design and (b) a schematic of the desired flow channel surface roughness promoting a dense, granular flow

The 5 kW_{th} STInGR was designed with an insulated, internal cavity made from high-strength aluminosilicate boards (Zircar Zirconia M35 buster-type insulation). The boards formed a conical aperture, rectangular cavity (150 mm x 150 mm x 0-100 mm), directly-irradiated slope, and granular flow channel. Directly-irradiated cavity surfaces were coated with a high-purity alumina coating (Aremco Pyropaint^{TM} 634-AL) to increase reflectance within the visible spectrum (0 – 4 μm). A uniform surface roughness on a similar order of magnitude to the average particle size was developed along inclined plane flow channels to promote a dense granular flow [116-118], pictured in Figure 7.2.

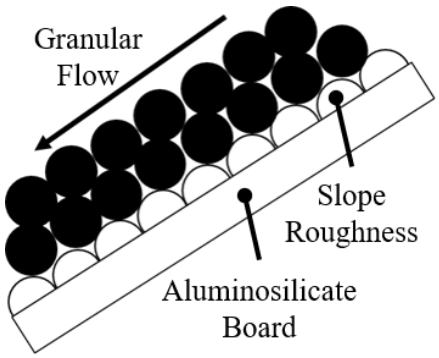

Figure 7.2. Schematic of roughened aluminosilicate board to promote dense, granular flow

The reactor cavity was housed within a cylindrical, stainless steel vacuum chamber. A 5 mm thick, 142 mm diameter quartz window was housed within a water-cooled Cu face. A concentrated, radiative input was introduced through the quartz window while maintaining reduced operating pressures (~ 100 mbar) using a vacuum pump downstream of the gas outlet. Ar sweep gas was introduced to further reduce O_2 partial pressures. Particles were loaded into an upper hopper assembly [199, 200]. Particle mass flow rate was controlled via a coupled orifice plate and solenoid valve [201, 202]. Particles were introduced into the granular flow channel using a diffuser plate, reducing particle kinetic energy and promoting uniform flow depth. A steady, granular flow was achieved within a custom flow channel along the inclined plane and was directly irradiated by a concentrated, radiative input. Incident irradiation was stored within the heat capacitance and endothermicity of the granular flow. High temperature, chemically reduced granular media were recovered in an insulated, cylindrical collector assembly positioned beneath the cavity.

7.3 Granular Media Thermophysical Characterization

The non-stoichiometric reduction and oxidation of perovskite oxide $CaAl_{0.2}Mn_{0.8}O_{3-\delta}$ (CAM28) is given as:

$$CaAl_{0.2}Mn_{0.8}O_{3-\delta'} + \Delta H_{rxn,\delta'\rightarrow\delta} \leftrightarrow CaAl_{0.2}Mn_{0.8}O_{3-\delta} + \frac{\delta - \delta'}{2}O_2 \quad (7.1)$$

where δ is the non-stoichiometric oxygen vacancy concentration or deviation from stoichiometry at a given thermodynamic equilibrium state, which represents the creation of oxygen vacancies within the crystal lattice; and $\Delta H_{rxn,\delta'\rightarrow\delta}$ is the total reaction enthalpy during O vacancy production from δ'→ δ. Thermodynamic properties ($\delta(T,p_{O2})$ and $\Delta H_{rxn,\delta'\rightarrow\delta}$) were extracted by prior studies [44]. Specific heat capacity for CAM28 was predicted using the Dulong-Petits law [203, 204], approximated as 0.918 kJ/kg-K.

Preliminary investigation of the reduction kinetics of a 0.42 g, 2 mm thick sample of high-purity CAM28 particles was performed using the Upward Flow Reactor (UFR) in the HFSS for repeated redox cycling [108]. High-purity CAM28 particles were synthesized in prior studies [44]. After an initial, UFR break-in cycle to remove impurities, 10 subsequent UFR cycles were performed and the rate of O vacancy production during reduction was determined from temporally monitored $\partial\delta/\partial t$ measurements of evolved O_2 [205]. Dispersion corrected temporal measurements of $\partial\delta/\partial t$ for cycles 1, 5, and 10 are given in Figure 7.3, where t = 0 s was selected once temporal O_2 levels exceeded the average baseline value prior to lamp ignition.

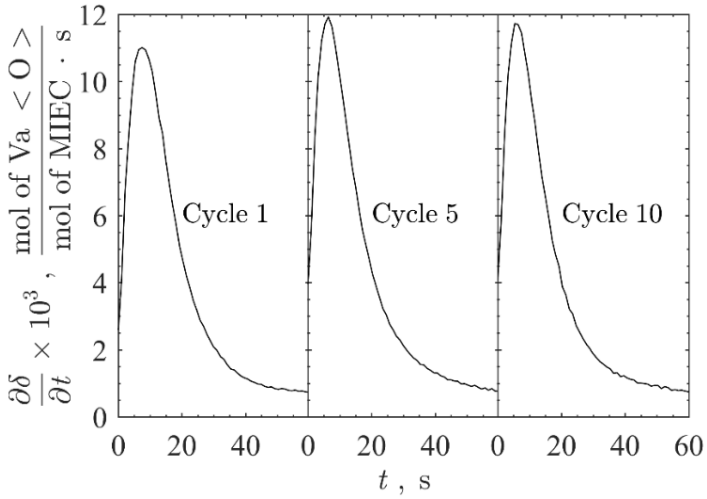

Figure 7.3. Temporal measurements of the rate of O vacany production during reduction of a 0.42 g CaAl0.2Mn0.8O3-δ in the upward flow reactor for cycle 1, 5, and 10.

In Figure 7.3, initial rapid $\partial\delta/\partial t$ was observed with a repeatable peak between $5 < t < 7$ s for all cycles. After the peak, a gradual decrease in $\partial\delta/\partial t$ was observed with an asymptotic tail of $\partial\delta/\partial t \rightarrow 0$. The initial, rapid $\partial\delta/\partial t$ is a result of the sample undergoing rapid heating rates (>50 K/s) at the directly irradiated free surface. The maximum peak and asymptotic tail of $\partial\delta/\partial t$ are a result of absorbed irradiation being transferred through the bed depth through combined conduction and inter-particle radiative exchange. This observed behavior and rapid $\partial\delta/\partial t$ suggests the thermal reduction of CAM28 particle beds is heat-transfer limited rather than kinetically limited. Reduction of a thin, dense granular flow would likely exhibit similar behavior if exposed to similar rapid heating conditions in a HFSS.

7.4 Steady Granular Flow Characterization

Granular flow characterization experiments were performed using bulk, spray-dried aluminum-doped calcium manganite (CAM) particles produced by Coorstek with $\bar{d}_p$ = 45 μm, determined via scanning electron microscopy. CAM particles, and flows were

compared to Accucast ID50 (ID50) particles produced by CarboCast Ceramics with $\bar{d}_p$ = 280 µm [206]. ID50 is a current state-of-the-art inert, sensible storage granular media used in CSP applications. Optical microscopy images (Leica DVM 6 Optical Microscope) are given in Figure 7.4 with (a) CAM and (b) ID50 particles.

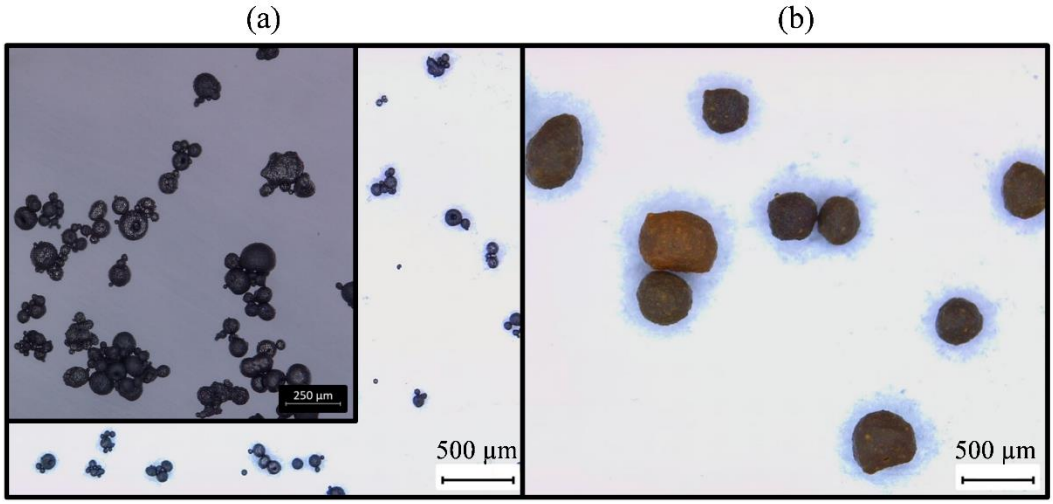

Figure 7.4. Optical microscopy images of (a) spray-dried spray-dried calcium manganites and (b) Accucast ID50 particles

In Figure 7.4a, individual CAM particles appear highly spherical and are clustered into small agglomerates composed of a large particle surrounded by smaller, satellite particles. Additionally, the surfaces of the CAM particles appear more fibrous than the surface of the ID50 particles, which may increase inter-particle cohesion for the CAM particles. In Figure 7.4b, no inter-particle cohesion is observed in the ID50 particles. Increased inter-particle cohesion is expected for granular powders 10 µm < d < 100 µm and may occur for granular solids 100 µm < d < 1000 µm if a high percentage of fines are present [182].

7.4.1 Experimental method

The flow-line equation [118, 131] is used to capture frictional interactions between a granular media and roughened slope pair, given as:

$$\tan\left(\theta_{\text{slope}}\right) = \tan\left(\theta_{\text{min}}\right) + \left(\tan\left(\theta_{\text{max}}\right) - \tan\left(\theta_{\text{min}}\right)\right) \cdot \frac{1}{\bar{h}_{\text{stop}} / L_{\text{o}} + 1} \tag{7.2}$$

where θ_{slope} is the slope inclination angle; θ_{min} is the minimum slope inclination; θ_{max} is the maximum slope inclination angle; $\bar{h}_{\text{stop}}$ is the depth of the residual particle layer deposited onto a slope after a steady flow is halted; and L_{o} is the characteristic flow depth.

The characteristic velocity scaling relationship used to capture granular flow velocities [118, 129], given as:

$$Fr_i = \beta_i \frac{\bar{h}_{\text{flow}}}{\bar{h}_{\text{stop}}} + \gamma_i \tag{7.3}$$

where Fr is the flow Froude number $\bar{u}_i / \sqrt{g\bar{h}_{\text{flow}}}$;is the granular flow characteristic velocity; g is gravitational acceleration; $\bar{h}_{\text{flow}}$ is the average flow height; β_i and γ_{i} are linear fitting coefficients; and i is an indicator of bulk flow or free-surface flow scaling laws. The extracted characteristic velocities include the depth-averaged characteristic bulk flow velocity [168] and the temporally-averaged free-surface velocity given, respectively, as:

$$\bar{u}_{\text{bulk}} = \frac{\dot{m}_{\text{flow}}}{\rho_{\text{bulk}} w \bar{h}_{\text{flow}}} \tag{7.4}$$

$$\bar{u}_{\text{fs}} = \frac{\int_0^t \left(\int_{A_{\text{fs}}} u_{\text{fs}} dA \right) dt}{t \cdot A_{\text{fs}}} \tag{7.5}$$

where $\dot{m}_{flow}$ is the prescribed mass flow rate; ρ_{bulk} is the bulk flow density determined from a trapped portion of the steady flow $m_{trap}/\left(A\cdot\bar{h}_{flow}\right)$ within area A [129]; w is the flow width; u_{fs} is the free surface velocity profile; and A_{fs} is the free surface area along which a steady flow was achieved. Given a granular material and roughened slope pair, the bulk, granular flow behavior can be predicted and modeled using the extracted flow characteristics: θ_{min} , θ_{max}, L_o, β_i, and γ_i. Flow characterization was performed using an experimental tilt-flow-rig, pictured schematically in Figure 7.5.

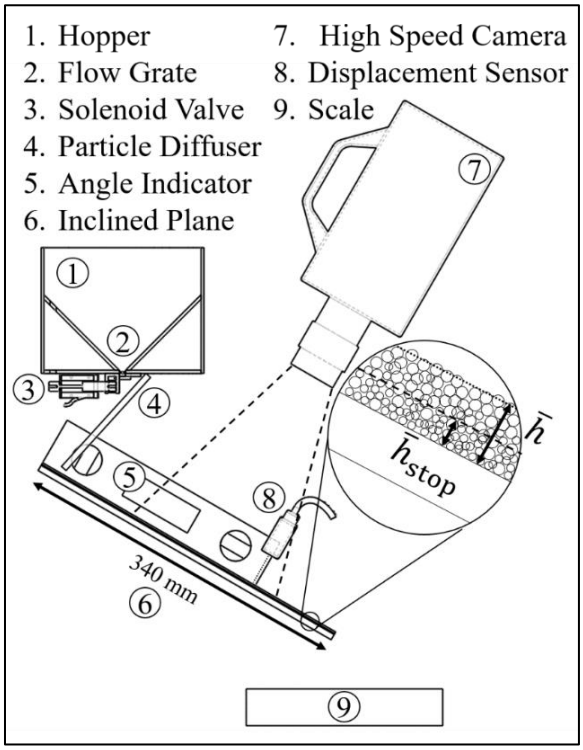

Figure 7.5. Schematic of the tilt-flow rig used for bulk, granular flow characterization

The tilt-flow-rig was composed of a 340 mm long, 150 mm wide interchangeable slope of similar materials, geometry, and flow introduction method as the 5 kW_{th} STInGR for a given granular media and slope pair. A nearly-uniform slope roughness was produced for CAM using sprayed, high purity alumina coating and for ID50 by securing a layer of

particles to the aluminosilicate board using high purity alumina coating. The θ_{slope} was measured using an angle indicator (Husky THD5403). The free surface velocity profile is extracted using a high speed camera (Photron SA3) and particle image velocimetry (PIV) techniques [207]. A laser displacement sensor (Keyence IL-030, IL-1000) was used to determine flow and residual particle depth along the slope. The $\dot{m}_{flow}$ was recorded at the particle flow outlet using a scale (OHAUS Ranger 3000). Two $\dot{m}_{flow}$ levels were selected iteratively per granular media investigated. The lower was selected to achieve $\bar{h}_{flow}/\bar{h}_{stop} > 1.2$ over all θ_{slope}'s where steady flow was observed, as velocity scaling arguments are less reliable as $\bar{h}_{flow}/\bar{h}_{stop} \rightarrow 1$ [118]. The upper $\dot{m}_{flow}$ is approximately twice the lower $\dot{m}_{flow}$. Prior to particle flow, static effects were reduced by passing particles through an electrically grounded sieve, and humidity effects were reduced by storing particles in a cool, dry space within re-sealable 5-gallon drums.

A steady, dense granular flow is developed between 100 – 200 mm downstream from particle introduction for the θ_{slope}'s investigated. For a given θ_{slope}, $\bar{h}_{flow}$ was determined from laser displacement measurements at four equidistant measurement positions across the flow width, with three replicate flows performed per measurement position. The free surface velocity profile was extracted using the high-speed camera at 500 fps and 1024 x 1024 pixel resolution and PIV post-processing tool PIVLab [208]. A residual particle layer was deposited along the slope by sudden closure of the solenoid knife valve during a steady flow. For a given θ_{slope}, the $\bar{h}_{stop}$ was determined from laser displacement measurements at four equidistant measurement locations across the flow

width, with three replicate residual layers produced per measurement position. Measurements were repeated for various θ_{slope}'s where steady flow behavior was observed.

$\boldsymbol{\rho}_{bulk}$ was determined from a series of steady flows between $29° < \theta_{slope} < 35°$ by trapping particles within a known cross-sectional area [129] during steady flow. Trapped particle mass was recorded using a mass balance (Mettler-Toledo ML54) from three repeated measurements per θ_{slope}. $\boldsymbol{\rho}_{bulk}$ was assumed constant across all θ_{slope}'s for a steady flow [129, 168].

Weighted non-linear regression (Alper and Gelb 1990) was used to fit data to the dimensionless steady flow characterization expressions using the least squares criterion for best fit by minimizing chi-squared using a multidimensional unconstrained non-linear minimization algorithm (Nelder-Mead), represented generically as:

$$\chi^2_{\min} = \sum_j \left(\frac{F_j}{\sigma_j} \right)^2 \tag{7.6}$$

where F is a function of measured properties and values that are initially unknown, represented as:

$$F_j = f\left(q_{1j}, \ldots, q_{nj}; \beta_1, \ldots, \beta_r\right) = 0 \tag{7.7}$$

where q denotes n measurands assumed as known, and β represents r fitting parameters assumed initially as unknown. The standard error was estimated as:

$$\sigma_j^2 = \sum_{i=1}^{n} \left(\frac{\partial F_j}{\partial q_{ij}} \right)^2 \sigma_{ij}^2 \tag{7.8}$$

where σ_{ij} represents the experimental uncertainty of the parameter. Ninety-five percent confidence limits for the β's were estimated using Monte Carlo analyses (Alper and Gelb, 1990) with greater than 600 iterations by stochastically varying σ_{ij} 's according to a Gaussian (normal) probability distribution function (pdf) and a uniform pdf for frequentist and Bayesian errors, respectively (Gleser, 1998). The number of iterations were determined once the computed standard deviation of β's varied less than 5% between increased iterations [209].

7.4.2 Experimental results

The prescribed $\dot{m}_{flow}$ and extracted ρ_{bulk} from flow characterization experiments are given in Table 1 with 95% confidence intervals.

Table 7.1. Prescribed inclined flow mass flow rates and extracted steady flow density with 95% confidence intervals for aluminum-doped calcium manganite and Accucast ID50 granular flows

Material	$\dot{m}_{flow}$, g/min	ρ_{bulk} , kg/m^3
CAM	230.1 ± 5 , 510.4 ± 6	1867.8 ± 104.5
ID50	480.2 ± 5 , 821.2 ± 12	1838.5 ± 83.8

The particle density of Accucast ID50 has been well documented as 3300 kg/m^3 [206]. Based on the 95% confidence interval of ρ_{bulk}, the volume fraction (ρ_{bulk} /ρ) range for the Accucast ID50 flows are within 0.53 – 0.58, with mean value of 0.56. This matched well with granular flows of glass spheres with volume fraction range between 0.56 – 0.62, with mean value of 0.59 [129]. The volume fraction of the CAM28 particles was assumed to range 0.54 – 0.66, with mean value 0.6 [166, 168].

Extracted granular flow characteristics of the CAM28 and ID50 are given in Table 7.2 for the flow-line equation, bulk velocity scaling argument, and free-surface velocity scaling argument with calculated 95% confidence intervals.

Table 7.2. Empirically determined granular flow characteristics with 95 % confidence intervals for aluminum-doped calcium manganite and Accucast ID50 granular materials

Material	Flow Line Properties			Bulk Flow Properties		Free Surface Flow Properties	
	θ_{min}	θ_{max}	$L_o / \bar{d}_p$	β_{bulk}	γ_{bulk}	β_{fs}	γ_{fs}
CAM	27.3 ± 1.0	41.2 ± 4.7	2.5 ± 1.3	0.25 ± 0.03	0.12 ± 0.04	0.37 ± 0.02	0.19 ± 0.05
ID50	26.2 ± 0.5	47.6 ± 3.5	0.9 ± 0.3	0.37 ± 0.04	0.29 ± 0.04	0.68 ± 0.05	0.51 ± 0.1

Experimental results for bulk flow characteristics are given in Figure 7.6 including (a) $\bar{h}_{stop} / \bar{d}_p$ as a function of θ_{slope} for CAM and ID50 particles and Fr_{bulk} as functions of $\bar{h}_{flow} / \bar{h}_{stop}$ for (b) ID50 and (c) CAM particles. Fitted steady granular flow relationships are compared to fitted literature relationships for glass spheres and sand [129, 132].

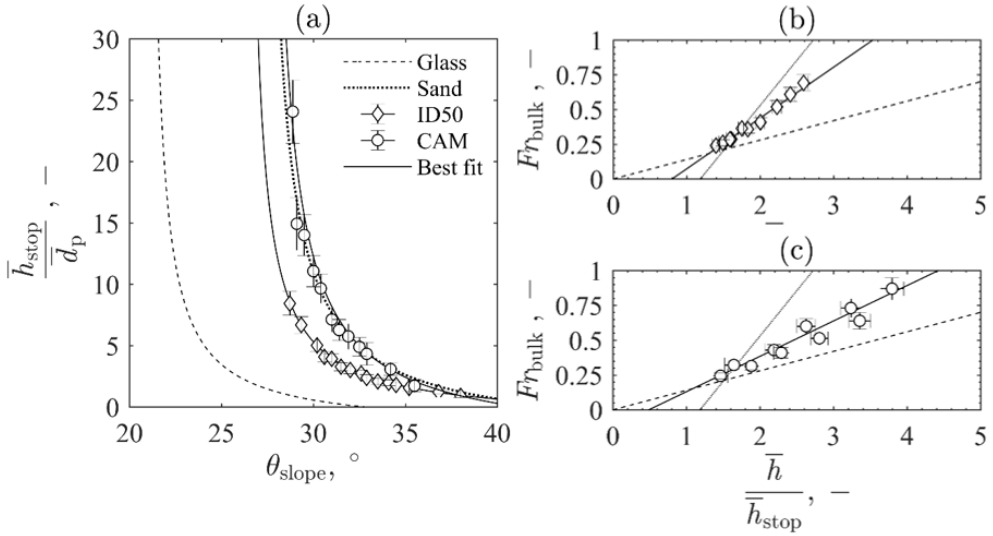

Figure 7.6. Empirically determined bulk granular flow behavior for (a) dimensionless, residual flow height as a function of inclination angle for spray-dried calcium manganites and Accucast ID50 particles and dimensionless bulk flow velocity as functions of

dimensionless flow height for (b) ID50 and (c) CAM particles compared to literature values for uniform, glass spheres and sand particles

In Figure 7.6a, the expected logarithmic increase in $\bar{h}_{stop} / \bar{d}_{p}$ was observed as $\theta \rightarrow \theta_{min}$. The logarithmic increase occurred as particle / slope and particle / particle frictional effects increased relative to the decreasing gravitational shear imparted on the flow for decreasing θ_{slope}. From Figure 7.6a, the CAM and ID50 particles exhibit similar frictional qualities to sand particles, likely due to varying particle size and shape. The greater magnitude of $\bar{h}_{stop} / \bar{d}_{p}$ for CAM particles than ID50 particles over similar θ_{slope}'s was due to increased frictional effects from rough particle surfaces and increased inter-particle cohesive behavior. For both CAM and ID50, $\theta_{max} > 45°$ was observed within the 95% confidence interval due to the influence of particle size segregation, where larger particles migrate towards the flow free surface while smaller particles migrate towards the inclined plane during steady flows [210-213].. Thus, particle fines remain trapped along the roughened incline plane for greater θ_{slope}'s. $\theta_{max} > 45°$ was also observed in prior studies [118]

In Figure 7.6 b and c, both the CAM and ID50 Fr_{bulk} increase linearly with $\bar{h}_{flow} / \bar{h}_{stop}$ and fall within fitted trends for the steady flow behavior of sand and glass spheres. The fitted $\beta_{bulk,CAM} < \beta_{bulk,ID50}$, indicating that a smaller increase in bulk, granular flow momentum with respect to the increased flow weight is required to achieve a similar change in steady flow states $\Delta\left(\bar{h}_{flow} / \bar{h}_{stop}\right)$. From optical microscopy, the ID50 particles were noticeably less spherical than the CAM particles. Similar bulk velocity scaling

behavior was observed between glass spheres and non-spherical sand particles, where $\beta_{glass} < \beta_{sand}$.

The free surface flow behavior of the dense, granular flows are given in Figure 7.7 including (a) Fr_{fs} as a function of $\bar{h}_{flow}/\bar{h}_{stop}$ for CAM and ID50 particles and (b) a representative extracted free-surface velocity profile of CAM particles at = 230 g/min and θ_{slope}= 29.6°.

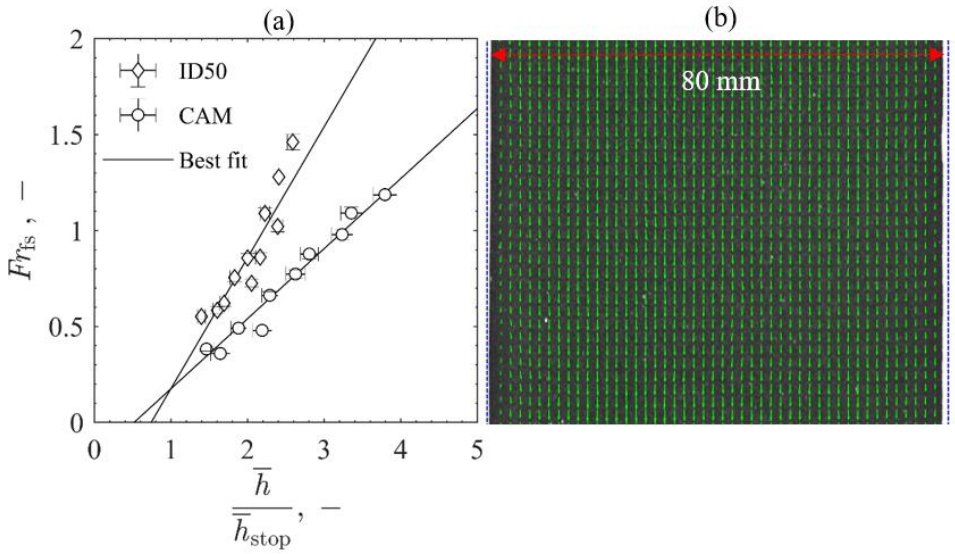

Figure 7.7. Free-surface velocity characteristics including (a) empirically-determined dimensionless area-averaged free surface flow velocity as functions of dimensionless flow height for spray-dried aluminum doped calcium manganite and Accucast ID50 particles and (b) representative extracted free-surface velocity profile of spray-dried aluminum-doped calcium manganite particles flowing at 230 g/min for an inclination angle of 29.6°.

In Figure 7.7a, Fr_{fs} increased linearly with $\bar{h}_{flow}/\bar{h}_{stop}$, but at a significantly higher rate than the Fr_{bulk} as the $\Delta\bar{u}_{fs} > \Delta\bar{u}_{bulk}$ for a similar $\Delta\left(\bar{h}_{flow}/\bar{h}_{stop}\right)$. In Figure 7.7b, an extracted velocity vector field is plotted across the flow free surface. The frictional influence of the sidewalls on the granular flow resulted in reduced velocity vectors near

the flow edges. In Figure 7.7b, local regions of limited flow acceleration and deceleration were observed as a result of local variations in surface roughness.

Significance of fitted regression was evaluated using the *F* statistic for regression for all fitted expressions, given in Table 7.3. Evidence suggested that each fitted expression was statistically significant ($F_o > F_{v1,v2,0.05}$) within 95% confidence.

Table 7.3. Significance of regression for fitted bulk granular flow relationships evaluated using the F-statistic value of regression and the root mean square error for both CAM and ID50 particles

Material	$\bar{h}_{stop} / \bar{d}_p$		Fr_{bulk}		Fr_{fs}	
	F-statistic	p-value	*F*-statistic	p-value	*F*-statistic	p-value
CAM	67 > 3.89 ($F_{2,12,0.05}$)	< 1e-5	110 > 5.32 ($F_{1,8,0.05}$)	< 1e-5	209 > 5.32 ($F_{1,8,0.05}$)	<1e-5
ID50	1553 > 4.26 ($F_{2,9,0.05}$)	< 1e-5	357 > 5.12 ($F_{1,9,0.05}$)	< 1e-5	35 > 5.12 ($F_{1,9,0.05}$)	0.002

Resulting fitted, bulk granular flow relationships were evaluated with the goodness of fit statistic root-mean square error (RMSE), given in Table 7.4.

Table 7.4. Goodness of fit statistic for fitted granular flow relationships for both CAM and ID50 particles

Material	$\bar{h}_{stop} / \bar{d}_p$	Fr_{bulk}	Fr_{fs}
	RMSE	RMSE	RMSE
CAM	1.61	0.05	0.05
ID50	0.13	0.02	0.11

The fitted, bulk granular flow relationships were used to predict granular flows experienced in the 5 kW_{th} STInGR during operation in the HFSS assuming the granular flow achieved steady flow conditions immediately upon introduction. This assumption led to an under-prediction of the average particle residence time in subsequent heat and mass transfer modeling as a granular flow would need to accelerate along the slope to achieve steady flow conditions after introduction.

7.5 Heat and Mass Transfer Modeling

Steady-state heat and mass transfer modeling was performed to evaluate the 5 kW_{th} STInGR performance using dense, granular flows of spray-dried CAM as a TCES material using computational fluid dynamics (CFD) software ANSYS FLUENT 17.1 [214]. The granular flow was modeled using a uniform, structured CFD mesh aligned with the flow direction while other regions were modeled using an unstructured CFD mesh. Second-order upwind discretization methods were employed to capture advective transport in the momentum, species, and energy equations. Body-force weighted discretization methods were used in solving for pressure to capture transport of evolved O_2 from the granular flow free surface. A least-squares, cell-based gradient method was used in calculating interfacial element scalar values. Inter-cavity gas flow was modeled as incompressible and laminar and solved using the semi-implicit method for pressure linked equations scheme for pressure-velocity coupling [89, 108]. Granular flow was modeled as a mixture of granular material, evolved O_2, and Ar interstitial gases. Inter-cavity gases were modeled as a mixture of O_2 and Ar. Thermodynamic and thermophysical properties of the CAM were assumed equivalent to high-purity CAM28.

7.5.1 Granular flow velocity profile

A two-dimensional constitutive relationship was used to model both collisional and frictional momentum transfer within dense granular flows [215, 216] assuming the interstitial gas has no effect on the bulk flow [130], given as:

$$\sigma_{xz} = \kappa\left(\frac{\partial u_x}{\partial z}\right)^2 + \nu\left(\frac{\partial u_x}{\partial z}\right) \tag{7.9}$$

where σ_{xz} is the net shear stress during flow conditions; $\kappa\left(\partial u/\partial z\right)^2$ is the Bagnold scaling relationship capturing the influence of binary collisions on momentum transfer; $\nu\left(\partial u/\partial z\right)$ is an elastic scaling relationship capturing the influence of long-lived particle contacts (i.e. friction) on momentum transfer; $\left(\partial u/\partial z\right)$ is the shear rate within the granular flow; and κ and ν are proportionality constants which capture relative importance between the momentum transfer mechanisms and are determined for a particular flow configuration. From the constitutive relationship and assuming negligible sidewall effects, a unidirectional velocity profile for cohesive CAM granular flow was derived [216], given as:

$$u_{\mathrm{CAM}}\left(z\right)\begin{cases}\dfrac{2}{3c\sqrt{\kappa}}\left\{\left(\left(\dfrac{\nu}{2\kappa}\right)^2+c\bar{h}_{\mathrm{flow}}\right)^{3/2}-\left[\left(\left(\dfrac{\nu}{2\kappa}\right)^2+c\left(\bar{h}_{\mathrm{flow}}-z\right)\right)^{3/2}\right]\right\} \\ \qquad -\left(\dfrac{\nu}{2\kappa}\right)z\ ,\ z<h_{\mathrm{plug}} \\ \bar{u}_{\mathrm{fs}}\ ,\ z\geq h_{\mathrm{plug}}\end{cases} \tag{7.10}$$

where $c=\rho_{\mathrm{bulk}}\cdot g\cdot\sin(\theta_{\mathrm{slope}})$; h_{plug} is the thickness of an upper plug flow region near the free surface; and z represents the flow depth position. Similar velocity profiles with two, distinct regions of flow behavior have been observed for granular flows of bi-disperse particle sizes [213], for particle flows with extended particle chain contacts [155], and for avalanches [217]. Unknown parameters were fit by minimizing error with respect to $\bar{u}_{\mathrm{bulk}}$ and $\left(\partial u/\partial z\right)\big|_{z=h_{\mathrm{plug}}}\rightarrow 0$ with a known $\bar{u}_{\mathrm{fs}}$ for a given flow configuration.

A unidirectional, velocity profile was derived for the ID50 particles assuming elastic momentum transfer was dominated by interlocking particle chains [155] and is

nearly linear, as is observed for thin, granular flows [166]. The unknown parameter was fit by minimizing error with respect to $\bar{u}_{bulk}$ for a given flow configuration. The fitted velocity profile predicted $\bar{u}_{fs}$ to within 10% of measured values for all investigated flow configurations.

The modeled, granular flow behavior extracted from empirical bulk flow characteristics for CAM and ID50 particles are given in Figure 7.8, including (a) $\bar{u}_{bulk}$ as a function of $\bar{h}_{flow}/\bar{h}_{stop}$ for θ_{slope} = 31, 35˚ with comparisons for $\dot{m}_{flow}$ = 230, 300 g/min and (b) unidirectional, granular flow velocity profiles through the dimensionless flow depth for $\dot{m}_{flow}$ = 230 g/min and θ_{slope} = 31, 35°.

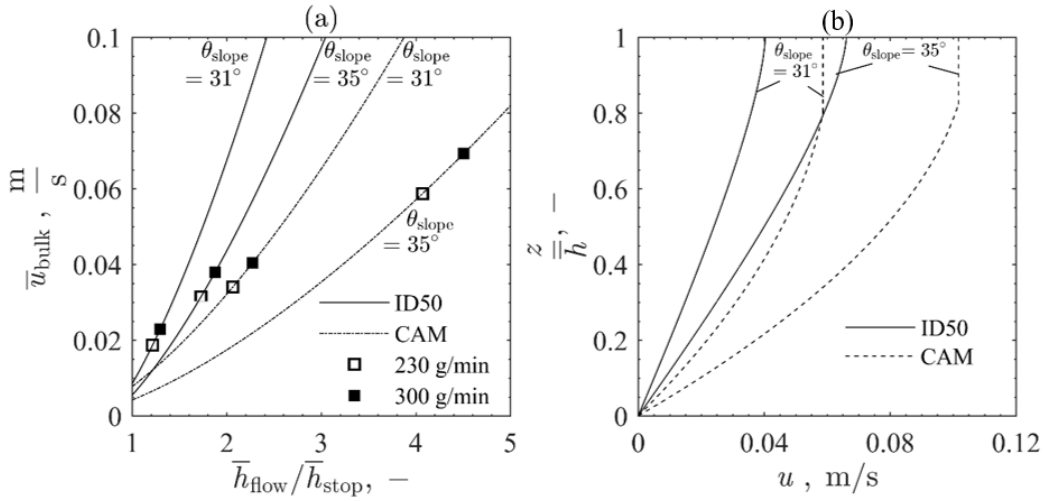

Figure 7.8. Modeled, granular flow behavior extracted from empirical bulk flow characteristics for spray-dried aluminum doped calcium manganites and Accucast ID50 particles including (a) average bulk flow velocity as a function of flow height deviation from frictional equilibrium for inclination angles of 31, 35˚ and mass flow rates of 230, 300 g/min and (b) unidirectional, granular flow velocity profiles within dimensionless flow depth for inclination angles of 31, 35 ˚ and mass flow rate of 230 g/min.

In Figure 7.8a, $\bar{u}_{bulk,CAM} > \bar{u}_{bulk,ID50}$ for equivalent θ_{slope} and $\dot{m}_{flow}$ as the magnitude of $\bar{h}_{flow}/\bar{d}_{p}$ is greater for CAM than ID50, resulting in reduced effects of the particle / slope

frictional boundary with respect to shear throughout the bulk flow. In Figure 7.8b, the distinct plug flow region of u_{CAM} and the differences in velocity magnitudes between the CAM and ID50 flows are observed.

7.5.2 Radiative exchange modeling

The 142 mm diameter, 5 mm thick quartz window was modeled as a non-scattering, participating medium [188] with specularly reflecting and refracting surfaces [176]. Intercavity gases were modeled as non-participating. Cavity surfaces were modeled as gray, diffusely reflecting aluminosilicate surfaces coated in high-purity alumina. Additional modeled surfaces include gray, diffusely reflective stainless steel and gray, specularly reflective copper [218] surfaces. The free surface of the granular flow was modeled as optically thick [102], with gray, diffuse radiative properties for a packed bed of CAM particles. Room temperature spectral, hemispherical radiative properties were measured for an opaque, packed bed of CAM particles and for the alumina-coated aluminosilicate boards. Measurements were performed using a coupled monochromator with integrating sphere (0.38-1.8 μm) and Fourier transform infrared spectrometer with integrating sphere (1.8-16 μm) with measurement accuracy of ±0.03 over all wavelengths [219]. Spectral, hemispherical radiative properties for ID50 were extracted from prior studies [220]. Radiative properties were modeled using a gray-band approximation with six modeled bands, given in Table 7.5.

Table 7.5. Band approximated radiative properties used in coupled radiative models of the solar thermochemical inclined granular-flow reactor

Radiative Band (μm)	α_{CAM}	α_{coat}	α_{ID50}	α_{steel}	α_{cu}	n_{quartz}	κ_{quartz}
0 - 1	0.93	0.11	0.92	0.8	0.3	1.5	8.4
1 - 2.25	0.85	0.17	0.88		0.01		
2.25 - 4	0.63	0.72					
4 – 5.8	0.53	0.72				1.8	$\sim 10^8$
5.8 - 8	0.76	0.92					
8 - ∞	0.93	0.89					

A HFSS comprised of seven Xe arc lamps [109, 197] is used to supply the radiative input to the 5 kW_{th} STInGR within 0 – 4 μm, similar to a blackbody emitter at 5800 K [221]. The combined HFSS-STInGR radiative exchange was modeled using 1) Monte Carlo ray tracing (MCRT) [176, 180] to capture highly concentrated, directional radiative inputs from the HFSS, 2) finite volume approximations to the radiative transport equation (FV–RTE) [102, 222] to capture diffuse, re-emission within STInGR, and 3) the Rosseland diffusion approximation [102, 171] to capture particle-to-particle radiative exchange within the dense granular flow using a modified thermal conductivity term [108, 109]. A novel, mapping method is proposed for coupling the MCRT and FV-RTE modeled domains, detailed in Appendix A. The FV-RTE was modeled using the discrete ordinates method [223] with a first-order upwind discretization scheme. Effects of false diffusion common to FV-RTE methods for directional irradiation [105] were reduced by modeling directional radiative HFSS inputs using MCRT and by both CFD and radiative mesh refinement [105].

7.5.3 Conservation of mass and energy

The steady-state, local, volume-averaged mass conservation equation for the intercavity gas flow and granular flow is given as:

$$\nabla \cdot \left(\rho_i \vec{V} \right) = \nabla \cdot D_{\mathrm{m},ij} \rho \nabla \frac{\rho_i}{\rho} + \dot{S}_{\mathrm{m},i} \tag{7.11}$$

where, ρ is the effective mixture density; ρ_i is density of component *i*; $\vec{V}$ is the flow velocity vector; $\dot{S}_{\mathrm{m},i}$ is the volumetric rate of production for component *i*; and $D_{\mathrm{m},ij}$ is the Fick diffusivity of a binary gas mixture (O_2/Ar). $D_{\mathrm{m},ij}$ is modeled as diffusion within a plain medium for the intercavity gas flow [224] and modified for transport within a porous media within the granular flow [225-227], given as:

$$D_{\mathrm{m},ij} = D^{\circ}_{\mathrm{m},ij}, \frac{D^{\circ}_{\mathrm{m},ij}(1 - f_{\mathrm{v}})}{\tau} \tag{7.12}$$

where, $D^{\circ}_{\mathrm{m},ij}$ is the temperature and pressure dependent Fick diffusion coefficient for a binary gas mixture (O_2 / Ar) in plain media calculated from Chapman-Enskog theory [224, 225]; (1-f_{v}) captures the modified cross-sectional area through which gas is diffused in a porous media; f_{v} is the volume fraction of particles within the granular flow; and τ is the tortuosity of gas transport through a bed of overlapping spheres [227]; given as:

$$\tau = 1 - \left(\frac{1}{2} \right) \ln\left(1 - f_{\mathrm{v}}\right) \tag{7.13}$$

Evolved O_2 and consumed CAM were modeled within the granular flow based upon CAM28 reduction δ'→δ and a unidirectional velocity profile, given as:

$$\dot{S}_{\mathrm{m},i} = \frac{\pm\rho_{\mathrm{bulk}}\left(\vec{V}\cdot\vec{A}\right)\left(\frac{M_{\mathrm{O_2}}}{M_{\mathrm{CAM28}}}\right)\left(\frac{\delta-\delta^{'}}{2}\right)}{V} \tag{7.14}$$

where, M is the molar mass of a given component; V is the cell volume; A is the element face area; and ± is for CAM consumption (-) or O_2 evolution (+) within the granular flow.

Steady-state energy conservation in all modeled regions is given as:

$$\nabla\cdot\left(\rho C_p\vec{V}T\right) = \nabla\cdot\left(k_{\mathrm{eff}}\nabla T\right) + \dot{S}_{\mathrm{rxn}} + \dot{S}_R + \dot{S}_{\mathrm{HFSS}} \tag{7.15}$$

where, C_p is the effective mixture specific heat; T is the local temperature; k_{eff} is the effective mixture or solid thermal conductivity; $\dot{S}_\mathrm{R}$ is the volumetric energy source calculated from an internal radiative balance computed via the FV-RTE; $\dot{S}_{\mathrm{HFSS}}$ is the volumetric energy source calculated from absorbed HFSS radiation computed via the MCRT; and $\dot{S}_{\mathrm{rxn}}$ is the volumetric energy sink calculated from the reduction enthalpy of heat-transfer limited CAM and a unidirectional velocity profile within the granular flow given as:

$$\dot{S}_{\mathrm{rxn}} = \frac{\rho_{\mathrm{bulk}}\left(\vec{V}\cdot\vec{A}\right)\Delta H_{\mathrm{rxn},\delta^{'}\rightarrow\delta}}{V} \tag{7.16}$$

Thermophysical properties for inter-cavity gases and granular flow were modeled as homogeneous mixtures of constituent materials. Gaseous thermophysical properties were determined from NIST chemistry webbook [228]. Effective thermal conductivity within the dense granular flow was modeled using the combined Zehner-Bauer-Schlunder porous media thermal conductivity model [173, 229] and the Rosseland diffusion approximation [102] to capture both thermal conductivity of the granular media and inter-

particle radiative exchange [108, 109]. Local thermal equilibrium was assumed for all modeled mixtures and convection within the granular flow voids was neglected.

7.5.4 Modeled parameters and boundary conditions

Based on previous analysis, the highly concentrated irradiation associated with individual lamps produced localized high temperature regions within a dense granular flow of Co_3O_4 / CoO particles [109]. Because spray-dried calcium manganites have been observed to exhibit agglomeration at T > 1173 K [49], the dense, granular flow configurations, cavity geometry, and HFSS lamp conditions were modified to promote uniform heating of the granular flow and bulk granular flow temperatures < 1173 K. The granular flow width was restricted to 80 mm, diverting the granular flow passed regions of highly directional irradiation supplied by two, peripheral HFSS lamps. A cavity depth of 100 mm was also selected to promote diffuse, uniform heating of the granular flow [109]. The top-most HFSS lamp positioned near-normal to the granular flow was not used in the analysis. Major modeled parameters are detailed in Table 7.6.

Table 7.6. Major modeled parameters used in heat and mass transfer modeling of 5 kW_{th} Solar Thermochemical Inclined Granular-Flow Reactor

Parameters	Values
$\dot{Q}_{HFSS}$	4.3 (5 lamp) – 5.2 (6 lamp) kW_{th}
$\dot{m}_{flow}$	230, 300 g/min
w_{cavity}, h_{cavity}	150 mm
l_{cavity}	100 mm
w	80 mm
d_p	45 (CAM), 280 (ID50) μm
ρ_{bulk}	1868 (CAM), 1839 (ID50) kg/m^3
f_v	0.56 – 0.64 (CAM), 0.56 (ID50)
P	90 – 110 mbar
θ_{slope}	31˚, 35˚
k	202.4 (Cu), 0.27 (M35), 1.4 (Quartz), 14.9 (Steel) , 2.0 for T = 1373 K (ID50) [220], $-8.62\text{x}10^{-9}T^3 + 2.08\text{x}10^{-5}T^2 - 1.75\text{x}10^{-2} + 7.28$ for $T \leq 1100$ K (CAM) [230] W/m-K

A schematic of the 5 kW_{th} STInGR modeled domain including callouts for major boundary conditions is pictured in Figure 7.9.

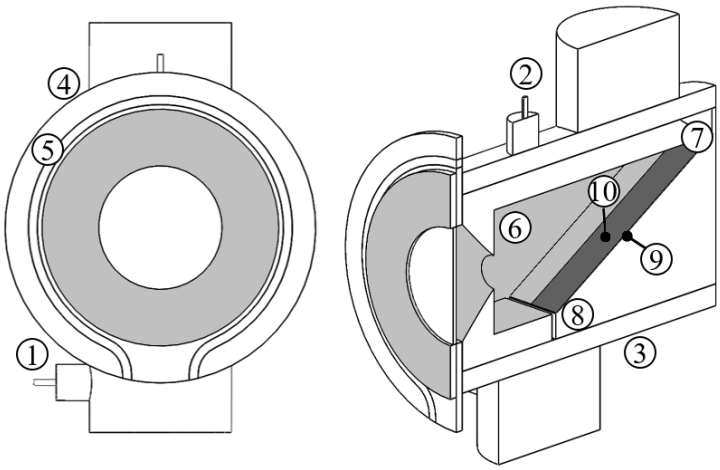

Figure 7.9. Computational fluid dynamics modeling domain for the 5 kWth solar thermochemical inclined granular-flow reactor with labeled major modeled boundary conditions and shaded surfaces indicating directly irradiated reactor surfaces (light gray) and the directly irradiated dense, granular flow (dark gray)

The reactor is operated in environmental conditions h_∞ = 25 W/m^2 , T_∞ = 300 K, and external surface radiative properties α = 0.8. Thin, steel surfaces were modeled

assuming one-dimensional heat transfer with conductive resistance R_{steel} based upon reactor geometry. The major external modeled boundary conditions are detailed in Table 7.7.

Table 7.7. Major modeled boundary conditions for 5 kW_{th} scale solar thermochemical inclined granular flow reactor

No.	Description	Boundary	Material	Modeled Conditions
1	Sweep Gas Inlet	Constant mass flow, ambient temperature	Ar	$\dot{m} = 1.48735 \cdot 10^{-5}$ kg/s $T = 300$ K
2	Gas Outlet	Constant pressure, convective outlet	Ar, O_2	P = 100 mbar
3	Vacuum Chamber Exterior	Energy conservation	Steel / Environment	$q'' = \left[1/R''_{steel} + \left(h_{conv} + h_{rad}\right)\right] \cdot \left(T_{s,i} - T_{\infty,i}\right)$
4	Cu Face Exterior	Energy conservation	Cu / Environment	$q'' = \left(h_{conv} + h_{rad}\right) \cdot \left(T_{s,i} - T_{\infty,i}\right)$
5	Water-cooled Cu Channel	Constant temperature	Cu	T = 300 K

Major internal boundary conditions include directly irradiated cavity surfaces and the granular flow boundaries, detailed in Table 7.8. The radiative exchange boundary conditions include both mapped incident, absorbed irradiation from the HFSS (Chapter 6) and net, internal re-radiative exchange calculated from FV-RTE . The granular flow mixture was introduced with fully oxidized CAM28 particles (δ=0), uniform temperature, composition, and steady, unidirectional velocity profile. The granular flow inlet and free surface interstitial gas composition was defined assuming an ideal-gas mixture. Granular flow inlet and free surface O_2 concentration was modeled as the average O_2 concentration along the free surface within the intercavity gas flow, capturing the influence of inter-cavity O_2 transport on the granular flow reduction. Evolved O_2 diffused through the granular flow free surface was delivered to the intercavity gas flow.

Table 7.8. Major modeled boundary conditions for granular flow within 5 kW_{th} scale solar thermochemical inclined granular flow reactor

No.	Description	Boundary	Material	Modeled Conditions
6	Directly Irradiated Surfaces	Energy conservation	Alumina, Cu faces / Ar,O2	$-k_{n,i}\left.\frac{\partial T}{\partial n}\right\|_{s,i} + q''_{HFSS,i} =$ $h_i\left(T_{s,i} - T_{bulk,i}\right) + q''_{R,i}$
7	Particle Inlet	Constant temperature Constant Mass Flow	Granular flow	T = 300 K $\dot{m}_{flow} = \int \rho u w \, dz$
8	Particle Outlet	Convective outlet	Granular flow	
9	Particle / Insulation Interface	Energy Conservation No penetration	Granular flow / Al_2O_3	$-k_{n,part}\left.\frac{\partial T}{\partial n}\right\|_{s,part} = -k_{n,ins}\left.\frac{\partial T}{\partial n}\right\|_{s,ins}$ $\left.\frac{\partial\left(\rho_i/\rho\right)}{\partial n}\right\|_{s,i} = 0$
10	Particle Free Surface	Energy conservation Mass conservation	Granular flow / O_2, Ar	$-k_{n,i}\left.\frac{\partial T}{\partial n}\right\|_{s,i} + q''_{HFSS,i} =$ $h_i\left(T_{s,i} - T_{\infty,i}\right) + q''_{R,i}$ $\dot{m}''_{O_2,i} = -\rho D_{m,ij}\left.\frac{\partial\left(\rho_{O_2}/\rho\right)}{\partial n}\right\|_{s,i}$

Granular flow performance was evaluated using the mass-flow weighted, average outlet temperature $\bar{T}_{out}$ and stoichiometric deviation $\Delta\bar{\delta}_{out}$, and total efficiency η_{total}, defined as:

$$\bar{T}_{out} = \frac{\int_{out} \rho C_p T u dA}{\dot{m}_{flow,out}\bar{C}_p}, \Delta\bar{\delta}_{out} = \frac{\int_{out} \rho \Delta\delta u dA}{\dot{m}_{flow,out}},$$
$$\eta_{total} = \frac{\left(\int_{out} \rho C_p T u dA - \int_{in} \rho C_p T u dA\right) + \left(\int \dot{S}_{rxn} dV\right)}{\dot{Q}_{HFSS}} \quad (7.17)$$

where $\dot{Q}_{HFSS}$ was determined as the HFSS concentrated irradiation delivered to an aperture of 40 mm diameter at the HFSS focal plane. Granular flow performance was also

evaluated using the storage density rate which compares the quantity and rate of energy storage within a granular flow, defined as:

$$\dot{R} = \frac{\left(\int_{\text{out}} \rho C_{\text{p}} T u dA - \int_{\text{in}} \rho C_{\text{p}} T u dA\right) + \left(\int \dot{S}_{\text{rxn}} dV\right)}{\dot{m}_{\text{flow}} \cdot \bar{t}} \tag{7.18}$$

where $\bar{t}$ is the average residence time of the granular flow. This metric becomes most important when evaluating scaled-up designs and comparing granular media.

7.6 Modeling Results and Discussion

A preliminary investigation was performed on the general design space varying major experimental parameters: $\dot{m}_{\text{flow}}$ = 230, 300 g/min, θ_{slope} = 31, 35°, and $\dot{Q}_{\text{HFSS}}$ = 4.3, 5.2 kW_{th}. The $\dot{Q}_{\text{HFSS}}$ = 4.3, and 5.2 kW_{th} were the power delivered from the HFSS to a calorimeter positioned at the focal plane for a combination of 5 and 6 lamps, respectively.

7.6.1 Investigation of Design Space

Granular flow performance for varying design space parameters are included in Table 7.9

Table 7.9. Reactor performance evaluated for varying design space parameters

$\dot{m}_{\text{flow}}$, g/min	θ_{slope}, °	$\dot{Q}_{\text{HFSS}}$, kW_{th}	$\bar{h}_{\text{flow}}$, mm	$\bar{t}$, s	ΔT_{out}, K	$\bar{T}_{\text{out}}$, K	$\Delta\bar{\delta}_{\text{out}}$	η_{total}
230	31	5.2 (6 lamp)	0.75	8.56	138	1158	0.076	0.628
230	31	4.3 (5 lamp)	0.75	8.56	197	1005	0.026	0.594
230	35	5.2 (6 lamp)	0.44	4.45	120	1165	0.078	0.635
230	35	4.3 (5 lamp)	0.44	4.45	172	1007	0.027	0.598
300	31	5.2 (6 lamp)	0.83	7.21	198	1011	0.024	0.649
300	31	4.3 (5 lamp)	0.83	7.21	279	866	0.001	0.606
300	35	5.2 (6 lamp)	0.48	3.77	175	1017	0.028	0.657
300	35	4.3 (5 lamp)	0.48	3.77	255	874	0.003	0.617

The competing effects of $\bar{t}$ and $\bar{h}_{\text{flow}}$ most impacted the granular flow performance within the 5 kW_{th} STInGR, emphasizing the sensitivity of the system to granular flow characteristics. For dense, granular flows the increased $\bar{t}$ occurred at the expense of an increased $\bar{h}_{\text{flow}}$, resulting in greater conductive resistance through the flow. In Table 8, an increased θ_{slope} with other parameters held fixed resulted in decreased ΔT_{out} and $\bar{h}_{\text{flow}}$, which increased $\bar{T}_{\text{out}}$, $\Delta\bar{\delta}_{\text{out}}$, and η_{total} despite the decrease in $\bar{t}$. In Table 8, a decreased $\dot{Q}_{\text{HFSS}}$ with other parameters held fixed resulted in a decreased η_{total}, primarily due to the removal of direct irradiation from the HFSS central lamp. Decreased η_{total} was also due to lower k_{eff} within the granular flow (T^3 dependence of inter-particle radiative exchange) and decreased CAM reduction near the free surface of the flow, resulting in a greater ΔT_{out}. In Table 7.9, an increased $\dot{m}_{\text{flow}}$ with other parameters held fixed resulted in increased η_{total} despite the increased $\bar{h}_{\text{flow}}$ as a result of significantly lower free surface temperatures and re-radiative losses. For all modeled conditions, low η_{total} occurred primarily due to the restricted granular flow width increasing $\bar{h}_{\text{flow}}$, decreasing $\bar{t}$, and diverting flow passed direct irradiation from two HFSS lamps.

The design-space study of $\dot{m}_{\text{flow}}$ = 230 g/min, $\dot{Q}_{\text{HFSS}}$ = 5.2 kW_{th}, and θ_{slope} = 31° study was selected for further investigation as $\bar{T}_{\text{out}} \rightarrow$ 1173 K for a CAM28 granular flow with long $\bar{t}$. Temperature contours of the 5 kW_{th} STInGR cavity surfaces and the free-surface of the granular flow are given in Figure 7.10, including (a) a side-view and (b) an isometric view for steady-state reactor operation with $\dot{m}_{\text{flow}}$ = 230 g/min, $\dot{Q}_{\text{HFSS}}$ = 5.2 kW_{th}, and θ_{slope} = 31°.

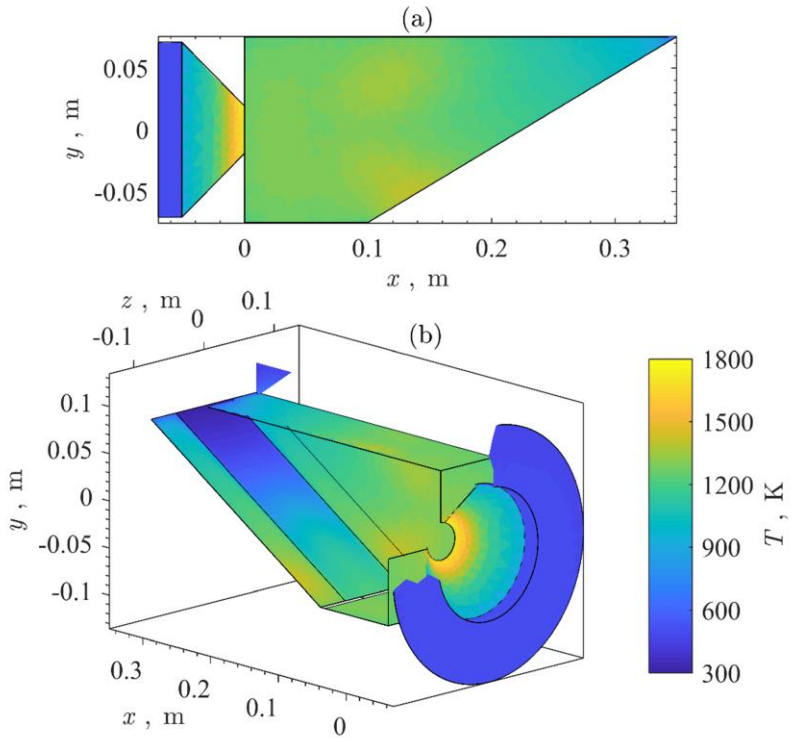

Figure 7.10. Temperature contours of reactor cavity surfaces including an (a) side-view and (b) isometric view for reactor operation with 230 g/min mass flow rate of spray-dried aluminum-doped calcium manganite particles, 5.2 kWth input supplied by the high-flux solar simulator, and inclination angle of 31°.

In Figure 7.10 a and b, localized, high-temperature regions are observed along directly irradiated reactor cavity surfaces as a result of direct irradiation from individual HFSS lamps. The highest temperature region of $T \rightarrow 1800$ K occurred at the reactor aperture due to the highly concentrated, irradiation spillage from the six HFSS lamps.

A normal view to the free surface of the particle flow is given in Figure 7.11 including contours of (a) temperature and (b) $\Delta\delta$ for steady-state reactor operation with $\dot{m}_{\text{flow}}$ = 230 g/min, $\dot{Q}_{\text{HFSS}}$ = 5.2 kW_{th}, and θ_{slope} = 31°.

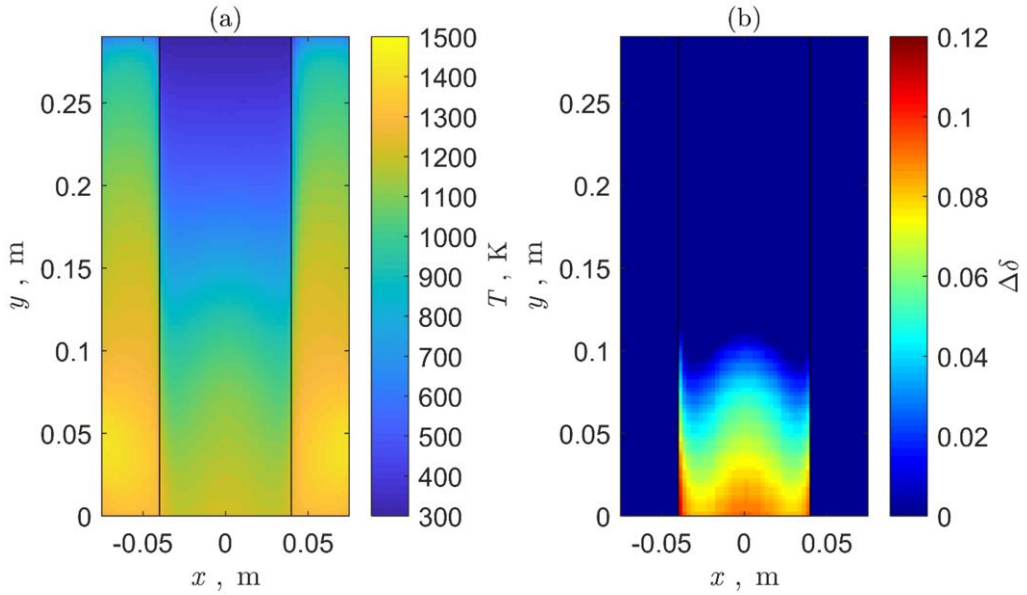

Figure 7.11. Normal view of the spray-dried aluminum-doped calcium manganite granular flow free surface within the reactor constrained between -0.04 m and 0.04 m and including bare, coated alumino-sillicate cavity walls including (a) temperature contours and (b) contours of reduction deviation from stoichiometry for reactor operation with 230 g/min mass flow rate of CAM particles, 5.2 kWth input supplied by the HFSS, and inclination angle of 31°

In Figure 7.11 a and b, the CAM granular flow lies within -0.04 m < x < 0.04 m, with high-purity alumina coated aluminosilicate surfaces locate $|x|$ > 0.04 m. In Figure 7.11a, granular flow entered at y = 0.29 m, traveled through the reactor cavity, and exited at y = 0.0 m. The particle flow was uniformly irradiated until traveling past y = 0.2 m where direct irradiation from the central HFSS lamp heated particles traveling along the central axis at x = 0.0m. In Figure 7.11a, no significant, local high temperature regions were produced within the granular flow as a result of the flow width restriction and diffuse incident irradiation supplied by the central HFSS lamp. In Figure 7.11a, the granular flow is uniformly heated, resulting in T_{max} = 1255 K at the free surface, near the edges of the flow due to conduction with the sidewalls and slight irradiation spillage from the two side-

lamps which primarily strike the alumina coated slope. In Figure 7.11b the $\Delta\delta$ distribution follows closely the temperature distribution within the granular flow with a $\Delta\delta_{max} = 0.107$.

Contours of p_{O2} along the central axis of the 5 kW_{th} STInGR are given in Figure 7.12, where solid reactor cavity surfaces are represented by solid blue regions where p_{O2} = 0 mbar.

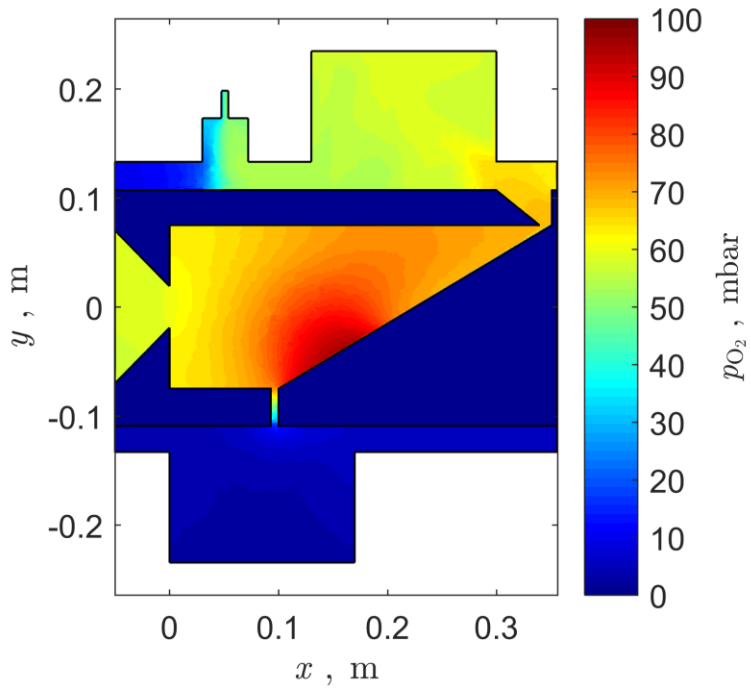

Figure 7.12. Contours of O2 partial pressure within reactor gas transport along the central reactor plane highlighting transport of evolved O2 during CAM reduction for reactor operation with 100 mbar total pressure, 230 g/min mass flow rate of CAM particles, 5.2 kWth input supplied by the HFSS, and inclination angle of 31°.

In Figure 7.12, the greatest concentration of p_{O2} = 95 mbar occurs within the central cavity immediately above the granular flow free surface. In Figure 7.12, the evolved O_2 is transported upwards towards the roof of the cavity and removed at the particle inlet due primarily to buoyancy effects. The cavity geometry resulted in significant O_2 remaining

trapped within the cavity, which inhibited reduction of the granular flow and further reinforced the importance of reduced pressure operation.

7.6.2 Sensitivity study of optimal, thermochemical storage design

A sensitivity study of various modeled parameters and granular flow properties was performed to evaluate the impact to 5 kW_{th} STInGR performance from a base modeled case with $\dot{m}_{flow}$ = 230 g/min, $\dot{Q}_{HFSS}$ = 5.2 kW_{th}, and θ_{slope} = 31°. The variables and properties investigated in the study include: u, $\dot{Q}_{HFSS}$ (6 lamp), P, f_v, $\alpha_{CAM}/\alpha_{coat}$, , $k_{p,CAM28}$, and $C_{p,CAM28}$. All variable parameters or properties were varied by ± 10% except for $\dot{Q}_{HFSS}$ (± 5%) and $\alpha_{CAM}/\alpha_{coat}$ (±0.05), as these values were closer to experimental error observed in HFSS characterization [162] and previous radiative measurements [219], respectively. The results of the study are given in Table 7.10, including 1) the base study performance with varied parameters and properties used in the study, and 2) variables to which the model was most sensitive.

Table 7.10. Sensitivity study of various modeled parameters and granular flow properties for optimal case for spray-dried aluminum doped calcium manganite granular flow within the 5 kW_{th} STInGR

Base Study										
u, m/s	$\dot{Q}_{HFSS}$, kW_{th}	P, mbar	f_v	α_{CAM}, α_{coat}	ΔH_{rxn}, kJ/kg	k_p, W/m-K	C_p, kJ/kg-K	$\bar{T}_{out}$, K	$\Delta\bar{\delta}_{out}$	η_{total}
u	5.2 (6 lamps)	100	0.6	α_{CAM}, α_{coat}	ΔH_{rxn}	k_p	0.918	1158	0.076	0.628

Sensitivity Study				
Variable	Value	$\bar{T}_{out}$, K	$\Delta\bar{\delta}_{out}$	η_{total}
u	$1.1 \cdot u$ (+10%)	1105 (-4.6%)	0.057 (-25.0%)	0.638 (+1.6%)
u	$0.9 \cdot u$ (-10%)	1221 (+5.4%)	0.099 (+30.2%)	0.616 (-1.9%)
$\dot{Q}_{HFSS}$ (6 lamps)	5.46 (+5%)	1193 (+3.0%)	0.088 (+15.8%)	0.627 (-0.1%)
$\dot{Q}_{HFSS}$ (6 lamps)	4.94 (-5%)	1124 (-2.9%)	0.064 (-15.8%)	0.628 (+0.0%)
α_{CAM}, α_{coat}	α+0.05	1185 (+2.3%)	0.086 (+13.2%)	0.652 (+3.7%)
α_{CAM}, α_{coat}	α-0.05	1136 (-1.9%)	0.068 (-10.5%)	0.607 (-3.3%)
C_p	1.010 (+10%)	1111 (-4.1%)	0.059 (-22.4%)	0.637 (+1.4%)
C_p	0.826 (-10%)	1213 (+4.7%)	0.096 (+26.3%)	0.617 (-1.8%)

The modeled 5 kW_{th} STInGR performance was most sensitive to variations in radiative properties of the CAM and high-purity alumina coating due to the increased absorption of incident irradiation in the visible spectrum from the HFSS. Decreased (-10%) u and C_p both exhibited similar impact to reactor performance parameters. Decreased (-10%) u and C_p and increased (+5%) $\dot{Q}_{HFSS}$ resulted in a greater decrease to η_{total} compared with the alternate parameter variation due to increased re-radiative losses from the granular flow surface. The η_{total} was relatively unaffected by variations in $\dot{Q}_{HFSS}$ as a result of the reactor cavity radiative performance. Variations in P and f_v exerted little influence on the

modeled performance and only resulted in small changes in p_{O2} within the granular flow. Additionally, variations in ΔH_{rxn} were overcome by the magnitude of $\Delta\delta$, and variations in k_p imparted little impact to k_{eff} as inter-particle radiative exchange was the dominant term in effective conductivity [108].

7.6.3 Comparison to state-of-the-art granular flow material

The 5kW$_{th}$ STInGR performance is compared using granular flows of CAM and ID50 for the same modeled operating parameters of $\dot{m}_{flow}$ = 230 g/min, $\dot{Q}_{HFSS}$ = 5.2 kW$_{th}$, and θ_{slope} = 31,35° and identical reactor cavity geometry. Results of the comparison are given in Table 7.11.

Table 7.11. Comparison of spray-dried aluminum-doped calcium manganite to Accucast ID50 granular flows in the 5 kW$_{th}$ solar thermochemical inclined granular-flow reactor for similar modeled conditions

Material	θ_{slope}, °	$\bar{h}_{flow}$, mm	$\bar{t}$, s	ΔT_{outlet}, K	$\bar{T}_{out}$, K	$\Delta\bar{\delta}_{out}$, --	η_{total}, --	$\dot{R}$, (kJ/kg)/s
CAM	31	0.75	8.56	138	1158	0.076	0.628	99.5
ID50		1.39	15.59	168	1137	n/a	0.636	55.6
CAM	35	0.44	4.45	120	1165	0.078	0.635	193.6
ID50		0.83	8.31	127	1155	n/a	0.643	105.0

As anticipated, $\eta_{total,CAM} \leq \eta_{total,ID50}$ for similar θ_{slope}'s due to $C_{p,CAM28} < C_{p,ID50}(T)$ and $\bar{t}_{CAM} < \bar{t}_{ID50}$. However, due to $\bar{h}_{flow,CAM} < \bar{h}_{flow,ID50}$ more uniform and more rapid energy storage is achieved within the CAM granular flows resulting in $\dot{R}_{CAM} > \dot{R}_{ID50}$ for similar θ_{slope}'s. This metric indicates the CAM granular flows exhibit greater potential for scaled-up systems compared to ID50 granular flows, as CAM granular flows can achieve significant energy storage with reduced residence times.

7.7 Model Verification

Grid independence was demonstrated for the $\dot{m}_{flow}$ = 300 g/min and θ_{slope} = 31° CFD model, as all modeled domains include slight variations in geometry from this model. Grid independence was demonstrated in the mesh by progressively refining 1) discretization of the granular flow, 2) discretization of directly-irradiated surfaces for MCRT / CFD coupling, and 3) discretization of radiative modeled domain for the FV-RTE. Discretization refinement was performed until reactor performance parameters varied < 1% between discretizations. Based on these results, a mesh of 641,081 cells with 6 x 36 x 85 discretization of the dense, granular flow and 5 x 5 radiation mesh with 3 x 3 pixelation was selected. All modeled domains for remaining CAM and ID50 models were constructed using identical discretization restrictions.

For all heat and mass transfer modeling, convergence was defined as a decrease to 10^{-4} for scaled residuals of continuity and momentum, $5 \cdot 10^{-5}$ for species and radiation, 10^{-6} for energy, and a maximum change in $\delta < 0.1\%$ between iterations, although residuals often decreased below these limits. Average cavity surface temperatures, average free-surface p_{O2}, and reactor performance parameters were also monitored to ensure convergence. A mass imbalance of < 0.5% between the Ar / O_2 flow outlet and the combined Ar inlet flow and evolved O_2 from the granular flow was determined to ensure O_2 evolution from the granular flow free surface was captured.

7.8 Conclusions

The 5 kW_{th} scale solar thermochemical inclined granular-flow reactor was designed for operation within a seven lamp high-flux solar simulator at reduced operating pressures. Dense, granular flows of spray-dried aluminum-doped calcium manganites were

investigated as potential thermochemical energy storage media by extracting steady, granular flow characteristics and performing detailed heat and mass transfer analysis using commercial computational fluid dynamics software ANSYS Fluent 17.1. A design-space study with variable granular flow mass flow rate (230-300 g/min), power input (4.3 – 5.2 kW_{th}), and inclination angle (31 – 35°) was performed to evaluate granular flow performance using the mass-weighted outlet flow temperature, stoichiometric deviation, and total, system efficiency. From the study, increased inclination angle resulted in reduced granular flow thickness, significantly reducing the conductive resistance through the granular flow and improving its performance despite a decreased average residence time. A 230 g/min granular flow irradiated by 5.2 kW_{th} radiative input along a 31° slope inclination angle achieved a modeled outlet flow temperature of 1158 K, stoichiometric deviation of 0.076, and total system efficiency of 0.628 while avoiding significant particle overheating and promoting long residence times. From a sensitivity study, the modeled granular flow performance was determined most sensitive to variations in flow velocity, high-flux solar simulator output, cavity radiative properties, and particle specific heat. Reactor performance was compared using dense, granular flows of spray-dried aluminum-doped calcium manganites and Accucast ID50, a state-of-the art inert granular media used in concentrated solar power applications. Additionally, reactor performance was compared using a proposed metric, the storage density rate. The storage density rate of the spray-dried aluminum-doped calcium manganite granular flows outperformed the Accucast ID50 as a result of the thinner flows achieved for equivalent mass flow rates.

Overall, this study has demonstrated the importance of extracting predictive, granular flow characteristics in maximizing the performance of dense, granular flows for

thermochemical energy storage. These results provide engineering guidance to the performance of dense, granular flows of spray-dried aluminum-doped calcium manganites within the 5 kW_{th} scale solar thermochemical inclined granular flow reactor and insight into future scale-up reactor designs.

CHAPTER 8. HFSS EXPERIMENTATION OF 5 KW_{TH} STINGR

8.1 Introduction

A 5 kW_{th} laboratory scale solar thermochemical inclined granular flow reactor [109] was fabricated and tested within a seven Xe arc-lamp high flux solar simulator [162] using spray-dried aluminum-doped calcium manganite granular powders as a heat transfer and thermochemical energy storage media. The reactor design and high-flux solar simulator operating conditions were tuned to overcome severe particle agglomeration within the directly-irradiated granular powders while maintaining continuous operation.

8.2 Experimental Setup

A 5kW_{th} scale Solar Thermochemical Inclined Granular-flow Reactor (STInGR) was designed and fabricated based on prior modeling results [109] to achieve thermochemical storage of concentrated irradiation within dense, granular flows of particulate media. The performance of dense, granular flows of spray-dried aluminum-doped calcium manganite particles (Coorstek) was first investigated within the reactor. The STInGR system is schematically depicted in Figure 7.1 with (a) a Solidworks rendering of the reactor design and (b) a process flow diagram of the reactor with concentrated irradiation delivered by a high-flux solar simulator (HFSS).

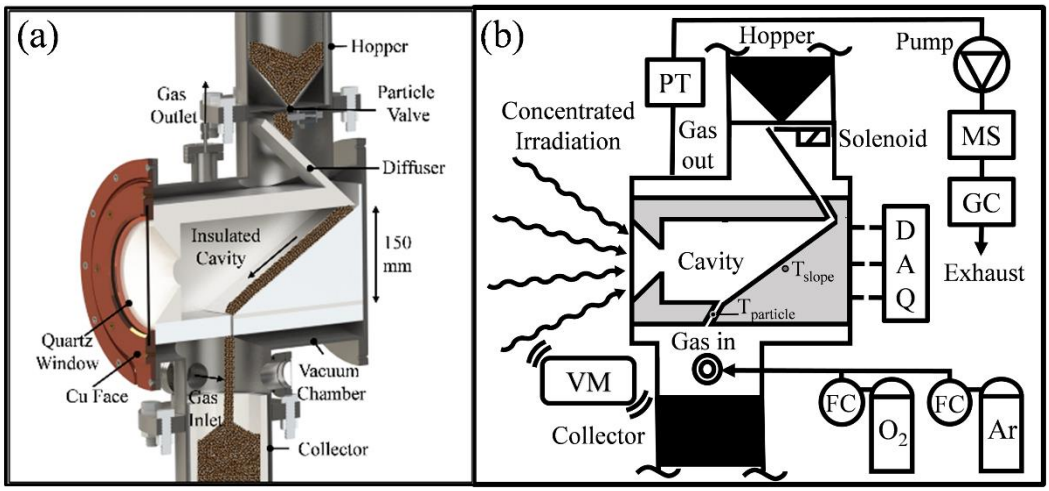

Figure 8.1. Design of the 5 kW_{th} solar thermochemical inclined granular-flow reactor with (a) a Solidworks rendering of the final design and (b) a process flow diagram of the reactor within the high-flux solar simulator

The 5 kW_{th} STInGR includes an insulated, internal cavity made from high-strength alumino-sillicate boards (Zircar Zirconia M35 buster-type insulation). The boards were machined to form a 50 mm conical aperture with 45° acceptance angle, rectangular cavity (150 x 150 x 100 mm^3), directly-irradiated slope, and granular flow channel. Directly-irradiated cavity surfaces were coated with a reflective, high-purity alumina coating (Aremco Pyropaint^{TM} 634-AL). An 80 mm wide granular flow channel was fabricated from multiple, interlocking aluminosilicate boards to accommodate thermal expansion during high temperature operation. The boards were coated with high-purity alumina to develop a uniform surface roughness. The surface roughness was tuned to promote a dense granular flow ([116-118] and Chapter 7) and to reduce frictional wear of the aluminosillicate board [231]. The assembled granular flow channel produced a directly-irradiated stair-step granular flow path along the inclined plane, pictured in Figure 8.2.

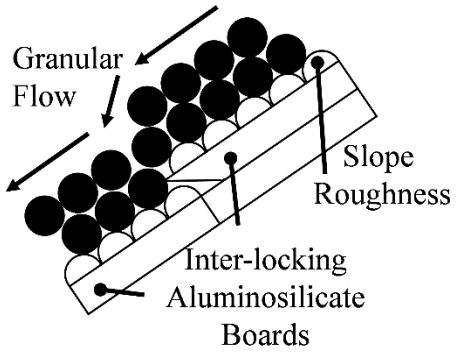

Figure 8.2. Schematic of granular flow channel composed of interlocking aluminosilicate boards to accommodate thermal expansion and producing a stair-step granular flow behavior

The reactor cavity was assembled within a stainless steel case (190 x 215 x 405 mm^3) to preserve cavity stability during high temperature operation and during insertion or removal from the vacuum chamber between experiments. The vacuum chamber was manufactured from a stainless steel tube (NPS 10 Schedule 5) and fitted with steel flanges and feedthroughs to facilitate gas, instrumentation , and particle transport within the reactor while operating at reduced pressures. The vacuum chamber was sealed with custom, mica gaskets using a steel back plate, vertical cylindrical stainless steel hopper and collector assemblies (NPS 6 Schedule 5), and a water-cooled Cu face. A 5 mm thick, 220 mm diameter quartz window (145 mm diameter across directly-irradiated cavity) was housed within the water-cooled Cu face assembly and sealed using custom mica gaskets.

Concentrated irradiation from the HFSS was introduced through the quartz window while maintaining reduced operating pressures with an oil-free rotary vane pump (Edwards nXDS10i oil-free scroll pump), monitored with a pressure transducer (PT, Omega PXM209). Ar / O2 sweep gas was introduced via mass flow controllers (FC, Bronkhorst F-201CV-20K-MAD-33-V) to further reduce O_2 partial pressure within the reactor or to promote material re-oxidation after a completed experiment. Gas flow was introduced and

removed from the vacuum chamber through gas vacuum feedthroughs (Kurt J. Lesker F0275X4SWG). Gas composition was temporally monitored using coupled gas chromatography (GC, Agilent 490 Micro GC with Molsieve and PoraPLOT Q columns) and mass spectrometry (MS, OmniStar ThermoStar GSD320 Gas Analysis System). Particles are loaded into an upper hopper assembly [199, 200] prior to sealing. Particle mass flow rate was controlled via a coupled orifice plate and solenoid valve [201, 232] powered using an electrical vacuum feedthrough (Kurt J. Lesker IFTRG067013). Particles were introduced into the granular flow channel using a diffuser plate, reducing particle kinetic energy and promoting uniform flow depth and width. A dense, granular flow was achieved within a custom flow channel along the inclined plane and was directly irradiated by a concentrated, radiative input. A vibratory motor (VM, Vibco SPR-21) was attached to the structural frame supporting the 5 kW_{th} STInGR to inhibit agglomerated particles from stagnating along the directly-irradiated flow channel during high temperature operation.

Sheathed, type N fine gage thermocouple probes (Omega SNNXL-020U-8.5-SHX) were placed at two locations within the reactor cavity: (1) ~ 6 – 7 mm below the aluminosilicate board to monitor cavity / granular flow channel temperature and (2) across the granular flow outlet to monitor the average granular flow temperature. The N-type thermocouple array at the flow outlet was designed to be fully immersed within the granular flow upon exit from the reactor cavity and was shielded by an aluminosilicate overhang to prevent direct irradiation of the probes. Unsheated, Type J thermocouples (Omega 5TC-GG-J-20-6) were installed throughout the reactor to monitor lower temperature components and critical seals. Thermocouples were introduced into the

vacuum chamber using thermocouple vacuum feedthroughs (Kurt J. Lesker custom N-type XTEMP-FT and TFT5JY00003). A hand-held infrared thermometer (ETEKCITY LaserGrip 1080 infrared thermomemeter) was also used to investigate temperatures of critical seals, reactor surfaces, and the quartz window.

The fully fabricated 5 kW_{th} STInGR is pictured in Figure 8.3 including (a) the STInGR sealed with upper hopper and lower collector assemblies and mounted within the support frame, (b) a closer view of STInGR and water-cooled Cu face, and (c) assembled aluminosilicate cavity within stainless steel sleeve.

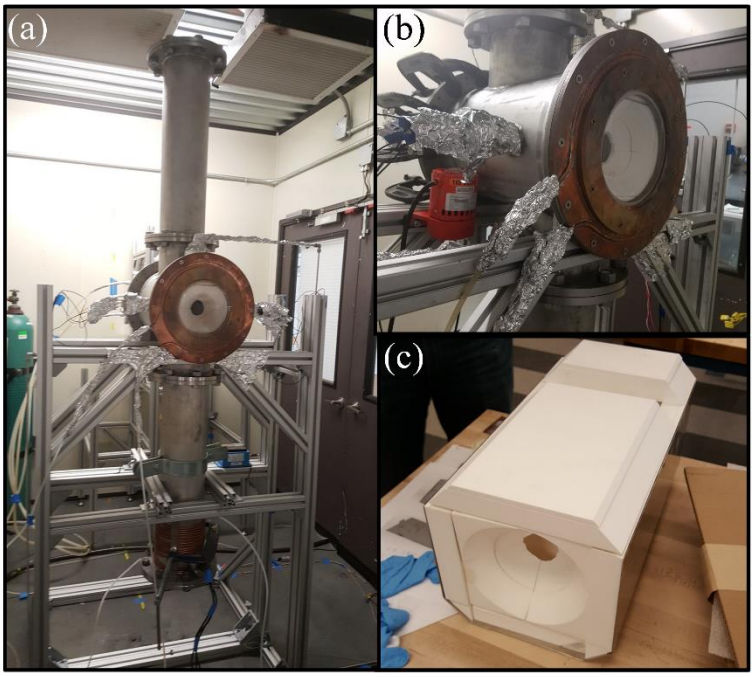

Figure 8.3. Fully-fabricated 5 kWth laboratory scale solar thermochemical inclined granular flow reactor (a) front-view with upper hopper and lower collector assemblies mounted in the support frame and, (b) closer, side-view, and (c) assembled aluminosilicate cavity within stainless steel sleeve

Granular flow performance within the 5 kW_{th} STInGR was evaluated based upon the average outlet granular flow temperature, evolved O_2 (*i.e.* deviation from stoichiometry), and total system efficiency, given as:

$$\eta_{\text{total}} = \frac{\dot{m}_{\text{flow}} \cdot \left(C_{\text{p}} \left[T_{\text{particle}} - T_{\text{hopper}} \right] + \Delta H_{\text{rxn},0\rightarrow\delta} \right)}{\dot{Q}_{\text{HFSS}}} \tag{8.1}$$

where $\dot{m}_{\text{flow}}$ is the prescribed, granular flow mass flow rate; C_{p} is the specific heat capacity of the aluminum-doped calcium manganite; T_{particle} is the outlet granular flow temperature; T_{hopper} is the average hopper temperature near the particle inlet assumed equal to the particle temperature; $\Delta H_{\text{rxn},0\rightarrow\delta}$ is the reaction enthalpy assuming stoichiometric deviation of $0 \rightarrow \delta$ based on evolved O_2 [205]; and is the radiative input delivered by the HFSS lamps within a 50 mm aperture at the focal plane. Thermophysical properties for the aluminum-doped calcium manganites were assumed similar to the properties for CAM28 investigated in previous studies ([44, 233] and Chapter 7).

8.3 Agglomeration potential of spray-dried calcium manganites

Initial HFSS experimentation was performed with dense, granular flows of spray-dried calcium manganite granular powders ($\bar{d}_{\text{p}}$ = 45 μm) for θ_{slope} = 31 - 35° and various $\dot{Q}_{\text{HFSS}}$ = 4.3 – 5.2 kW_{th} to investigate performance conditions identified in prior steady-state modeling studies. Significant inter-particle agglomeration was observed to occur for T_{particle} > 1150 K, producing an agglomerated structure of particles along the directly-irradiated granular flow channel. Significant particle agglomeration is pictured in Figure 8.4 including (a) an optical microscopy (Leica DVM 6 Optical Microscope) image of an agglomerate structure removed from the reactor and (b) an image of an agglomerate structure within the granular flow channel.

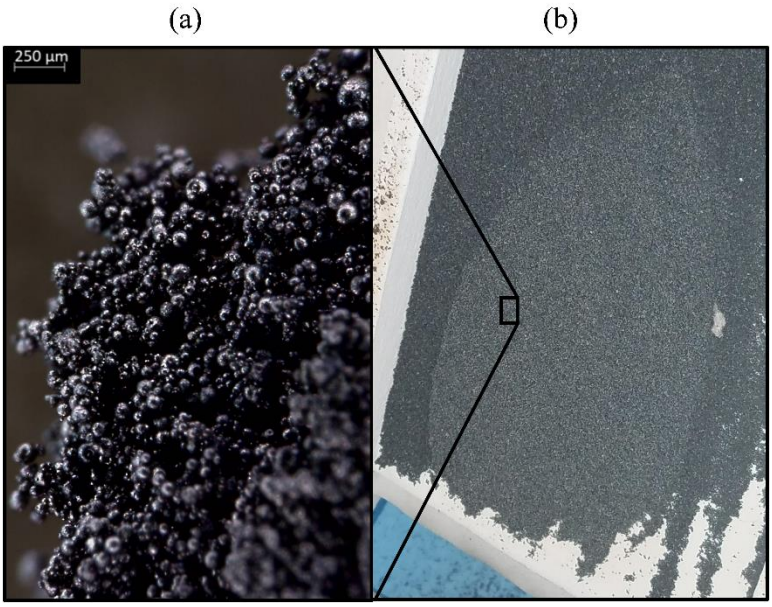

Figure 8.4. Significant particle agglomeration observed in limiting performance studies with (a) an optical microscopy image of an agglomerate structure removed from the reactor after testing and (b) an image of an agglomerate structure within the granular flow channel

As seen in Figure 8.4a, weakly connected, inter-particle chains were observed which formed a clustered structure of individual particles, with no observable sintering. As seen in Figure 8.4b, when an agglomerate structure formed, the gravitational shear along the incline was not sufficient to overcome the inter-particle agglomeration and frictional effects at the slope, holding the agglomerate structure in place and diverting granular flow. In Figure 8.4b, a significant agglomerate structure was formed near the flow outlet where particles achieve the highest $T_{\text{particle.}}$ The agglomerate did not appear to adhere to the flow channel and was easily brushed from the slope, yet retained an inter-particle agglomerate structure. Agglomerate structures were also found to break apart and return to a granular powder with little mechanical agitation after an experiment.

The crystallographic structure of the granular powder and potential phase impurities were examined using X-ray diffractormetry (XRD, PANalytical X'Pert PRO Alpha-1 diffractometer). XRD diffraction patterns are included in Figure 8.5 for spray-

dried, aluminum-doped calcium managanite granular powder samples in the as-received (fresh) condition, cycled through multiple STInGR reduction / oxidation cycles, and calcined in an air furnace (Sentro Tech Corp. ST-1600C-445) heated to 1473 K and held for 8 hours, and compared to high-purity CAM28 particles[4].

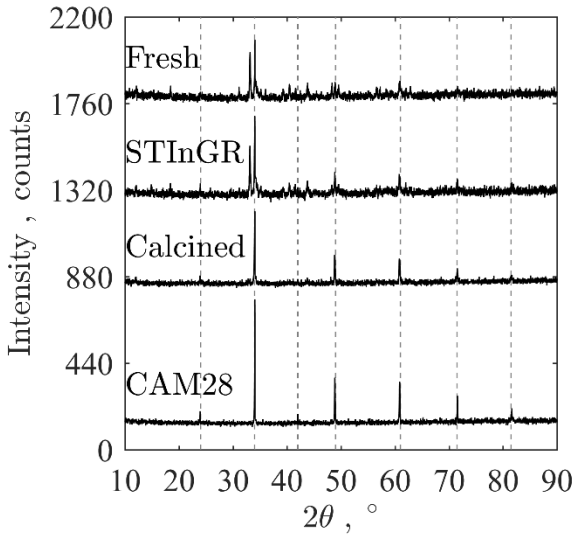

Figure 8.5. Intensity as a function of 2θ angle from X-ray diffractometry measurements for spray-dried, aluminum-doped calcium managanite granular powder samples in the as-received (fresh) condition, cycled through multiple reactor (STInGR) reduction / oxidation cycles, and calcined in an air furnace heated to 1473 K and held for 8 hours, and compared to high-purity $CaAl_{0.2}Mn_{0.8}O_{3-\delta}$ particles

In Figure 8.5, the extracted peaks of the high-purity perovskite structure for CAM28 include the expected orthohombric structure of a calcium manganite based perovskite oxide [44]. Both fresh and STInGR-cycled XRD diffractrometry patterns included peaks associated with the orthorhombic structure. However, significant peak splitting and the existence of a prominent peak near $2\theta = 33°$ not observed in the high-purity CAM28 material suggests the existence of secondary phases within the granular powder. Potential impurities include Ca_2MnO_4, $CaMn_2O_4$, and $CaAl_{0.5}Mn_{0.5}O_{2.5}$, where

Synthesis of $CaAl_{0.2}Mn_{0.8}O_{3-\delta}$ performed by Dr. Sean Babiniec of Sandia National Laboratories[4]

Ca_2MnO_4 was observed in a prior study exhibiting significant agglomeration of spray-dried calcium manganites for temperatures 1173-1273 K [49]. In Figure 8.5, additional calcination greatly increased the prominence of peaks associated with an orthohombric structure. While calcination improved XRD peaks, the calcined particles continued to form solid agglomerate structures within the air-furnace during repeated calcination runs.

Particle size dependence for agglomeration was investigated by sieving particles into different size ranges and heating to 1173 K in an air furnace (MTI Corp. KSL-1200X) and held for 1 hour. Agglomerated structures were observed for all particle sizes less than 106 microns with more significant structures identified for smaller particle sizes, suggesting the particle fines contribute to the agglomeration potential.

As a result of these initial studies, STInGR operating conditions were selected to promote continuous operation by avoiding significant inter-particle agglomeration.

8.4 High Flux Solar Simulator Reduction Experiments

HFSS experiments with STInGR were performed to approach steady-state operating conditions with continuous thermochemical energy storage of incident irradiation within a dense, granular flow of aluminum-doped calcium manganites. The major experimental conditions used for testing in the HFSS are provided in Table 8.1.

Table 8.1. Steady-state experimental conditions for testing in the high-flux solar simulator

Parameters	Values
d_{aperture}	50 mm
$\dot{V}_{\text{Ar}}$	0.5 Ln/min
$\dot{Q}_{\text{HFSS}}$	4.04± 0.1 kW_{th}
w_{cavity}, h_{cavity}	150 mm
l_{cavity}	100 mm
w	80 mm
$\overline{d}_{\text{p}}$	45 μm
P	80 – 95 mbar
θ_{slope}	35°
$\dot{m}_{\text{flow}}$	220 ± 5 g/min

The $\dot{Q}_{\text{HFSS}}$ was determined from coupled calorimetry measurements and the calibrated Monte Carlo ray tracing analysis of the characterized HFSS [162]. The P was determined to remain relatively constant during initial sealing and during high temperature operation but was dependent upon given sealing conditions for a particular experiment. The reactor cavity was cleaned in-between experiments and fully re-assembled to the same geometry specifications. A representative, experimental summary of STInGR in the HFSS is given in Figure 8.6, including temporal measurements of embedded slope temperature T_{slope}, average particle outlet temperature $\overline{T}_{\text{particle}}$, molar flow rate of evolved O_2 $\dot{n}_{O_2,\text{evolved}}$, and $\dot{Q}_{\text{HFSS}}$.

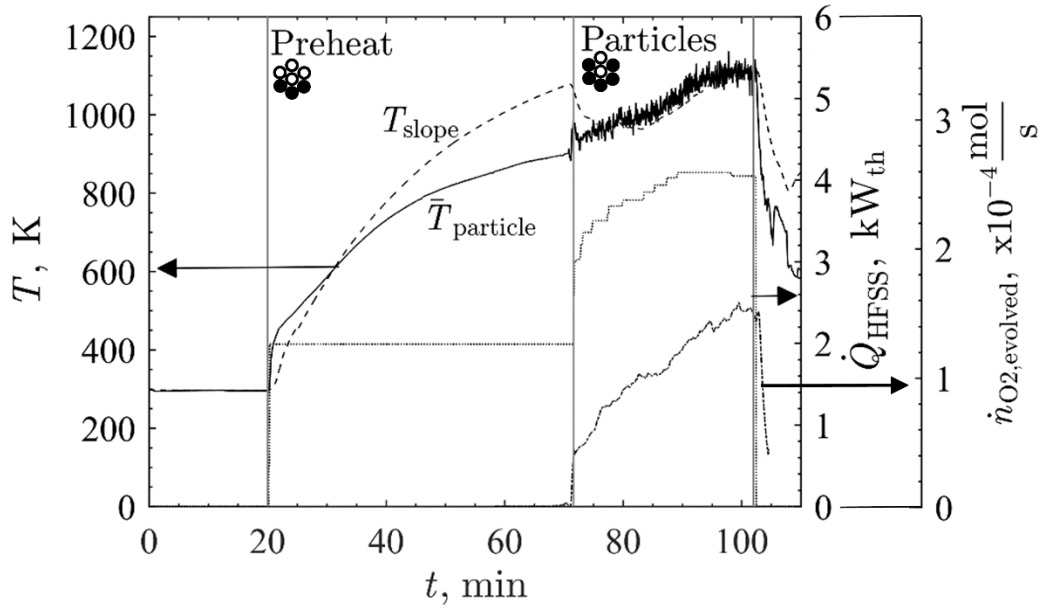

Figure 8.6. Experimental summary of solar thermochemical inclined granular flow reactor experiments in the high-flux solar simulator monitoring lamp power delivered to a 50 mm aperture at the focal plane, slope and outlet particle temperatures, and evolved O_2

Initially, the STInGR operating pressure was reduced using the vacuum pump and 0.5 L_n/min of Ar sweep gas was introduced into the reactor until a steady operation pressure and product gas composition was observed. The STInGR was then preheated for ~50 minutes using three, lower HFSS lamps at lower power levels until $T_{slope} \rightarrow 1073$ K to reduce thermal stresses along the granular flow channel. Once $T_{slope} = 1073$ K, particles were introduced at a controlled mass flow rate via the coupled orifice plate and knife valve. The the vibratory motor was excited to inhibit agglomeration along the granular flow channel. In Figure 8.6, the introduction of particles at $t = 70$ min resulted in a rapid decrease in T_{slope} and a rapid increase in $\bar{T}_{particle}$ and $\dot{n}_{O_2,evolved}$ as concentrated irradiation is stored within the thermal capacitance and endothermicity of the granular flow. $\bar{T}_{particle} > T_{slope}$ is expected as the granular flow receives direct irradiation from the HFSS lamps and advects absorbed radiation downstream towards the outlet thermocouple array. The fluctuating

measurements of $\bar{T}_{\text{particle}}$ are a result of intermittent granular flows coming into direct contact with the outlet thermocouple array, with a sudden increase in $\bar{T}_{\text{particle}}$ resulting from contact of the granular flow with an outlet thermocouple. A comparison between the desired, steady, granular flow [117, 118] and the observed, intermittent granular flow during high-temperature operation is given in Figure 8.7.

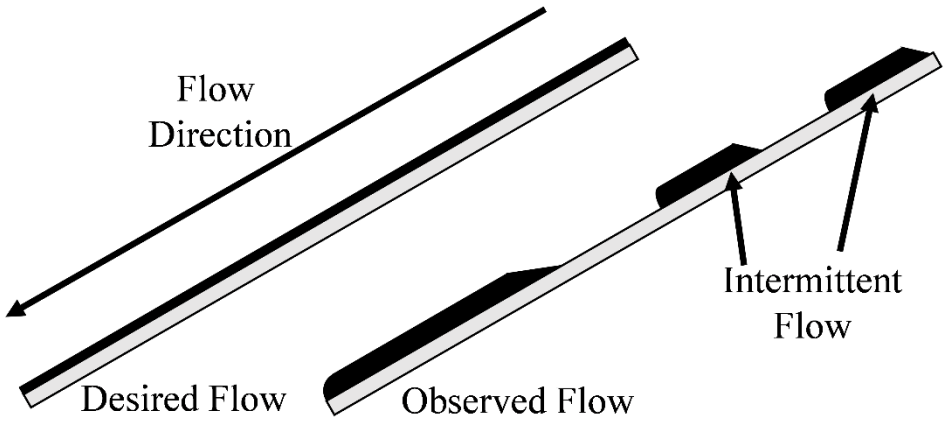

Figure 8.7. Schematic of desired, steady, dense granular flow compared to the observed, intermittent, dense granular flows during high temperature operation with the spray-dried, aluminum-doped calcium manganite granular powder

In Figure 8.7, the observed flow during high-temperature operation was characterized by thick, dense, intermittent waves of particles along the granular flow channel. The intermittent flows did not always cover the full flow channel width and would often contact only a portion of the outlet thermocouple array. The intermittent flow resulted from a slightly agglomerated heap formed at the top of the incline as particles were introduced into the irradiated cavity. The heap would build until gravitational shear forces broke the heap and a dense, granular flow was developed along the incline. Upon particle introduction, the $\dot{Q}_{\text{HFSS}}$ was first increased by introducing two additional, peripheral HFSS

lamps and gradually increasing the power supplied to the five lamps until near steady-state operating conditions were observed.

After approximately 5 minutes of steady state operation was observed, the HFSS was turned off, and the collected particles were re-oxidized. Re-oxidation occurred by turning off the vacuum pump and re-pressurizing the cavity with O_2 from the mass flow controllers until near atmospheric pressures were achieved. The observed, steady-state operation for two repeated STInGR experiments at similar operating conditions are given in Figure 8.8a and b, respectively, including temporal measurements of the range of T_{particle}, T_{slope}, and the molar flow rate of evolved O_2 $\dot{n}_{O_2,\text{evolved}}$.

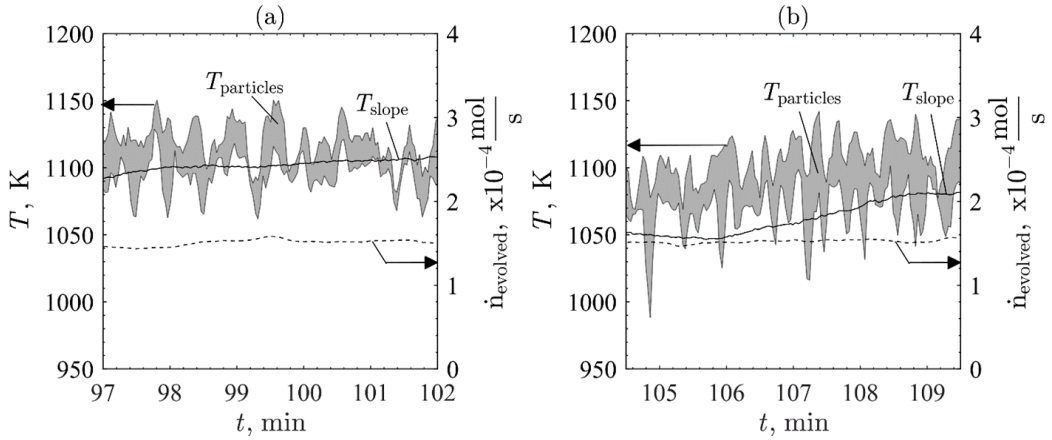

Figure 8.8. Temporal measurements of the temperature range of the particle outlet thermocouple, slope temperature, and evolved O_2 for near steady-state operating conditions during high-flux solar simulator experimentation for (a) initial (b) repeated trials

In Figure 8.8a and b, rapid increases in T_{particle} were associated with the intermittent dense flow striking a portion of the thermocouple array. For instances with a wide range of T_{particle} the intermittent flow likely did not cover the full width of the flow channel when contacting the outlet thermocouple array. For the repeated experiments, a repeatable granular flow temperature $1110 < T_{\text{particle}} < 1140$ K was recorded during contact between

an intermittent flow and the outlet thermocouple array. Maximum $T_{particle}$ < 1150 K was achieved and significant agglomeration of particles along the directly irradiated flow channel were avoided. In Figure 8.8, a and b, the evolved O2 was associated with a bulk $0.011 < \Delta\delta < 0.012$. The low $\Delta\delta$ was likely due to a combination of reduced particle residence times along the directly irradiated portion of the slope and due to the presence of phase impurities in the spray-dried aluminum-doped calcium manganite granular powder. The impact of phase impurities on reduction potential was investigated using thermogravimetric analysis (TGA, Netzsch STA 449 F3 Jupiter) for reduction / oxidation studies of the granular powder with reduction cycles of p_{O2} = 100 mbar and 1473 K and oxidation cycles of p_{O2} = 800 mbar and 773 K., Fresh, STInGR-cycled, and calcined granular powders achieved a mass loss / gain of 1.6%, which is significantly less than the mass loss / gain (~2.2%) for CAM28 at similar cycling conditions. A $0.67 < \eta_{total} < 0.70$ was determined for reactor operation at the given steady-state operation conditions based upon the measured range in $T_{particle}$ and $\Delta\delta$, respectively. A lower η_{total} was observed despite the increased residence time of the particles at the top of the inclined slope, due to the restricted flow width which reduced the amount of direct, incident HFSS irradiation.

Two pictures of the intermittent, dense, granular flow viewed through the quartz window and 50 mm aperture immediately following HFSS experimentation are given in Figure 8.9 for views (a) normal to the aperture and (b) off-normal to the aperture.

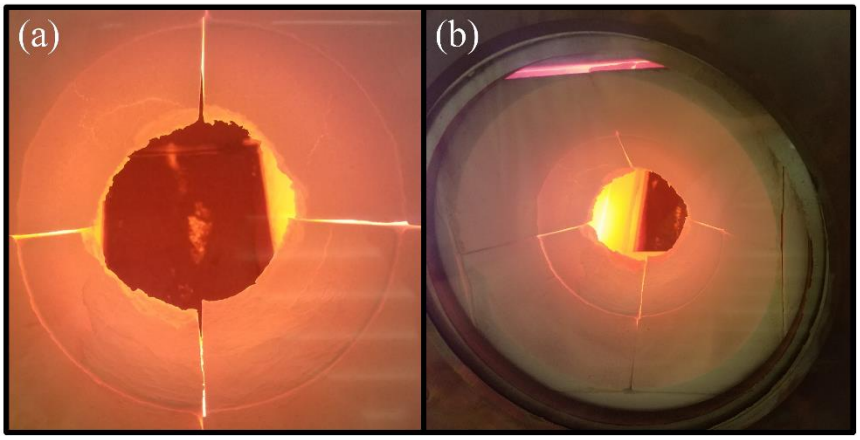

Figure 8.9. Images of intermittent, dense, granular flow of spray-dried aluminum-doped calcium manganites viewed through the quartz window and 50 mm aperture immediately after high-flux solar simulator experimentation for views (a) normal to the aperture and (b) off-normal to the aperture

In Figure 8.9a, the intermittent, dense granular flow is observed to not be evenly distributed across the granular flow channel as is shown by the exposed slope behind the granular flow along the center of the granular flow channel. In Figure 8.9b, an angled view through the aperture revealed the formation of a local, high temperature region produced by direct irradiation from a single lamp as observed in previous steady-state modeling studies ([109] and Chapter 7).

8.5 Conclusions

A novel 5 kW_{th} laboratory-scale solar thermochemical inclined granular flow reactor was fabricated and tested in a high flux solar simulator using spray-dried aluminum-doped calcium manganites as a heat transfer and thermochemical energy storage medium. This reactor was designed to promote effective and efficient storage of concentrated solar energy through direct solar irradiation of the reacting material, continuous on-sun operation, and matched incident concentrated solar power to the rate of sensible and chemical energy storage of the reacting material. The reactor and high-flux solar simulator

operating conditions were tuned to accommodate for severe inter-particle agglomerations observed in the spray-dried aluminum-doped calcium manganite particles for temperatures exceeding 1150 K. The reactor was able to operate continuously with intermittent, dense granular flows with granular flow temperatures > 1073 K and thermochemical energy storage with a maximum absorption efficiency of nearly 0.7.

CHAPTER 9. RESEARCH CONTRIBUTIONS, FUTURE WORK

A novel, solar thermochemical inclined granular-flow reactor was designed, fabricated, and tested to achieve operating temperatures > 1073 K of heat transfer media with thermochemical energy storage of solar energy. The reactor was developed for a newly proposed concentrated solar power technology: an Air-Brayton cycle coupled to a two-step solar thermochemical cycle using redox-active metal oxides as heat transfer and energy storage media. This novel cycle was investigated using thermodynamic analysis to evaluate its performance using a candidate metal oxide pair, Co_3O_4 / CoO. Co_3O_4 was further investigated using thermogravimetry to extract apparent reduction kinetics and further inform reactor design. Modeling and experimental studies produced various research contributions in developing the solar thermochemical inclined granular-flow reactor, highlighted in the following section.

9.1 Research Contributions

A thermodynamic analysis was performed to evaluate the potential of an Air-Brayton cycle coupled to a two-step solar thermochemical cycle using redox-active metal oxides as heat transfer and energy storage media. The proposed cycle included two major stages:

1. thermal and chemical storage of concentrated solar energy within the bulk transport of metal oxide particles using a solar thermochemical reactor, and

2. on-demand process heat delivery to an Air Brayton cycle for solar electricity production from stored thermal and chemical energy within metal oxide particles using a secondary pressurized air-reactor.

The cycle stages can be decoupled to produce solar electricity during non-ideal solar conditions. The cycle was first evaluated using the redox-active Co_3O_4 / CoO binary metal oxide pair. A radiative heat transfer model of an ideal, windowed, solar thermochemical reactor was developed to capture the storage of incident irradiation in the cycle. A maximum solar-to-electricity cycle efficiency of 44% was determined for re-oxidizing the CoO at 30 bar, with the maximum solar-to-electricity cycle efficiency reducing to 26% for a decrease in pressure to 5 bar. High, theoretical cycle efficiencies indicate the technology is promising but requires components which minimize irreversibilities (exergetic losses) to approach predicted efficiencies, with the solar thermochemical reactor (stage 1) warranting initial investigation.

To inform solar thermochemical reactor design, kinetic analysis to identify the mechanisms and determine kinetic parameters for the reduction of Co_3O_4 were performed using a combination of isothermal and non-isothermal thermogravimetry. The Co_3O_4 reduction between 1113 and 1213 K followed an Avrami–Erofeyev nucleation model. The O2 partial pressure dependence between 0% and 20% O2–Ar was determined with a power rate law.

From both the thermodynamic and kinetic analyses, a $5kW_{th}$, solar thermochemical inclined granular flow reactor concept was proposed and investigated using Co_3O_4 / CoO metal oxide particles for thermochemical energy storage. The reactor concept was evaluated using a design-stage heat and mass transfer model coupling Monte Carlo ray-tracing for radiative heat exchange to identify optimal reactor design and operating conditions to promote thermal and chemical storage of incident irradiation. The parametric study of the reactor design was performed with varying cavity depth, particle inlet

temperature, and solar concentration ratio to maximize conversion of Co_3O_4 to CoO and particle outlet temperature while preventing particle overheating.

A modeling method was developed for mapping Monte Carlo ray tracing results to commercial computational heat transfer and fluid dynamics reactor models to develop more informed modeling efforts in designing of the 5 kWth scale reactor. The method was determined well-suited to models with highly directional and spatially varying radiative inputs as is common with solar reactors. The method was designed to be compatible with two and three dimensional structured and unstructured discretizations while achieving energy conservation and preserving spatial variation.

Building upon previous modeling efforts, a 5 kW_{th} laboratory-scale solar thermochemical inclined granular flow reactor was designed. Reactor performance was evaluated using dense, granular flows of aluminum-doped calcium manganite particles. An experimental tilt-flow rig and particle image velocimetry were used to extract granular flow characteristics used in frictional and velocity scaling arguments for dense, steady granular flows. Flow characteristics were applied to detailed heat and mass transfer models of the reactor performance within the high-flux solar simulator. Modeling was performed in ANSYS Fluent 17.1 to evaluate the performance of candidate granular flows, to capture the final geometry and materials of the laboratory scale reactor within the high-flux solar simulator, and to evaluate the influence of evolved O_2 transport within the reactor on the chemical reduction of the dense granular flow. A new metric, the energy density storage rate, was proposed for evaluating granular flows in concentrated solar power applications for insight into reactor performance at various scales.

A solar thermochemical inclined granular flow reactor was fabricated and tested within the high flux solar simulator. The system was gradually preheated to temperatures > 1073 K to avoid thermal shock to the granular flow channel. A dense, granular flow of 220 g/min was introduced to a 35° inclined slope upon preheating and additional lamps and lamp powers were increased until near steady state conditions were observed based on outlet granular flow temperatures and O_2 evolution. Steady-state system response was observed for reactor geometry and high-flux solar simulator operating conditions which avoided significant particle agglomerations, promoting directly irradiated and continuous reactor operation. Continuous operation of the reactor using intermittent, dense granular flows was achieved with flow outlet temperatures ranging between 1110 – 1140 K with thermochemical energy storage and a maximum efficiency of nearly 0.7.

Building from these initial studies, there remains further research which could improve the reactor performance.

9.2 Future Work

The design, modeling, and testing of the solar thermochemical inclined granular flow reactor encompassed the work in this dissertation. In the near-term, adjustments could be made to the reactor and high flux solar simulator operating conditions and modeling to improve the reactor performance:

- Preheat particles using heat-tape wrapped hopper to encourage new high flux solar simulator lamp combinations and power levels which further promote uniform irradiation of the dense granular flow.

- Investigation of reactor performance with alternative thermochemical energy storage media, specifically perovskite oxides tuned to reduce at lower temperatures to avoid significant particle agglomeration.
- Introduce absorber plates over the granular flow where localized regions of highly concentrated irradiation are developed along the inclined slope. This would promote a combination of direct and indirect heating of the granular flow, but may permit wider flows for a similar mass flow rate.
- Development of transient heat and mass transfer modeling for the STInGR reactor to capture the intermittent behavior of the granular flows during high temperature operation.

In the long term, the work developed in this dissertation may promote continued research efforts through various pathways:

- Investigation of the solar thermochemical inclined granular flow concept for larger –scale solar concentrating infrastructures which could accommodate wider granular flow channels and thinner granular flows, more uniform irradiation from concentrating infrastructures, and longer slopes for increased flow residence times
- Further investigation into high temperature performance of dense, granular flows to determine how temperature-dependent material properties effect bulk flow handling and the relative importance of frictional – collisional behavior.
- Development of thermochemical energy storage media designed not only to achieve chemical, but granular flow performance criteria to promote bulk material transport at high temperatures. For example, Al_2O_3-supported redox-active metal oxides are currently being investigated [234].

A 100 kW_{th} scale, solar thermochemical inclined granular flow reactor has been designed and fabricated based on the successful design features of the 5 kW_{th} STInGR. Images of the fully-fabricated 100 kW_{th} scale reactor are given in Figure 9.1 including (a) a side-view of the fully fabricated reactor with hopper, collector, and particle recirculation loop, (b) a top-down view of the reactor assembly and secondary concentrator, (c) a view through the windowed aperture detailing the stair-step, interchangeable granular flow channels, and (d) view of insertion of the granular flow channels within the aluminosilicate cavity coated with high-purity alumina.

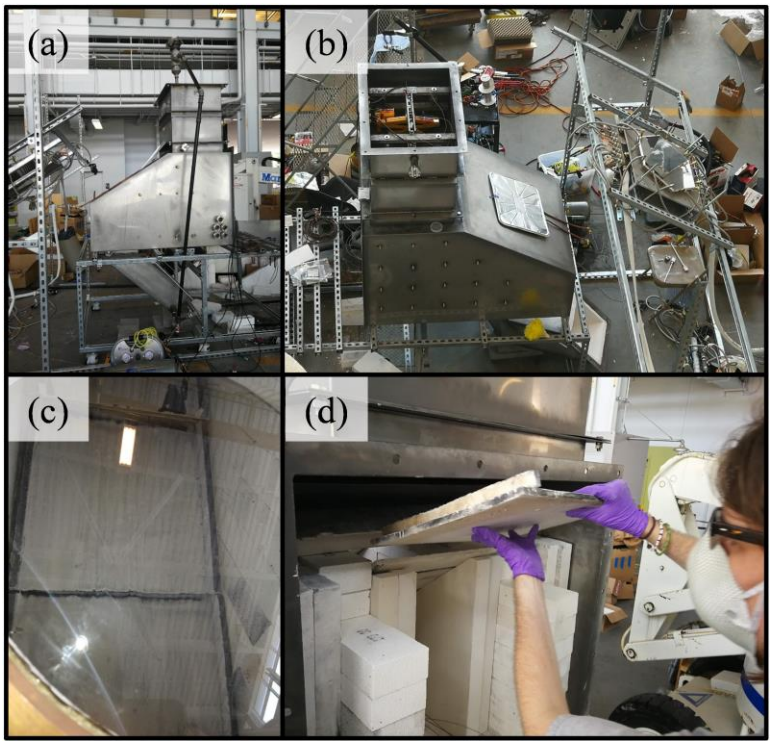

Figure 9.1. Fully fabricated 100 kW_{th} scale reactor with hopper, collector, and particle recirculation loop, (b) a top-down view of the reactor assembly and secondary concentrator, (c) a view through the windowed aperture detailing the stair-step, interchangeable granular flow channels, and (d) view of insertion of the granular flow channels within the aluminosilicate cavity coated with high-purity alumina.

The observed high-temperature agglomeration phenomena observed throughout the course of this research spearheaded the funding of a separate project by the Department of

Energy (DOE) for Topic 2B Gen3 concentrated solar power research initiative entitled, 'Advanced Characterization of Particulate Flows for Concentrating Solar Applications'. From the DOE website,

"*This project will address a knowledge gap within the field of particulate flows for concentrating solar thermal power (CSP) applications. The team will characterize the flow and heat transfer of particulate media over a range of operating conditions, including temperature, particle size, and construction material. Through experimentation and modeling, the team will determine the properties needed for inputs at these high temperatures. These results will provide guidance to the CSP industry for ongoing work related to the design and modeling of solar particle heat receivers and reactors.*"

A modified version of the inclined flow tilt rig used in granular flow characterization (Chapter 7) was proposed to accommodate temperatures ≤ 1073 K to investigate bulk handling characteristics and temperature distributions for varying flow configurations and granular media in concentrated solar power applications. A Solidworks rendering of the proposed high temperature tilt rig is given in Figure 9.2.

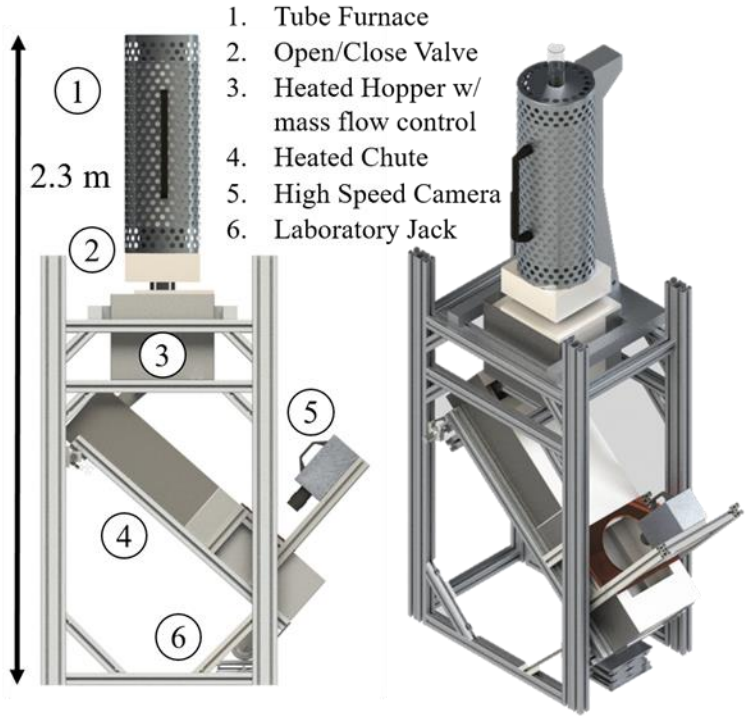

Figure 9.2. Solidworks rendering of high-temperature tilt rig for characterization of granular media bulk transport at temperatures ≤ 1073 K

Lastly, the development of thermochemical energy storage media designed not only for chemical, but mechanical performance would improve the potential of a solar thermochemical inclined granular flow reactor. Carbo Ceramics is a company which has been developing methods for producing granular media for fracking and casting applications, and has recently been employing those same materials for concentrated solar applications (*e.g.* Accucast ID50). Further collaborations with Carbo Ceramics or similar companies should be pursued to modify pre-existing methods to accommodate redox-active metal oxides. Additionally, using inert, mechanically reliable granular media as a support structure for redox-active metal oxides could achieve both the mechanical and chemical requirements for these thermochemical energy storage media.

APPENDIX A. MAPPING MCRT SURFACE/VOLUME PROFILES IN ANSYS FLUENT

The below procedure details the method of mapping MCRT surface irradiation to ANSYS Fluent v19.0.

Steps:

1. Reserve user-defined memory (UDM) locations for storing incident rays via **User Defined > Memory > Number of User-Defined Memory Locations: [1]**.

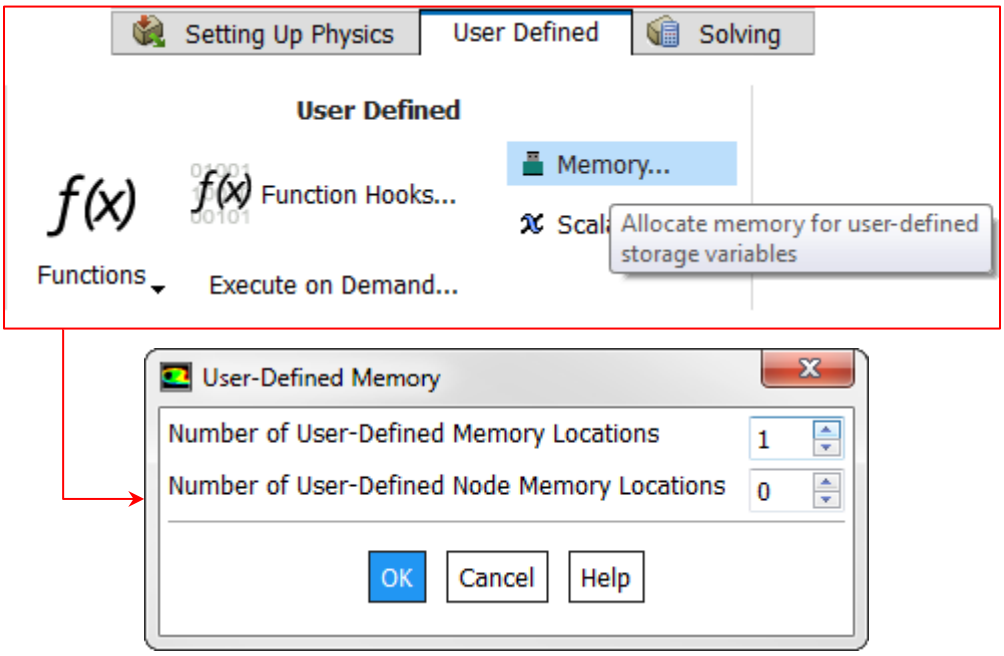

2. Load and compile .c and .h files for UDF via **User Defined > Functions > Compiled >**
   a. (Source Files) Add > [coupleMCRT.c]
   b. (Header Files) Add > [coupleHeader.h]
   c. [Build]
   d. [Load]

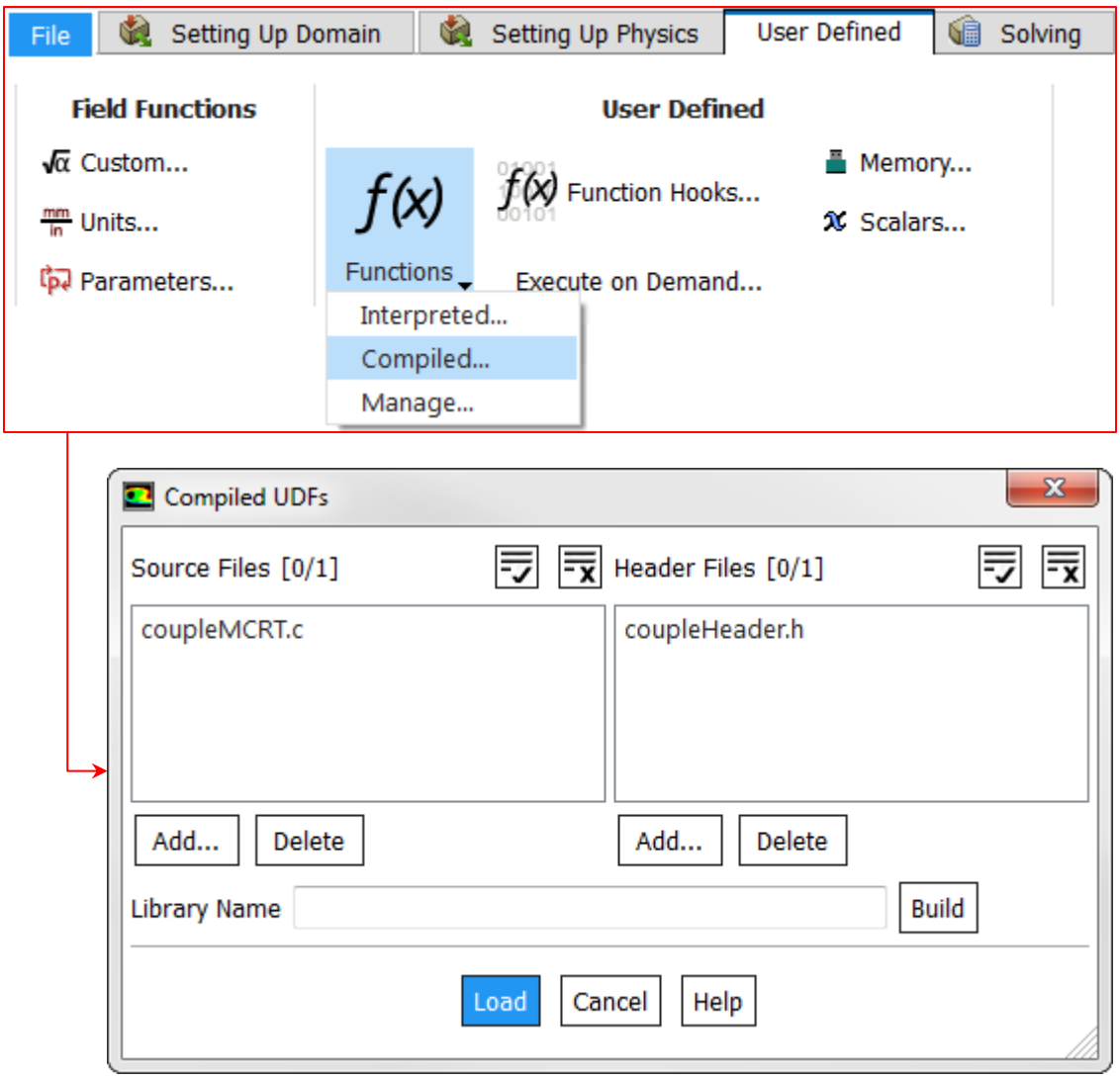
File
Setting Up Domain
Setting Up Physics
User Defined
Solving
Field Functions
Custom...
Units...
Parameters...
User Defined
Functions
Function Hooks...
Execute on Demand...
Memory...
Scalars...
Interpreted...
Compiled...
Manage...
Compiled UDFs
Source Files [0/1]
Header Files [0/1]
coupleMCRT.c
coupleHeader.h
Add...
Delete
Add...
Delete
Library Name
Build
Load
Cancel
Help

3. Integrate the MCRT-CFD mapping procedure into the solution initialization feature as a function hook, via: **User Defined > Function Hooks > (Initialization) Edit: [import_MCRT::libudf] >**
    a. [Add]
    b. [OK]

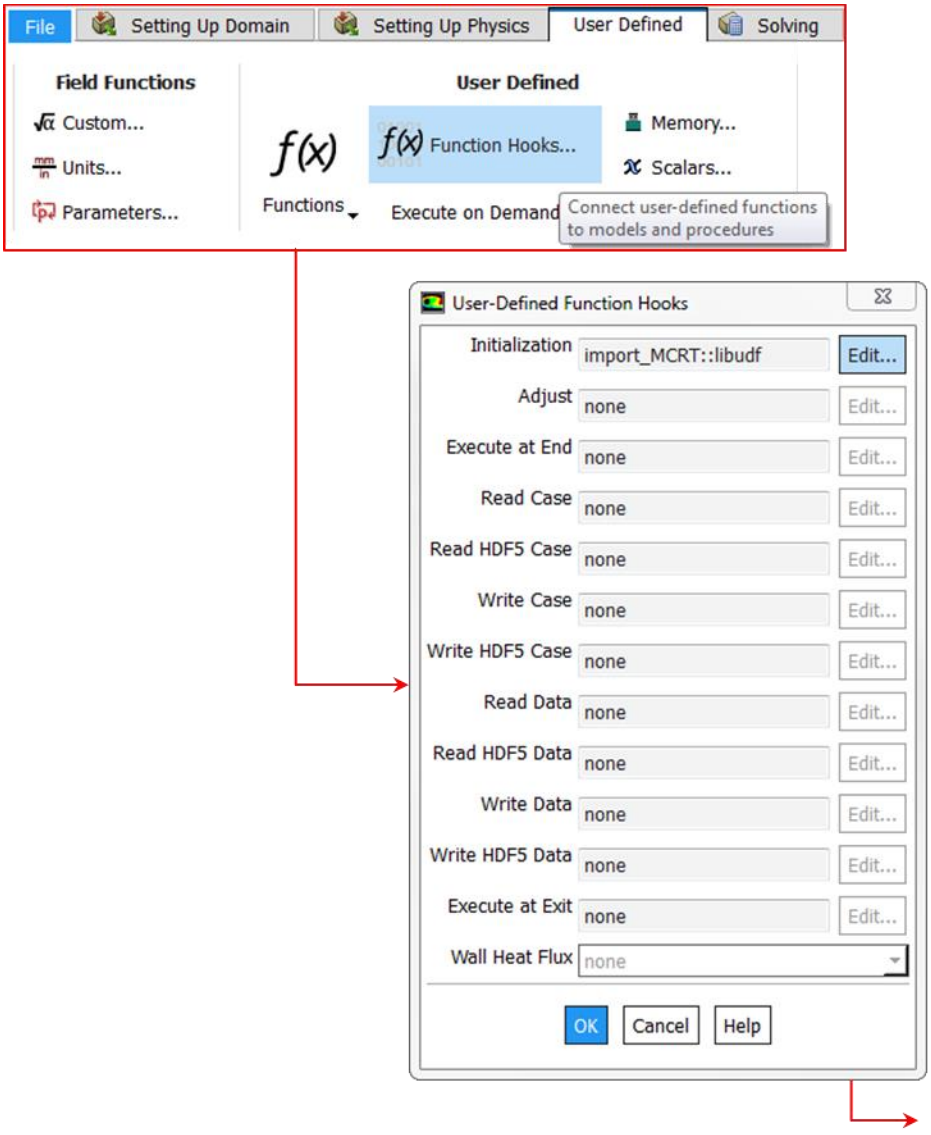

Continued

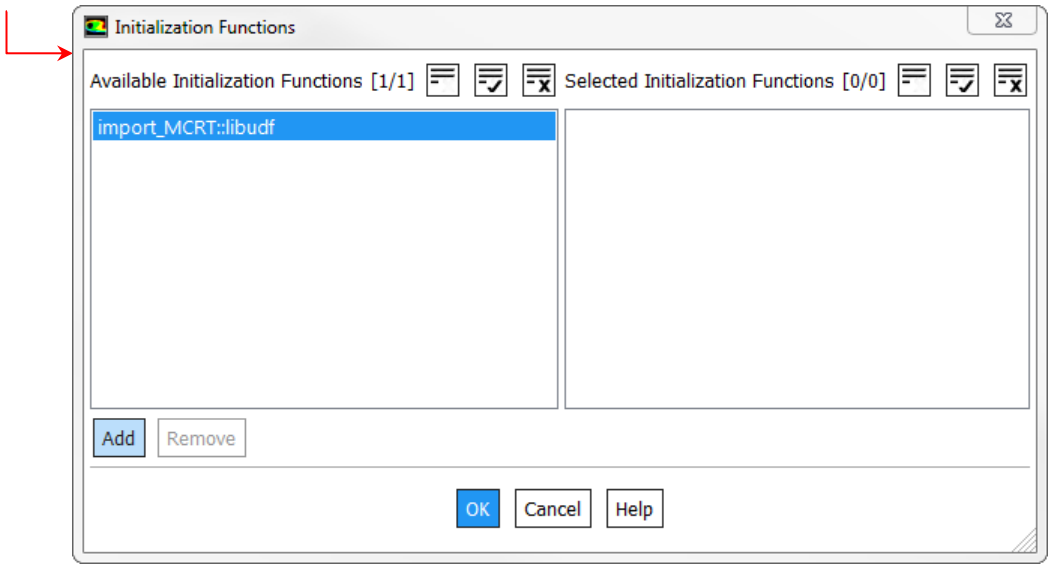

4. Couple the power from incident rays to the thermal energy equation via volumetric boundary source terms, with a boundary thickness defined in the **coupleHeader.h** header file, via **Setup > Boundary Conditions > [irradiated boundary] > Thermal > Heat Generation Rate (W/m3) > [udf absorbed_irradiation::libudf]**.

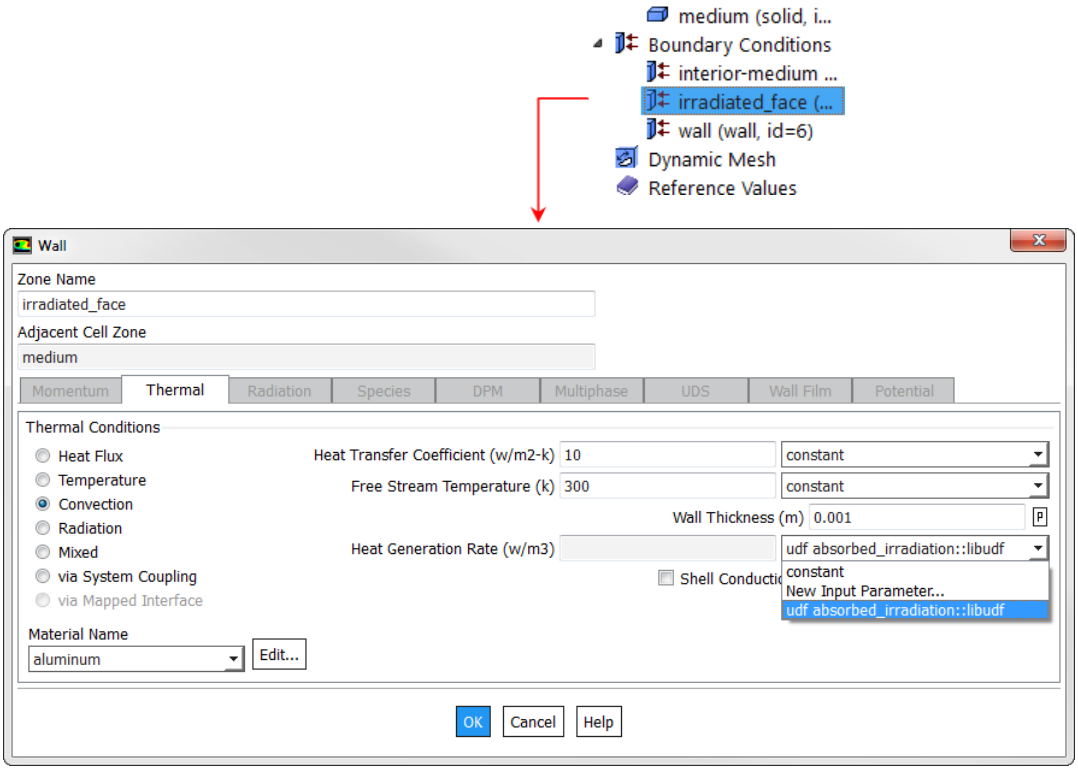

For volumetric mapping, *i.e.* a volumetric source term, the source would instead be included via **Setup > Cell Zone Conditions > [absorbing volume] > Source Terms > Energy > [udf absorbed_radiation_cell::libudf]**, with the Source Terms box checked and the Number of Energy Sources set to [1].

Monte Carlo irradiation data for each surface should be in the form of a space-separated ASCII text file of N lines, where N is the number of ray intersections, and where each line is four decimal numbers long:

$$\begin{matrix} x_1 & y_1 & z_1 & E_1 \\ x_2 & y_2 & z_2 & E_2 \\ \vdots & \vdots & \vdots & \vdots \\ x_N & y_N & z_N & E_N \end{matrix}$$

The file should have neither header nor footer and lines should be generated by a single newline character ("\n"), or manually with the Enter key. The spatial coordinates x_k, y_k, and z_k should be in units of [m] and E_k in units of [W].

REFERENCES

1. *The Sunshot 2030 Goals*, U.S.D.o. Energy, Editor. 2016, Solar Energy Technologies Office.

2. Ho, C.K. and B.D. Iverson, *Review of high-temperature central receiver designs for concentrating solar power.* Renewable and Sustainable Energy Reviews, 2014. **29**: p. 835-846.

3. Steinfeld, A. and R. Palumbo, *Solar Thermochemical Process Technology*, in *Encyclopedia of Physical Science and Technology (Third Edition)*, R.A. Meyers, Editor. 2003, Academic Press: New York. p. 237-256.

4. Weinstein, L.A., et al., *Concentrating Solar Power.* Chemical Reviews, 2015. **115**(23): p. 12797-12838.

5. Pitz-Paal, R., et al., *Concentrating solar power in Europe, the Middle East and North Africa: achieving its potential.* EPJ Web of Conferences, 2012. **33**: p. 03004.

6. Carrillo, A.J., et al., *Revisiting the BaO 2/BaO redox cycle for solar thermochemical energy storage.* Physical Chemistry Chemical Physics, 2016. **18**(11): p. 8039-8048.

7. Wu, S., et al., *A review on high-temperature thermochemical energy storage based on metal oxides redox cycle.* Energy conversion and management, 2018. **168**: p. 421-453.

8. Schrader, A.J., A.P. Muroyama, and P.G. Loutzenhiser, *Solar electricity via an Air Brayton cycle with an integrated two-step thermochemical cycle for heat storage based on Co3O4/CoO redox reactions: Thermodynamic analysis.* Sol. Energy, 2015. **118**: p. 485-495.

9. Pagkoura, C., et al., *Cobalt oxide based structured bodies as redox thermochemical heat storage medium for future CSP plants.* Sol. Energy, 2014. **108**(0): p. 146-163.

10. Carrillo, A.J., et al., *Solar energy on demand: A review on high temperature thermochemical heat storage systems and materials.* Chemical reviews, 2019. **119**(7): p. 4777-4816.

11. Imponenti, L., *Redox cycles with doped calcium manganites for high-temperature thermochemical energy storage in concentrating solar power*. 2018, Colorado School of Mines. Arthur Lakes Library.

12. Gorman, B.T., *A Steady State Thermodynamic Model of Concentrating Solar Power with Thermochemical Energy Storage*. 2017, Arizona State University.

13. Bush, H.E. and P.G. Loutzenhiser, *Solar electricity via an Air Brayton cycle with an integrated two-step thermochemical cycle for heat storage based on Fe2O3/Fe3O4 redox reactions: Thermodynamic and kinetic analyses.* Solar Energy, 2018. **174**: p. 617-627.

14. Wong, B., *Thermochemical Heat Storage for Concentrated Solar Power, Final Report for the US Department of Energy*. 2011: San Diego, CA, USA.

15. Muller, R., P. Haerberling, and R.D. Palumbo, *Further advances toward the development of a direct heating solar thermal chemical reactor for the thermal dissociation of ZnO(s).* Sol. Energy, 2005. **80**: p. 500-511.

16. Palumbo, R., et al., *Reflections on the design of solar thermal chemical reactors: thoughts in transformation.* Energy, 2004. **29**(5–6): p. 727-744.

17. Ermanoski, I., N.P. Siegel, and E.B. Stechel, *A New Reactor Concept for Efficient Solar-Thermochemical Fuel Production.* J. Sol. Energy Eng., 2013. **135**(August 2013).

18. Medrano, M., et al., *State of the art on high-temperature thermal energy storage for power generation. Part 2 -- Case studies.* Renew. Sust. Energ. Rev., 2010. **14**(1): p. 56-72.

19. Ho, C., et al., *Technology advancements for next generation falling particle receivers.* Enrgy Proced., 2014. **49**(0): p. 398-407.

20. Medrano, M., et al., *State of the art on high-temperature thermal energy storage for power generation. Part 2—Case studies.* Renewable and Sustainable Energy Reviews, 2010. **14**(1): p. 56-72.

21. Siegel, N. and G. Kolb. *Design and on-sun testing of a solid particle receiver protype* in *2008 2nd International Conference on Energy Sustainability, ES 2008, August 10, 2008 - August 14, 2008*. 2009. Jacksonville, FL, United states: ASME.

22. Liu, M., W. Saman, and F. Bruno, *Review on storage materials and thermal performance enhancement techniques for high temeprature phase change thermal storage systems.* Renew. Sust. Energ. Rev., 2012. **16**(4): p. 2118-2132.

23. Sharma, A., et al., *Review on storage materials and thermal performance enchancement techniques for high temperature phase change thermal storage systems.* Renew. Sust. Energ. Rev., 2009. **13**(2): p. 318-345.

24. Steinmann, W.D., D. Laing, and R. Tamme, *Development of PCM Storage for Process Heat and Power Generation.* J. Sol. Energy Eng., 2009. **131**(4): p. 041009-041009.

25. Bayón, R., et al., *Analysis of the experimental behaviour of a 100 kWth latent heat storage system for direct steam generation in solar thermal power plants.* Appl. Therm. Eng., 2010. **30**(17–18): p. 2643-2651.

26. Lovegrove, K., A. Luzzi, and H. Kreetz, *A solar-driven ammonia-based thermochemical energy storage system.* Sol. Energy, 1999. **67**(4–6): p. 309-316.

27. Bilgen, E., et al., *Use of solar energy for direct and two-step water decomposition cycles.* Int. J. Hydrogen Energy, 1977. **2**(3): p. 251-257.

28. Fletcher, E.A., *Solarthermal Processing: A Review.* J. Sol. Energy Eng., 2000. **123**(2): p. 63-74.

29. Kodama, T., *High-temperature solar chemistry for converting solar heat to chemical fuels.* Prog. Energy Combust. Sci., 2003. **29**(6): p. 567-597.

30. Loutzenhiser, P.G., A. Meier, and A. Steinfeld, *Review of the Two-Step H20/CO2-Splitting Solar Thermochemical Cycle Based on Zn/ZnO Redox Reactions.* Materials, 2010. **3**(11): p. 4922-4938.

31. Meier, A. and C. Sattler, *Solar Fuels from Concentrated Sunlight*, in *Solar Power and Chemical Energy Systems Implementing Agreement of the International Energy Agency*. 2009, SolarPACES.

32. Neises, M., et al., *Solar-heated rotary kiln for thermochemical energy storage.* Sol. Energy, 2012. **86**(10): p. 3040-3048.

33. Perkins, C. and A.W. Weimer, *Solar-thermal production of renewable hydrogen -- a review.* AIChE J., 2009. **55**(2): p. 286-293.

34. Steinfeld, A., *Solar thermochemical production of hydrogen -- a review.* Sol. Energy, 2005. **78**(5): p. 603-615.

35. Abanades, S., et al., *Screening of water-splitting thermochemical cycles potentially attractive for hydrogen production by concentrated solar energy.* Energy, 2006. **31**(14): p. 2805-2822.

36. Agrafiotis, C., et al., *Exploitation of thermochemical cycles based on solid oxide redox systems for thermochemical storage of solar heat. Part 1: Testing of cobalt oxide-based powders.* Sol. Energy, 2014. **102**(0): p. 189-211.

37. Agrafiotis, C., et al., *Exploitation of thermochemical cycles based on solid oxide redox systems for thermochemical storage of solar heat. Part 3: Cobalt oxide monolithic porous structures as integrated thermochemical reactors/heat exchangers.* Sol. Energy, 2015. **114**: p. 459-475.

38. Karagiannakis, G., et al., *Cobalt/cobaltous oxide based honeycombs for thermochemical heat storage in future concentrated solar power installations:*

Multi-cyclic assessment and semi-quantitative heat effects estimations. Sol. Energy, 2016. **133**: p. 394-407.

39. Babiniec, S.M., et al., *Investigation of LaxSr1−xCoyM1−yO3−δ (M = Mn, Fe) perovskite materials as thermochemical energy storage media.* Solar Energy, 2015. **118**: p. 451-459.

40. McDaniel, A.H., et al., *Sr- and Mn-doped LaAlO3-[small delta] for solar thermochemical H2 and CO production.* Energy & Environmental Science, 2013. **6**(8): p. 2424-2428.

41. Pishahang, M., et al., *Oxygen non-stoichiometry and redox thermodynamics of LaMn1 − xCoxO3 − δ.* Solid State Ionics, 2013. **231**: p. 49-57.

42. Bakken, E., et al., *Redox energetics of perovskite-related La(B1-x;− xB'x)O3 − δ oxides where BB' is FeCo, MnCo, MnNi and CoCu.* Solid State Ionics, 2011. **182**(1): p. 19-23.

43. Scheffe, J.R., D. Weibel, and A. Steinfeld, *Lanthanum–Strontium–Manganese Perovskites as Redox Materials for Solar Thermochemical Splitting of H2O and CO2.* Energy & Fuels, 2013. **27**(8): p. 4250-4257.

44. Babiniec, S.M., et al., *Doped calcium manganites for advanced high-temperature thermochemical energy storage.* International Journal of Energy Research, 2016. **40**(2): p. 280-284.

45. Jing, D., et al., *Effect of Production Parameters on the Spray-Dried Calcium Manganite Oxygen Carriers for Chemical-Looping Combustion.* Energy & Fuels, 2016. **30**(4): p. 3257-3268.

46. Imponenti, L., et al., *Thermochemical energy storage in strontium-doped calcium manganites for concentrating solar power applications.* Solar Energy, 2017. **151**: p. 1-13.

47. Imponenti, L., et al., *Measuring thermochemical energy storage capacity with redox cycles of doped-CaMnO3.* ECS Transactions, 2016. **72**(7): p. 11-22.

48. Imponenti, L., et al., *Redox cycles with doped calcium manganites for thermochemical energy storage to 1000° C.* Applied energy, 2018. **230**: p. 1-18.

49. Hallberg, P., et al., *Chemical Looping Combustion and Chemical Looping with Oxygen Uncoupling Experiments in a Batch Reactor Using Spray-Dried CaMn1–xMxO3−δ (M = Ti, Fe, Mg) Particles as Oxygen Carriers.* Energy & Fuels, 2013. **27**(3): p. 1473-1481.

50. Hallberg, P., et al., *Investigation of a calcium manganite as oxygen carrier during 99h of operation of chemical-looping combustion in a 10kWth reactor unit.* International Journal of Greenhouse Gas Control, 2016. **53**: p. 222-229.

51. Khawam, A. and D.R. Flanagan, *Solid-state kinetic models: Basics and mathematical fundamentals.* Journal of Physical Chemistry B, 2006. **110**(35): p. 17315-17328.

52. Hutchings, K.N., et al., *Kinetic and thermodynamic considerations for oxygen absorption/desorption using cobalt oxide.* Solid State Ionics, 2006. **177**(1–2): p. 45-51.

53. Wong, B., *Thermochemical Heat Storage for Concentrated Solar Power*. 2011. p. 65.

54. Pagkoura, C., et al., *Cobalt oxide based structured bodies as redox thermochemical heat storage medium for future CSP plants.* Solar Energy, 2014. **108**(0): p. 146-163.

55. Berman, A. and M. Epstein, *The kinetics of hydrogen production in the oxidation of liquid zinc with water vapor.* International Journal of Hydrogen Energy, 2000. **25**(10): p. 957-967.

56. Ernst, F.O., A. Steinfeld, and S.E. Pratsinis, *Hydrolysis rate of submicron Zn particles for solar H2 synthesis.* International Journal of Hydrogen Energy, 2009. **34**(3): p. 1166-1175.

57. Möller, S. and R. Palumbo, *Solar thermal decomposition kinetics of ZnO in the temperature range 1950–2400 K.* Chemical Engineering Science, 2001. **56**(15): p. 4505-4515.

58. Perkins, C., P. Lichty, and A.W. Weimer, *Determination of aerosol kinetics of thermal ZnO dissociation by thermogravimetry.* Chemical Engineering Science, 2007. **62**(21): p. 5952-5962.

59. Schunk, L.O. and A. Steinfeld, *Kinetics of the Thermal Dissociation of ZnO Exposed to Concentrated Solar Irradiation Using a Solar-Driven Thermogravimeter in the 1800–2100 K Range.* AIChE J., 2009. **55**(6): p. 1497-1504.

60. Venstrom, L.J. and J.H. Davidson, *The kinetics of the heterogeneous oxidation of zinc vapor by carbon dioxide.* Chemical Engineering Science, 2013. **93**(0): p. 163-172.

61. Loutzenhiser, P.G., et al., *CO2 Splitting via Two-Step Solar Thermochemical Cycles with Zn/ZnO and FeO/Fe3O4 Redox Reactions II: Kinetic Analysis.* Energy Fuels, 2009. **23**: p. 2832-2839.

62. Chambon, M., S. Abanades, and G. Flamant, *Kinetic investigation of hydrogen generation from hydrolysis of SnO and Zn solar nanopowders.* International Journal of Hydrogen Energy, 2009. **34**(13): p. 5326-5336.

63. Levêque, G. and S. Abanades, *Kinetic analysis of high-temperature solid–gas reactions by an inverse method applied to ZnO and SnO2 solar thermal dissociation.* Chemical Engineering Journal, 2013. **217**(0): p. 139-149.

64. Abanades, S., *CO2 and H2O reduction by solar thermochemical looping using SnO2/SnO redox reactions: Thermogravimetric analysis.* International Journal of Hydrogen Energy, 2012. **37**(10): p. 8223-8231.

65. Go, K.S., S.R. Son, and S.D. Kim, *Reaction kinetics of reduction and oxidation of metal oxides for hydrogen production.* International Journal of Hydrogen Energy, 2008. **33**(21): p. 5986-5995.

66. Gálvez, M.E., et al., *Solar hydrogen production via a two-step thermochemical process based on MgO/Mg redox reactions—Thermodynamic and kinetic analyses.* International Journal of Hydrogen Energy, 2008. **33**(12): p. 2880-2890.

67. Botas, J.A., et al., *Kinetic modelling of the first step of Mn2O3/MnO thermochemical cycle for solar hydrogen production.* International Journal of Hydrogen Energy, 2012. **37**(24): p. 18661-18671.

68. Francis, T.M., P.R. Lichty, and A.W. Weimer, *Manganese oxide dissociation kinetics for the Mn2O3 thermochemical water-splitting cycle. Part 1: Experimental.* Chemical Engineering Science, 2010. **65**(12): p. 3709-3717.

69. McDaniel, A.H., et al., *Nonstoichiometric Perovskite Oxides for Solar Thermochemical H2 and CO Production.* Energy Procedia, 2014. **49**(0): p. 2009-2018.

70. Kostoglou, M., S. Lorentzou, and A.G. Konstandopoulos, *Improved kinetic model for water splitting thermochemical cycles using Nickel Ferrite.* International Journal of Hydrogen Energy, 2014. **39**(12): p. 6317-6327.

71. Neises, M., et al., *Kinetic investigations of the hydrogen production step of a thermochemical cycle using mixed iron oxides coated on ceramic substrates.* International Journal of Energy Research, 2010. **34**(8): p. 651-661.

72. Scheffe, J.R., et al., *Kinetics and mechanism of solar-thermochemical H2 production by oxidation of a cobalt ferrite-zirconia composite.* Energy & Environmental Science, 2013. **6**(3): p. 963-973.

73. Agrafiotis, C., M. Roeb, and C. Sattler, *A review on solar thermal syngas production via redox pair-based water/carbon dioxide splitting thermochemical cycles.* Renewable and Sustainable Energy Reviews, 2015a. **42**(0): p. 254-285.

74. Muller, R., P. Haeberling, and R.D. Palumbo, *Further advances toward the development of a direct heating solar thermal chemical reactor for the thermal dissociation of ZnO(s).* Sol. Energy, 2005. **80**: p. 500-511.

75. Schunk, L.O., et al., *A Receiver - Reactor for the Solar Thermal Dissociation of Zinc Oxide.* J. Sol. Energ. Eng., 2008. **130**(May 2008).

76. Villasmil, W., et al., *Pilot scale demonstration of a 100-kWth solar thermochemical plant for the thermal dissociation of ZnO.* J. Sol. Energ. Eng., 2014. **136**(1).

77. Anton Meier , E.B., Gian Mario Cella , Wojciech Lipinski , Daniel Wuillemin , Robert Palumbo, *Design and experimental investigation of a horizontal rotary reactor for the solar thermal production of lime.* Energy, 2003. **29**: p. 811-821.

78. Meier, A., et al., *Multitube rotary kiln for the industrial solar production of lime.* J. Sol. Energ. Eng., 2005. **127**(3): p. 386-395.

79. Meier, A., et al., *Solar chemical reactor technology for industrial production of lime.* Sol. Energy, 2006. **80**(10): p. 1355-1362.

80. Ermanoski, I. and N. Siegel, *Annual average efficiency of a solar-thermochemical reactor.* Enrgy Proced., 2013. **49**: p. 1932-1939.

81. Bellan, S., et al., *Thermal performance of lab-scale solar reactor designed for kinetics analysis at high radiation fluxes.* Chem. Eng. Sci., 2013. **101**: p. 81-89.

82. Rodat, S., et al., *A pilot-scale solar reactor for the production of hydrogen and carbon black from methane splitting.* Int. J. Hydrogen Energ., 2010. **35**(15): p. 7748-58.

83. Hirsch, D. and A. Steinfeld, *Solar hydrogen production by thermal decomposition of natural gas using a vortex-flow reactor.* Int. J. Hydrogen Energ., 2004. **29**(1): p. 47-55.

84. Rodat, S., S. Abanades, and G. Flamant, *Methane decarbonization in indirect heating solar reactors of 20 and 50 kW for a CO2-free production of hydrogen and carbon black.* Journal of Solar Energy Engineering, Transactions of the ASME, 2011. **133**(3).

85. Tescari, S., et al., *Experimental evaluation of a pilot-scale thermochemical storage system for a concentrated solar power plant.* Appl. Energ., 2017. **189**: p. 66-75.

86. Siegel, N. and G. Kolb. *Design and on-sun testing of a solid particle receiver prototype*. in *2008 2nd International Conference on Energy Sustainability, ES 2008, August 10, 2008 - August 14, 2008*. 2009. Jacksonville, FL, United states: ASME.

87. Ho, C., et al., *Technology advancements for next generation falling particle receivers.* Enrgy Proced., 2013. **49**: p. 398-407.

88. Steinfeld, A., *Solar thermochemical production of hydrogen—a review.* Sol. Energy, 2005. **78**(5): p. 603-615.

89. Koepf, E.E., S.G. Advani, and A.K. Prasad, *A novel beam-down, gravity fed, solar thermochemical receiver/reactor for direct solid particle decomposition: Design, modeling, and experimentation.* Int. J. Hydrogen Energ., 2012. **37**: p. 16871-16887.

90. Patankar, S., *Numerical heat transfer and fluid flow*. 1980: CRC press.

91. Anderson, D., J. Tannehill, and R. Pletcher, *Computational Fluid Mechanics and Heat Transfer, series in computational methods in mechanics and thermal sciences second edition*. Taylor and Francis.

92. *ANSYS Fluent*. 2013, ANSYS, Inc.: Canonsburg, PA.

93. Schunk, L., W. Lipiński, and A. Steinfeld, *Heat transfer model of a solar receiver-reactor for the thermal dissociation of ZnO—Experimental validation at 10kW and scale-up to 1MW.* Chem. Eng. J., 2009. **150**(2): p. 502-508.

94. Villafán-Vidales, H.I., et al., *Monte Carlo radiative transfer simulation of a cavity solar reactor for the reduction of cerium oxide.* Int. J. Hydrogen Energ., 2009. **34**(1): p. 115-124.

95. Villafán-Vidales, H., et al., *Radiative heat transfer analysis of a directly irradiated cavity-type solar thermochemical reactor by Monte-Carlo ray tracing.* J. Renew. Sust. Energy, 2012. **4**(4): p. 043125.

96. Abanades, S., P. Charvin, and G. Flamant, *Design and simulation of a solar chemical reactor for the thermal reduction of metal oxides: Case study of zinc oxide dissociation.* Chem. Eng. Sci., 2007. **62**(22): p. 6323-6333.

97. Hathaway, B.J., W. Lipiński, and J.H. Davidson, *Heat Transfer in a Solar Cavity Receiver: Design Considerations.* Numer. Heat Tr. A-Appl., 2012. **62**(5): p. 445-461.

98. Lapp, J., J.H. Davidson, and W. LipiĹ, *Heat transfer analysis of a solid-solid heat recuperation system for solar-driven nonstoichiometric redox cycles.* J. Sol. Energ. Eng., 2013. **135**(3): p. 031004.

99. Lapp, J. and W. LipiĹ, *Transient three-dimensional heat transfer model of a solar thermochemical reactor for H2O and CO2 splitting via nonstoichiometric ceria redox cycling.* J. Sol. Energ. Eng., 2014. **136**(3): p. 031006.

100. Müller, R., W. Lipiński, and A. Steinfeld, *Transient heat transfer in a directly-irradiated solar chemical reactor for the thermal dissociation of ZnO.* Appl. Therm. Eng., 2008. **28**(5): p. 524-531.

101. Muroyama, A., et al., *Modeling of a Dynamically-Controlled Hybrid Solar/Autothermal Steam Gasification Reactor.* Energy & Fuels, 2014. **28**(10): p. 6520-6530.

102. Modest, M.F., *Radiative Heat Transfer*. 3rd ed. 2013, Oxford, UK: Academic Press. 882.

103. ANSYS, *ANSYS Fluent*. 2017, ANSYS, Inc.: Canonsburg, PA.

104. Mecit, A.M. and F. Miller, *A Comparison Between the Monte Carlo Ray Trace and the FLUENT Discrete Ordinates Methods for Treating Solar Input to a Particle Receiver.* 2014(45868): p. V001T02A013.

105. Craig, K.J., et al., *Finite-volume ray tracing using Computational Fluid Dynamics in linear focus CSP applications.* Appl. Energ., 2016. **183**: p. 241-256.

106. Wang, F., et al., *Thermal performance analyses of porous media solar receiver with different irradiative transfer models.* International Journal of Heat and Mass Transfer, 2014. **78**: p. 7-16.

107. Mecit, A.M. and F. Miller. *Optical analysis of a window for solar receivers using the Monte Carlo ray trace method*. in *ASME 2013 7th International Conference on Energy Sustainability collocated with the ASME 2013 Heat Transfer Summer Conference and the ASME 2013 11th International Conference on Fuel Cell Science, Engineering and Technology*. 2013. American Society of Mechanical Engineers.

108. Evan Bush, H., et al., *Design and Characterization of a Novel Upward Flow Reactor for the Study of High-Temperature Thermal Reduction for Solar-Driven Processes.* Journal of Solar Energy Engineering, 2017. **139**(5): p. 051004-051004-11.

109. Schrader, A.J., et al., *Solar electricity via an Air Brayton cycle with an integrated two-step thermochemical cycle for heat storage based on Co3O4/CoO redox reactions III: Solar thermochemical reactor design and modeling.* Solar Energy, 2017. **150**: p. 584-595.

110. Qiu, Y., et al., *A comprehensive model for opitcal and thermal characterization of a linear Fresnel solar reflector with a trapezoidal cavity receiver.* Renewable Energy, 2016. **97**: p. 129-144.

111. Qiu, Y., et al., *Study on optical and thermal perforamance of a linear Fresnel solar reflector using molten salt as HTF with MCRT and FVM methods.* Appl. Energ., 2015. **146**: p. 162-173.

112. He, Y.-L., et al., *A MCRT and FVM coupled simulation method for energy conversion process in parabolic trough solar collector.* Renewable Energy, 2010. **36**: p. 976-985.

113. Lapp, J., J.H. Davidson, and W. Lipiński, *Heat Transfer Analysis of a Solid-Solid Heat Recuperation System for Solar-Driven Nonstoichiometric Redox Cycles.* Journal of Solar Energy Engineering, 2013. **135**(3): p. 031004-031004-11.

114. Koepf, E., et al., *A novel beam-down, gravity-fed, solar thermochemical receiver/reactor for direct solid particle decomposition: Design, modeling, and experimentation.* International Journal of Hydrogen Energy, 2012. **37**(22): p. 16871-16887.

115. Alonso, E. and M. Romero, *A directly irradiated solar reactor for kinetic analysis of non-volatile metal oxides reductions.* International Journal of Energy Research, 2015. **39**(9): p. 1217-1228.

116. Andreotti, B., Y. Forterre, and O. Pouliquen, *Granular media: between fluid and solid*. 2013: Cambridge University Press.

117. Forterre, Y. and O. Pouliquen, *Flows of dense granular media.* Annu. Rev. Fluid Mech., 2008. **40**: p. 1-24.

118. MiDi, G., *On dense granular flows.* Eur. Phys. J. , 2004. **14**: p. 341-365.

119. Gregg, D.W., et al., *Solar coal gasification.* Solar Energy, 1980. **24**(3): p. 313-321.

120. Taylor, R.W., R. Berjoan, and J.P. Coutures, *Solar gasification of carbonaceous materials.* Solar Energy, 1983. **30**(6): p. 513-525.

121. Ho, C., et al., *Technology advancements for next generation falling particle receivers.* Energy Procedia, 2014. **49**: p. 398-407.

122. Ho, C.K., et al. *Performance evaluation of a high-temperature falling particle receiver*. in *ASME 2016 10th International Conference on Energy Sustainability collocated with the ASME 2016 Power Conference and the ASME 2016 14th International Conference on Fuel Cell Science, Engineering and Technology*. 2016. American Society of Mechanical Engineers.

123. Ho, C.K., et al. *On-sun testing of an advanced falling particle receiver system*. in *AIP Conference Proceedings*. 2016. AIP Publishing.

124. Siegel, N.P., et al., *Development and evaluation of a prototype solid particle receiver: on-sun testing and model validation.* Journal of solar energy engineering, 2010. **132**(2): p. 021008.

125. Moller, S. and R. Palumbo, *The development of a solar chemical reactor for the direct thermal dissociation of zinc oxide.* TRANSACTIONS-AMERICAN SOCIETY OF MECHANICAL ENGINEERS JOURNAL OF SOLAR ENERGY ENGINEERING, 2001. **123**(2): p. 83-90.

126. Koepf, E.E., et al., *Experimental Investigation of the Carbothermal Reduction of ZnO Using a Beam-Down, Gravity-Fed Solar Reactor.* Industrial & Engineering Chemistry Research, 2015. **54**(33): p. 8319-8332.

127. Singh, A., et al., *Design of a pilot scale directly irradiated, high temperature, and low pressure moving particle cavity chamber for metal oxide reduction.* Solar Energy, 2017. **157**: p. 365-376.

128. Xiao, G., et al., *Optical and thermal performance of a high-temperature spiral solar particle receiver.* Solar Energy, 2014. **109**: p. 200-213.

129. Pouliquen, O., *Scaling laws in granular flows down rough inclined planes.* Phys. Fluids, 1999. **11**(3): p. 542-548.

130. Pouliquen, O. and F. Chevoir, *Dense flows of dry granular material.* CR Phys, 2002. **3**(2): p. 163-175.

131. Pouliquen, O. and Y. Forterre, *Friction law for dense granular flows: application to the motion of a mass down a rough inclined plane.* Journal of fluid mechanics, 2002. **453**: p. 133-151.

132. Forterre, Y. and O. Pouliquen, *Long-surface-wave instability in dense granular flows.* J. Fluid Mech., 2003. **483**: p. 21 - 50.

133. Loutzenhiser, P.G. and A. Steinfeld, *Solar syngas production from CO2 and H2O in a two-step thermochemical cycle via Zn/ZnO redox reactions: Thermodynamic cycle analysis.* Int. J. Hydrogen Energy, 2011. **36**(19): p. 12141-12147.

134. Lovegrove, K., et al., *Exergy Analysis of Ammonia-Based Solar Thermochemical Power Systems.* Sol. Energy, 1999. **66**(2): p. 103-115.

135. Mahfuz, M.H., et al., *Exergetic analysis of a solar thermal power system with PCM storage.* Energy Convers. Manage., 2014. **78**(0): p. 486-492.

136. Sturzenegger, M. and P. Nüesch, *Efficiency analysis for a manganese-oxide-based thermochemical cycle.* Energy, 1999. **24**(11): p. 959-970.

137. Xu, C., et al., *Energy and exergy analysis of solar power tower plants.* Appl. Therm. Eng., 2011. **31**(17–18): p. 3904-3913.

138. Roine, A., *HSC chemistry*. 2002: Finland: Outokumpu Res Oy.

139. Moran, M. and H. Shapiro, *Fundamentals of Engineering Thermodynamics*. 4 ed. 2000, New York: John Wiley and Sons, Inc.

140. Hischier, I., P. Leumann, and A. Steinfeld, *Experimental and numerical analyses of a pressurized air receiver for solar-driven gas turbines.* Sol. Energy, 2012. **134**(2).

141. Z'Graggen, A. and A. Steinfeld, *Radiative Exchange Within a Two-Cavity Configuration With a Spectrally Selective Window.* J. Sol. Energy Eng., 2004. **126**(2): p. 819-822.

142. Loutzenhiser, P.G., O. Tuerk, and A. Steinfeld, *Production of Si by vacuum carbothermal reduction of SiO2 using concentrated solar energy.* JOM, 2010. **62**(9): p. 49-54.

143. Maag, G., C. Falter, and A. Steinfeld, *Temperature of a Quartz/Sapphire Window in a Solar Cavity-Receiver.* J. Sol. Energy Eng., 2010. **133**(1): p. 014501-014501.

144. Loutzenhiser, P.G. and A. Steinfeld, *Solar syngas production from CO2 and H2O in a two-step thermochemical cycle via Zn/ZnO redox reactions: Thermodynamic cycle analysis.* International Journal of Hydrogen Energy, 2011. **36**(19): p. 12141-12147.

145. Steinfeld, A., *Solar hydrogen production via a two-step water-splitting thermochemical cycle based on Zn/ZnO redox reactions.* Int. J. Hydrogen Energy, 2002. **27**(6): p. 611-619.

146. Schunk, L.O., et al., *A Receiver-Reactor for the Solar Thermal Dissociation of Zinc Oxide.* J. Sol. Energy Eng., 2008. **130**(2): p. 021009-021009.

147. Steinfeld, A. and R. Palumbo, *Solar Thermochemical Process Technology*, in *Encyclopedia of Physical Science and Technology*, R.A. Meyers, Editor. 2001, Academic Press. p. 237-256.

148. Alper, J.S. and R.I. Gelb, *Standard errors and confidence intervals in nonlinear regression: comparison of Monte Carlo and parametric statistics.* The Journal of Physical Chemistry, 1990. **94**(11): p. 4747-4751.

149. *MATLAB*. 2012, MathWorks.

150. Gleser, L.J., *Assessing Uncertainty in Measurement.* Statistical Science, 1998. **13**(3): p. 277-290.

151. Khawam, A. and D.R. Flanagan, *Solid-state kinetic models: basics and mathematical fundamentals.* J Phys Chem B, 2006. **110**(35): p. 17315-28.

152. Vyazovkin, S., et al., *ICTAC Kinetics Committee recommendations for performing kinetic computations on thermal analysis data.* Thermochimica Acta, 2011. **520**(1–2): p. 1-19.

153. Roine, A., *HSC Chemistry*. 2011, Outokumpu Res Oy: Finland.

154. Malinin, G.V. and Y.M. Tolmachev, *Thermal Decomposition of Solid Metal Oxides.* Russian Chemical Reviews, 1975. **44**(5): p. 6.

155. Mills, P., D. Loggia, and M. Tixier, *Model for a stationary dense granular flow along an inclined wall.* Europhys. Lett., 1999. **45**: p. 733-738.

156. Bradley, N., *The response surface methodology*. 2007, Indiana University South Bend.

157. Klein, C.A., *Characteristic strength, Weibull modulus, and failure probability of fused silica glass.* Opt. Eng., 2009. **48**(11): p. 113401-113401-10.

158. Saung, E.-F. and F. Miller. *Dome Window Geometry for a Large Scale Solar Receiver*. in *ASME 2013 7th International Conference on Energy Sustainability collocated with the ASME 2013 Heat Transfer Summer Conference and the ASME 2013 11th International Conference on Fuel Cell Science, Engineering and Technology*. 2013. American Society of Mechanical Engineers.

159. Mande, O. and F. Miller, *Window Design for a Small Particle Solar Receiver.* IECEC 2011, 2011.

160. Saung, E. and F.J. Miller, *Dome Window and Mount Design for a 5 MWth Solar Receiver.* Enrgy Proced., 2014. **49**: p. 514-523.

161. DassaultSystemes, *Solidworks*. 2016, Dassault Systemes.

162. Gill, R., et al., *Characterization of a 6 kW high-flux solar simulator with an array of xenon arc lamps capable of concentrations of nearly 5000 suns.* Rev. Sci. Instrum., 2015. **86**(12): p. 125107.

163. Sih, S.S. and J.W. Barlow, *The prediction of the emissivity and thermal conductivity of powder beds.* Particul. Sci. Technol., 2004. **22**(4): p. 427-440.

164. Mahan, J.R., *Radiation heat transfer: a statistical approach*. Vol. 1. 2002: John Wiley & Sons.

165. Campbell, C.S., *Rapid granular flows.* Annu. Rev. Fluid Mech., 1990. **22**(1): p. 57-90.

166. Silbert, L., J. Landry, and G. Grest, *Granular flow down a rough inclined plane: Transition between thin and thick piles.* Phys. Fluids, 2003. **15**.

167. Jenkins, J. and S. Savage, *A theory for the rapid flow of identical, smooth, nearly elastic, spherical particles.* Journal of Fluid Mechanics, 1983. **130**: p. 187-202.

168. Ancey, C., *Dry granular flows down an inclined channel: Experimental investigations on the frictional-collisional regime.* Phys. Rev. E, 2002. **65**(1; PART 1): p. 011304-011304.

169. Jakobsen, H.A., *Chemical Reactor Modeling: Multiphase Reactive Flows*. Second ed. 2014, Switzerland: Springer International

170. Kaviany, M., *Principles of Heat Transfer in Porous Media*. Second Edition ed. Mechanical Engineering Series. 1995, New York: Springer.

171. Lipinski, W. and A. Steinfeld, *Heterogeneous thermochemical decomposition under direct irradiation.* Int. J. Heat Mass. Tran., 2004. **47**(8–9): p. 1907-1916.

172. Tsotsas, E. and H. Martin, *Thermal conductivity of packed beds: a review.* Chem. Eng. Process., 1987. **22**(1): p. 19-37.

173. Botterill, J., A. Salway, and Y. Teoman, *The effective thermal conductivity of high temperature particulate beds—II. Model predictions and the implication of the experimental values.* Int. J. Heat Mass. Tran., 1989. **32**(3): p. 595-609.

174. Marti, J., M. Roesle, and A. Steinfeld, *Experimental Determination of the Radiative Properties of Particle Suspensions for High-Temperature Solar Receiver Applications.* Heat Transfer Eng., 2013. **35**(3): p. 272-280.

175. Tien, C., *Thermal radiation in packed and fluidized beds.* ASME J. Heat Transfer, 1988. **110**(4): p. 1230-1242.

176. Modest, M.F., *Radiative Heat Transfer*. Second ed. 2003, San Diego, CA: Academic Press.

177. Linstrom, P.J. and W.G. Mallard, *NIST Chemistry WebBook*. NIST Standard Reference Database Number 69. 2016, Gaithersburg MD: National Institute of Standards and Technology.

178. Muroyama, A.P., A.J. Schrader, and P.G. Loutzenhiser, *Solar electricity via an Air Brayton cycle with an integrated two-step thermochemical cycle for heat storage based on Co3O4/CoO redox reactions II: Kinetic analyses.* Sol. Energy, 2015. **122**: p. 409-418.

179. Bergman, T.L., et al., *Introduction to Heat Transfer*. Sixth ed. 2011: John Wiley and Sons, Inc.

180. Howell, J.R., R. Siegel, and M.P. Menguc, *Thermal radiation heat transfer*. 2010: CRC press.

181. Powell, R.W., C.Y. Ho, and P.E. Liley, *Thermal Conductivity of Selected Materials*, in *National Standard Reference Data System*. 1966, National Bureau of Standards: West Lafayette, Indiana.

182. Shamlou, P., *Handling of Bulk Solids: Theory and Practice*. 2013: Elsevier.

183. Montgomery, D.C. and G.C. Runger, *Applied Statistics and Probability for Engineers*. Fifth ed. 2011: John Wiley and Sons, Inc.

184. MathWorks, *stepwiseglm: create generalized linear regression model by stepwise regression*. 2016.

185. *Thermal Properties.* 2015.

186. Dai, G.-L., X.-L. Xia, and G.-F. Hou, *Transmission performances of solar windows exposed to concentrated sunlight.* Solar Energy, 2014. **103**: p. 125-133.

187. Yong, S., et al., *Radiative properties of a solar cavity receiver/reactor with quartz window.* International journal of hydrogen energy, 2011. **36**(19): p. 12148-12158.

188. Müller, R. and A. Steinfeld, *Band-approximated radiative heat transfer analysis of a solar chemical reactor for the thermal dissociation of zinc oxide.* Solar Energy, 2007. **81**(10): p. 1285-1294.

189. Cunsolo, S., et al., *Monte Carlo determination of radiative properties of metal foams: Comparison between idealized and real cell structures.* International Journal of Thermal Sciences, 2015. **87**: p. 94-102.

190. Wei, G., et al., *Experimental study on the radiative properties of open-cell porous ceramics.* Solar Energy, 2017. **149**: p. 13-19.

191. Cui, F.Q., et al., *Numerical simulations of the solar transmission process for a pressurized volumetric receiver.* Energy, 2012. **46**(1): p. 618-628.

192. Li, Y., et al., *Pore-level determination of spectral reflection behaviors of high-porosity metal foam sheets.* Infrared Physics & Technology, 2018. **89**: p. 77-87.

193. Akolkar, A. and J. Petrasch, *Tomography based pore-level optimization of radiative transfer in porous media.* International Journal of Heat and Mass Transfer, 2011. **54**(23): p. 4775-4783.

194. Marti, J., M. Roesle, and A. Steinfeld, *Combined Experimental-Numerical Approach to Determine Radiation Properties of Particle Suspensions.* Journal of Heat Transfer, 2014. **136**(9): p. 092701.

195. Marti, J., M. Roesle, and A. Steinfeld, *Experimental determination of the radiative properties of particle suspensions for high-temperature solar receiver applications.* Heat Transfer Engineering, 2014. **35**(3): p. 272-280.

196. Tien, C.L., *Thermal Radiation in Packed and Fluidized Beds.* Journal of Heat Transfer, 1988. **110**(4b): p. 1230-1242.

197. Gill, R., et al., *Characterization of a 6 kW high-flux solar simulator with an array of xenon arc lamps capable of concentrations of nearly 5000 suns.* Review of Scientific Instruments, 2015. **86**(12): p. 8.

198. Bush, H.E., et al., *Design and Characterization of a Novel Upward Flow Reactor for the Study of High-Temperature Thermal Reduction for Solar-Driven Processes.* Journal of Solar Energy Engineering, 2017. **139**(5): p. 051004-051004-11.

199. Nguyen, T., C. Brennen, and R. Sabersky, *Funnel flow in hoppers.* Journal of Applied Mechanics, 1980. **47**(4): p. 729-735.

200. Maynard, E., *Ten steps to an effective bin design.* CEP, American Society of Chemical Engineers: Tyngsboro, MA, USA, 2013: p. 25-32.

201. Beverloo, W.A., H.A. Leniger, and J. van de Velde, *The flow of granular solids through orifices.* Chemical Engineering Science, 1961. **15**(3): p. 260-269.

202. Al-Din, N. and D. Gunn, *The flow of non-cohesive solids through orifices.* Chemical engineering science, 1984. **39**(1): p. 121-127.

203. de Ligny, D. and P. Richet, *High-temperature heat capacity and thermal expansion of SrTiO 3 and SrZrO 3 perovskites.* Physical Review B, 1996. **53**(6): p. 3013.

204. Babiniec, S.M., et al. *ABO3 (A= La, Ba, Sr, K; B= Co, Mn, Fe) perovskites for thermochemical energy storage*. in *AIP Conference Proceedings*. 2016. AIP Publishing.

205. Bush, H.E., R. Datta, and P.G. Loutzenhiser, *Aluminum-doped strontium ferrites for a two-step solar thermochemical air separation cycle: Thermodynamic characterization and cycle analysis.* Solar Energy, 2019. **188**: p. 775-786.

206. Ho, C.K., et al., *Characterization of Particle Flow in a Free-Falling Solar Particle Receiver.* Journal of Solar Energy Engineering, 2016. **139**(2): p. 021011-021011-9.

207. Jesuthasan, N., B.R. Baliga, and S.B. Savage, *Use of particle tracking velocimetry for measurements of granular flows: review and application.* KONA Powder and Particle Journal, 2006. **24**: p. 15-26.

208. Thielicke, W. and E.J. Stamhuis, *PIVlab--Towards User-friendly, Affordable and Accurate Digital particle Image Velocimetry in MATLAB.* Journal of Open Research Software, 2014.

209. Figliola, R.S. and D.E. Beasley, *Theory and design for mechanical measurements*. 2014: John Wiley & Sons.

210. Dolgunin, V.N., A.N. Kudy, and A.A. Ukolov, *Development of the model of segregation of particles undergoing granular flow down an inclined chute.* Powder Technology, 1998. **96**(3): p. 211-218.

211. Pouliquen, O. and W. Vallance, *Segregation induced instabilities of granular fronts.* Chaos: An Interdisciplinary Journal of Nonlinear Science, 1999. **9**(3): p. 621-630.

212. Savage, S.B. and L.C.K. K., *Particle size segregation in inclined chute flow of dry cohesionless granular solids.* Journal of Fluid Mechanics, 1988. **189**: p. 311-335.

213. Rognon, P.G., et al., *Dense flows of bidisperse assemblies of disks down an inclined plane.* Physics of Fluids, 2007. **19**(5): p. 058101.

214. ANSYS, *" ANSYS Fluent," ANSYS, Inc., Canonsburg, PA.* 2017.

215. Brewster, R., et al., *Plug flow and the breakdown of Bagnold scaling in cohesive granular flows.* Physical Review E, 2005. **72**(6): p. 061301.

216. Brewster, R., et al., *Relationship between interparticle contact lifetimes and rheology in gravity-driven granular flows.* Physical Review E, 2008. **77**(6): p. 061302.

217. Rognon, P.G., et al., *Rheology of dense snow flows: Inferences from steady state chute-flow experiments.* Journal of Rheology, 2008. **52**(3): p. 729-748.

218. Ehrenreich, H. and H. Philipp, *Optical properties of Ag and Cu.* Physical Review, 1962. **128**(4): p. 1622.

219. Cheng, Q., P. Yang, and Z. Zhang, *Radiative Properties of Ceramic $$\hbox {Al}_{2}\hbox {O}_{3}$$Al2O3, AlN, and $$\hbox {Si}_{3}\hbox {N}_{4}$$Si3N4: I. Experiments.* International Journal of Thermophysics, 2016. **37**(6): p. 62.

220. Siegel, N., et al., *Physical properties of solid particle thermal energy storage media for concentrating solar power applications.* Energy Procedia, 2014. **49**(1): p. 1015-1023.

221. Tawfik, M., X. Tonnellier, and C. Sansom, *Light source selection for a solar simulator for thermal applications: A review.* Renewable and Sustainable Energy Reviews, 2018. **90**: p. 802-813.

222. Versteeg, H.K. and W. Malalasekera, *An introduction to computational fluid dynamics: the finite volume method*. 2007: Pearson education.

223. Chai, J.C., et al., *Finite volume radiative heat transfer procedure for irregular geometries.* Journal of Thermophysics and Heat Transfer, 1995. **9**(3): p. 410-415.

224. Ghiaasiaan, S.M., *Convective heat and mass transfer*. 2018: CRC Press.

225. Kaviany, M., *Principles of heat transfer in porous media*. 2012: Springer Science & Business Media.

226. Ghanbarian, B., et al., *Tortuosity in porous media: a critical review.* Soil science society of America journal, 2013. **77**(5): p. 1461-1477.

227. Shen, L. and Z. Chen, *Critical review of the impact of tortuosity on diffusion.* Chemical Engineering Science, 2007. **62**(14): p. 3748-3755.

228. Linstrom, P.J. and W.G. Mallard, *NIST Chemistry WebBook, NIST Standard Reference Datatbase Number 69*. Gaithersburg, MD: National Institute of Standards and Technology.

229. Deissler, R. and C. Eian, *Investigation of effective thermal conductivities of powders*. 1952, Lewis Flight Propulsion Lab., NACA.

230. Xu, G., et al., *High-temperature transport properties of Nb and Ta substituted CaMnO3 system.* Solid State Ionics, 2004. **171**(1-2): p. 147-151.

231. Hruby, J., *Technical feasibility study of a solid particle solar central receiver for high temperature applications*. 1986, Sandia National Labs., Livermore, CA (USA).

232. Al-Din, N. and D.J. Gunn, *Metering of solids by a rotary valve feeder.* Powder Technology, 1983. **36**(1): p. 25-31.

233. Ambrosini, A., et al., *Calcium Manganite-Based Materials for High Temperature CSP Thermochemical Energy Storage*. 2017, Sandia National Lab.(SNL-NM), Albuquerque, NM (United States).

234. Arifin, D., et al., *CoFe 2 O 4 on a porous Al 2 O 3 nanostructure for solar thermochemical CO 2 splitting.* Energy & Environmental Science, 2012. **5**(11): p. 9438-9443.